ADVANCED CRYSTAL GROWTH TECHNIQUES WITH III-V BORON COMPOUND SEMICONDUCTORS

by

CLINTON E. WHITELEY

B.S., Benedictine Collage, 2005
M.S., Kansas State University, 2008

AN ABSTRACT OF A DISSERTATION

submitted in partial fulfillment of the requirements for the degree

DOCTOR OF PHILOSOPHY

Department of Chemical Engineering
College of Engineering

KANSAS STATE UNIVERSITY
Manhattan, Kansas

2011

ABSTRACT

Semiconducting icosahedral boron arsenide, $B_{12}As_2$, is an excellent candidate for neutron detectors and radioisotope batteries, for which high quality single crystals are required. Thus, the present study was undertaken to grow $B_{12}As_2$ crystals by precipitation from metal solutions (nickel) saturated with elemental boron and arsenic in a sealed quartz ampoule. $B_{12}As_2$ crystals of 8-10 mm were produced when a homogeneous mixture of the three elements was held at 1150 °C for 48-72 hours and slowly cooled (3°C/hr). The crystals varied in color and transparency from black and opaque to clear and transparent. X-ray topography (XRT), Raman spectroscopy, and defect selective etching confirmed that the crystals had the expected rhombohedral structure and a low density of defects ($5x10^7$ cm^{-2}). The concentrations of residual impurities (nickel, carbon, etc) were found to be relatively high (10^{19} cm^{-3} for carbon) as measured by secondary ion mass spectrometry (SIMS) and elemental analysis by energy dispersive x-ray spectroscopy (EDS).

The boron arsenide crystals were found to have favorable electrical properties (μ = 24.5 cm^2 / Vs), but no interaction between a prototype detector and an alpha particle bombardment was observed. Thus, the flux growth method is viable for growing large $B_{12}As_2$ crystals, but the impurity concentrations remain a problem.

ADVANCED CRYSTAL GROWTH TECHNIQUES WITH III-V BORON COMPOUND SEMICONDUCTORS

by

CLINTON E. WHITELEY

B.S., Benedictine Collage , 2005
M.S., Kansas State University, 2008

A DISSERTATION

submitted in partial fulfillment of the requirements for the degree

DOCTOR OF PHILOSOPHY

Department of Chemical Engineering
College of Engineering

KANSAS STATE UNIVERSITY
Manhattan, Kansas

2011

Approved by:
Major Professor
Dr. James H. Edgar

ABSTRACT

Semiconducting icosahedral boron arsenide, $B_{12}As_2$, is an excellent candidate for neutron detectors and radioisotope batteries, for which high quality single crystals are required. Thus, the present study was undertaken to grow $B_{12}As_2$ crystals by precipitation from metal solutions (nickel) saturated with elemental boron and arsenic in a sealed quartz ampoule. $B_{12}As_2$ crystals of 8-10 mm were produced when a homogeneous mixture of the three elements was held at 1150 °C for 48-72 hours and slowly cooled (3°C/hr). The crystals varied in color and transparency from black and opaque to clear and transparent. X-ray topography (XRT), Raman spectroscopy, and defect selective etching confirmed that the crystals had the expected rhombohedral structure and a low density of defects ($5x10^7$ cm^{-2}). The concentrations of residual impurities (nickel, carbon, etc) were found to be relatively high (10^{19} cm^{-3} for carbon) as measured by secondary ion mass spectrometry (SIMS) and elemental analysis by energy dispersive x-ray spectroscopy (EDS).

The boron arsenide crystals were found to have favorable electrical properties (μ = 24.5 cm^2 / Vs), but no interaction between a prototype detector and an alpha particle bombardment was observed. Thus, the flux growth method is viable for growing large $B_{12}As_2$ crystals, but the impurity concentrations remain a problem.

Copyright

CLINTON E. WHITELEY

2011

Table of Contents

List of Figures ix
List of Tables xiii
Acknowledgements xiv
Dedication xv
CHAPTER 1 - BORON AND THE ^{10}B ISOTOPE 1
Boron Rich Solids: B_{12} Icosahedra and $B_{12}As_2$ 2
Icosahedral Boron Bonding and Structure 2
Boron Compounds and Properties 3
Crystal Growth Methods for $B_{12}As_2$ 6
Chemical Vapor Deposition (CVD) 6
The Flux Growth Method 7
$B_{12}As_2$ Semiconductor Applications 9
Radiation Detectors 9
Beta Voltaic Devices 14
CHAPTER 2 - ANALYSIS TECHNIQUES 18
Scanning Electron Microscope (SEM) and Energy Dispersive X-ray Spectroscopy (EDS) 18
X-ray Photoelectron Spectroscopy (XPS) 19
Secondary Ion Mass Spectrometry (SIMS) 20
X-ray Diffraction (XRD) and the Coefficient of Thermal Expansion 21
X-ray Diffraction Topography (XRT) 22
Raman Spectroscopy 24
Van der Pauw and the Hall Effect 24
CHAPTER 3 - COEFFICIENT OF THERMAL EXPANSION BETWEEN 25°C AND 850°C 29
Abstract 29
Introduction 30
Experimental Methods 33
Results and Discussion 34
Conclusions 37

Acknowledgements 37
References 39
CHAPTER 4 - Crystal Growth of $B_{12}As_2$ 40
Abstract 40
Introduction 41
Experimental Methods 43
Results and Discussion 45
Conclusions 50
References 52
CHAPTER 5 - DEFECT SELECTIVE ETCHING 54
Abstract 54
Introduction 55
Experimental Procedure 56
Results and Discussion 58
Conclusions 62
References 63
CHAPTER 6 - CRYSTAL FACET ORIENTATION 65
Abstract 65
Introduction 66
Experimental Procedures 68
Results and Discussion 69
Conclusions 71
References 73
CHAPTER 7 - ELECTRICAL PROPERTIES AND DEVICE TESTING 74
Abstract 74
Introduction 75
Experimental Procedures 79
Results and Discussion 80
Conclusions 88
References 89
CHAPTER 8 - CONCLUSIONS AND FUTURE WORK 91

REFERENCES 94

List of Figures

Figure 1-1 - The crystal structure of $B_{12}As_2$. The boron atoms (small spheres) are collected as twelve atom icosahedra. The boron atoms are positioned at the corners of the icosahedra, the icosahedra are situated at the corners of a rhombohedra, and the group V atoms (large spheres) are in the center, spanning the body diagonal [12,13]. 1

Figure 1-2 – Schematic depicting the unusual bonding configuration of boron icosahedron. 2

Figure 1-3 – Apparatus for the chemical vapor deposition (CVD) of $B_{12}As_2$ crystals. 7

Figure 1-4 – Schematic depicting (A) the source materials before flux growth, (B) the homogeneous liquid produced above the eutectic temperature, and (C) crystals precipitated out of the solution during the cooling process. 8

Figure 1-5 – Proposed design for a Schottky diode using a *p*-type $B_{12}As_2$ crystal [39]. 10

Figure 1-6 - Schematic diagram of the movement of electrons and holes in a semiconductor detector, which produces a measurable signal [42]. The detector is biased with a voltage, which creates an electric field within the detector. When an interaction with a radioactive particle happens the energy deposited by the radiation produces a current, the movement of electron-hole pairs, that is measured as a signal. 11

Figure 1-7 – Depiction of some different types of crystal defects [42]. All of which degrade the electrical properties of a semiconductor. 12

Figure 1-8 – Schematic diagram depicting a neutron detector comprised of a neutron capture and conversion layer on a semiconductor diode [43-45]. 13

Figure 1-9 – Design for a planar beta voltaic device illustrating how the device works and how they can be scaled to micro sizes [51-53]. 14

Figure 2-1 –Interrelation between crystal characterization, growth and properties [40]. 18

Figure 2-2 - Schematic diagram depicting the Hall effect measurement. 25

Figure 2-3 - van der Pauw four point probe setup, and depiction of measurements to determine R_A, R_B, and V_H. 27

Figure 2-4 - Configurations for conducting a Hall effect measurement. A) the traditional approach is to place the contacts at the very edge of the sample. Alternatives include B) to place the contacts over the thickness of the sample, and C) to construct a “Hall Bar”. 28

Figure 3-1 - Rhombohedral unit cell of $B_{12}As_2$, shown in red, with icosahedral boron clusters (in green) at the vertices and As-As (in blue) chains along the body diagonal, the rhombohedral [111] direction, and also showing the relationship to the axes and unit cell (in black) of the hexagonal setting. 31

Figure 3-2 - Temperature profile of the resistance heater during the synthesis of $B_{12}As_2$ powder. Notice the boron is held in the hot zone and the arsenic is held in a cooler zone (to maintain 0.5atm). 33

Figure 3-3 - Room temperature XRD spectrum for $B_{12}As_2$ powder before (top) and after (bottom) heating to 850°C. All peaks were identified to be associated with boron arsenide, by comparison with the $B_{12}As_2$ reference pattern at the bottom. 35

Figure 3-4 - Linear and volumetric coefficients of thermal expansion of $B_{12}As_2$ as a function of temperature. Note the large value of the volumetric coefficient (right axis) and the anisotropy of the perpendicular (*a* axis) and parallel (*c* axis) coefficients (left axis). The dotted lines are fits to the data of the form $\alpha=\alpha_0+\alpha_1*T+\alpha_2/T^2$, with the values of α_0, α_1 and α_2 given in Table 3-1. 37

Figure 4-1 - The nickel boron binary phase diagram. The liquid phase is maintained down to the eutectic temperature of 1018°C (55mol% Ni) [34]. 43

Figure 4-2 - In the first step of crystal growth, a homogeneous nickel boride liquid mixture is created by heating only the B-Ni component mixture (Top). Icosahedral boron arsenide crystal growth is initiated by subliming the arsenic, which then reacts with the boron in solution to form icosahedral boron arsenide crystals (Bottom). 45

Figure 4-3 - Image of a $B_{12}As_2$ crystal in reflection, 7mm in longest dimension, depicting platelet shaped crystals (Top). Image of $B_{12}As_2$ crystals growing with many facets on the arsenic end of the ingot (bottom). 48

Figure 4-4 - Raman energy spectrum for flux grown boron arsenide crystals. 49

Figure 4-5 - Image of $B_{12}As_2$ crystals after defect selective etching for 5 minutes at 500°C. The etch-pit density was $4.4x10^7 pits/cm^2$. The scale on the images is 200μm (Top). SEM image of the typical triangular etch pits (Bottom). 50

Figure 5-1 - SEM images of the three multi-faceted crystals with illustrations of the crystals and the label given to each facet. 57

Figure 5-2 - SEM image of typical triangle etch pits. 60

Figure 5-3 – SEM image of ovals that formed on side four of the multi-faceted crystals. 61
Figure 5-4 - Triangle shaped etch-pit that is a different size than the pits observed on side 2 of the multi-faceted crystals. 62
Figure 6-1 – Possible slip-planes in $B_{12}As_2$ crystals. The indicated plane is shown on each unit cell with a line or a square. Note that the four index hexagonal system is utilized. These planes can easily be related to the three-index rhombohedral system using the standard relationship such that [11-20] $B_{12}As_2$ is parallel to [10-1] $B_{12}As_2$, [9] [0001] $B_{12}As_2$ is parallel to [111] $B_{12}As_2$, and (0003) $B_{12}As_2$ is equivalent to (111) $B_{12}As_2$ [14]. 67
Figure 6-2 - Schematic of the scanning system at beamline X-19C at the NSLS. Both the crystal and film are scanned simultaneously through the incident beam enabling large-area coverage. 68
Figure 6-3 –SWBXT topograph of indexed $B_{12}As_2$ Laue pattern. The presence of distinct diffraction spots shows that the crystals are high quality single crystalline. 69
Figure 6-4 – Optical image of a $B_{12}As_2$ crystal depicting the preferred facet orientation. 70
Figure 6-5 – Enlarged topographs with different g vectors of $B_{12}As_2$ crystal. Surface plane is (111) and vertical side plane is (-101). 71
Figure 6-6 - SEM images of typical triangle shaped etch pits. 72
Figure 7-1 - van der Pauw four point probe setup depicting the measurements of R_A, and R_B. .. 75
Figure 7-2 - Schematic diagram of the NIM-BIN electronic system for testing radiation detectors. 77
Figure 7-3 - Images of the boron arsenide crystals with (A) Ohmic and (B) Schottky metal contacts. (C) Image of the project box used to hold the electronic device in place, and (D) close-up of the electrical connections between the metal contacts and the Anode and ground. 80
Figure 7-4 - Plot of the impurity concentration vs. the depth of the material. Concentrations above 10^{18} are considered degenerate [20]. 82
Figure 7-5 - TRIM simulation plot of the penetration distance of 5.5MeV alpha particles into boron arsenide crystals with a Ti/Au metal contact. 83
Figure 7-6 - TRIM ionization plot showing the alpha particles depositing their kinetic energy at the end of their range (12.9 μm). 84

Figure 7-7 - I-V curve measured on a boron arsenide crystals with Ohmic and Schottky metal contacts. Notice the rectifying region between +5V and -15V..... 85
Figure 7-8 - Energy spectrum for the μτ product measurement. The measurement with the alpha particle source was taken for a longer time, and thus collected more counts, but the Channel Number (9) indicates background energy. The most significant observation being that there is no full energy peak for the 5.5MeV alpha particle, which should appear as an individual peak in the 300-500 Channel Number range. 87

List of Tables

Table 1-1 - Candidates for boron based semiconductors [14-18]. 3
Table 1-2 – Fundamental properties of some boron-rich semiconductors compared to two common substrate materials for the crystal growth of $B_{12}As_2$ [18,31-34]. 5
Table 1-3 - Exothermic nuclear reactions between thermal neutrons and the three most common capture materials [42]. 10
Table 1-4 – Properties of radioactive isotopes; note that not all of the sources are mono-energetic. The gray-filled boxes represent the most commonly utilized radioisotopes, and the yellow-filled box indicates a valuable isotope that is not used because the kinetic energy is high enough to permanently damage beta voltaic batteries [51,54]. 16
Table 3-1 - Coefficients of thermal expansion for $B_{12}As_2$ (25-850°C). 36
Table 4-1 - Crystal size as a function of ternary molar composition (B:As:Ni) of the starting materials. The highlighted values are the important factors that hindered the crystal growth; boron composition too high, boron composition too low, and arsenic composition too low, respectively. Note that the listed values only represent the most interesting of the 25 tested compositions. 46
Table 4-2 - Icosahedral boron arsenide crystal size as a function of cooling rate and high temperature dwell time. 47
Table 5-1 -Results of the DSE optimization experiments revealing the optimum etching conditions (550 C for 2 min) for $B_{12}As_2$ crystals. The "0" indicates no etch pits or etch pits that were <5 μm in diameter. The "∞" means the entire surface etched or no change in EPD from the previous trial. 58
Table 5-2 - Tabulated results from etching the multi-faceted crystals. There was etching on 3 of the 4 studied sides. General observations about the pre-etch structures, the shape and pattern of the etch pits, and additional notes were recorded. 60
Table 7-1 – Tabulated atomic percent concentrations of the major impurities found using XPS. 81
Table 7-2 - List of the data obtained from the Hall effect measurement conducted on a bulk boron arsenide crystal. For comparison the same data are included for a thin film of boron arsenide. 86

Acknowledgements

I wish to thank my committee members who were more than generous with their expertise and precious time. A special thanks to Dr. James Edgar, my major professor for his countless hours of reflecting, reading, encouraging, and most of all patience throughout the entire process. Thank you Dr. Kenneth Klabunde, Dr. Larry Erickson, Dr. Mary Rezac, and Dr. Z.J. Pei for agreeing to serve on my committee.

I would like to acknowledge and thank the College of Engineering at Kansas State University for allowing me to conduct my research and providing any assistance requested. Special thanks goes to the members of the staff in the Chemical Engineering office for their continued support.

Finally I would like to thank the professors and administrators in the Chemical Engineering Department that assisted me with this project. Their excitement and willingness to provide feedback made the completion of this research an enjoyable experience.

Dedication

I dedicate my dissertation work to my family and friends. A special feeling of gratitude to my loving parents, Gregg and Eva Fujan and Rick Whiteley whose words of encouragement and push for perseverance ring in my ears. My siblings Lea, Danya, Cady, McKenzie, and Connor have never left my side and are very special to me.

I also dedicate this dissertation to my many friends who have supported me throughout the process. I will always appreciate all they have done, especially Ryan Green for helping me develop my professional skills, Tyler Selbe and Yi Zhang for the many hours of proofreading, and Ed Keck for teaching me how to believe in myself.

I dedicate this work and give special thanks to my wife Valerie Whiteley and my magnificent children Maddox, Reese, and Dominic for being there for me throughout the entire doctorate program. You four are my most dedicated cheerleaders.

CHAPTER 1 - BORON AND THE ^{10}B ISOTOPE

In the structures of the simplest boron-rich solids, B_{12} icosahedra are centered at the vertices of a rhombohedral unit cell, as illustrated in Figure 1-1. The complex crystal structures of icosahedral boron-rich solids have prompted long-standing interest in their stability at high temperature and under high pressures. Many recent studies have focused on the stability and transformations of complex forms of elemental boron at high pressure [1-6].

Interesting phenomena such as superconductivity, semiconductor-to-metal transitions, and pressure-induced amorphization [7-8] have been reported at high pressures in these complex forms of boron. Additionally, icosahedral boron compounds have been shown to be excellent thermoelectric materials [9-11].

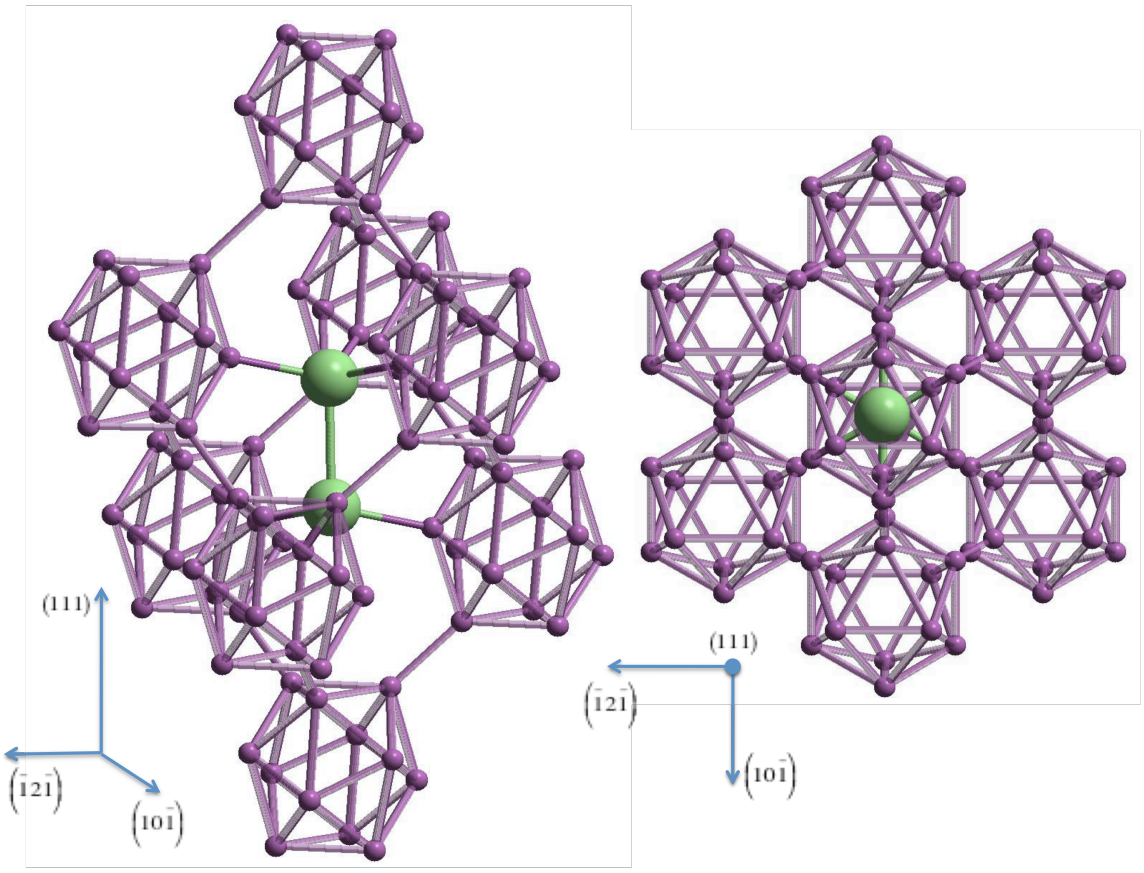

Figure 1-1 - The crystal structure of $B_{12}As_2$. The boron atoms (small spheres) are collected as twelve atom icosahedra. The boron atoms are positioned at the corners of the icosahedra, the icosahedra are situated at the corners of a rhombohedra, and the group V atoms (large spheres) are in the center, spanning the body diagonal [12,13].

Boron Rich Solids: B_{12} Icosahedra and $B_{12}As_2$

Icosahedral Boron Bonding and Structure

Pure boron and boron-rich solids are materials with unusual structures; where B_{12} icosahedra are the primary building blocks of pure boron and many boron-rich solids. The bonding within icosahedra is metal-like: internal bonding electrons are delocalized over the surface of each icosahedron with densities that peak at the centers of the triangular faces formed by three neighboring boron atoms, as seen in Figure 1-2 [12,13]. As a consequence, these compounds are very stable, with melting temperatures up to 2700 K, which is interesting both from fundamental and application points of view [12,13].

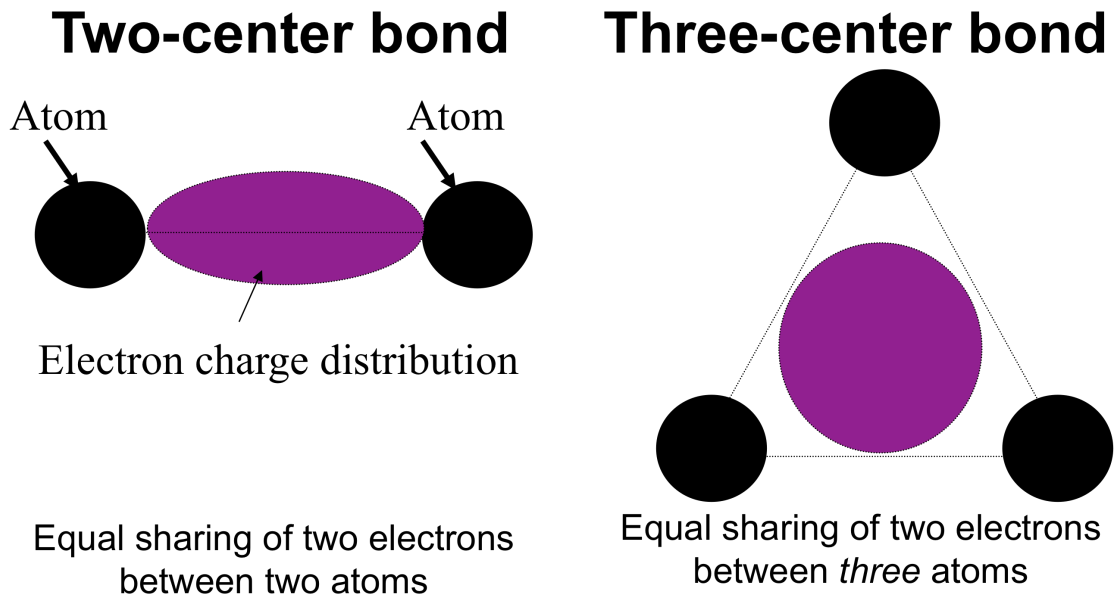

Figure 1-2 – Schematic depicting the unusual bonding configuration of boron icosahedron.

The unusual bonding is evident from x-ray diffraction studies, which indicate charge accumulation about the center of the icosahedron faces rather than along the lines that link adjacent boron atoms [12,13]. Strong covalent bonds link boron atoms of each icosahedron to boron atoms of neighboring icosahedra, and the remaining six boron atoms of each icosahedron bond to the cations on the *c* axis. Each boron atom of an icosahedron participates in the electron-deficient bonding as well as in covalent bonding to atoms outside of the icosahedron [12,13]. All of the bonding is primarily attributed to electrons from the second shell of the boron atoms. One of the three second-shell electrons is involved in bonding external to the icosahedron, and the remaining two electrons participate in the internal bonding [12,13].

Table 1-1 - Candidates for boron based semiconductors [14-18].

Element or Compound	Barriers to crystal growth and device fabrication
α-B	Thermodynamically stable only at temperatures below 1100°C, making crystal growth difficult
β-B	Low charge carrier mobility; high crystal defect densities
cBN	Requires extremely high pressures (>5 GPa) limiting crystals sizes to <5 mm
hBN	Stacking fault energy is low, making crystal growth difficult; crystals limited in size to less than 5 mm; doping to control electrical properties may be difficult; very susceptible to radiation damage
BP	High vapor pressure of phosphorus for temperatures > 1000°C; tends to decompose to $B_{12}P_2$; films on Si substrates are heavily doped with Si.
BAs	Stable only at low temperatures (<920°C), due to high As vapor pressure; at higher temperatures decomposes to $B_{12}As_2$
B_4C	Very high melting temperature (2450°C); propensity for crystal twinning; highly variable stoichiometry; inherent crystalline disorder
$B_{12}P_2$	High melting point temperature (2120°C) may complicate crystal growth from the melt
$B_{12}As_2$	Melting point is probably high (~2027°C), complicating crystal growth from the melt

In most compound semiconductors, chemical bonds are formed between two atoms sharing electrons. Consequently, the highest electron charge density is located on a line between the two atoms. In boron compounds that contain the twelve boron atom icosahedra, three boron atoms (each situated at the apex of an equilateral triangle) share two electrons [12,13]. The highest electron charge density is located not on a line between boron atoms, but in the center of the equilateral triangle. The boron icosahedra are highly stable structures, but are electron deficient. To gain the charge necessary to complete a stable bonding configuration, the icosahedra form external bonds to other icosahedra (in pure boron) or atoms (As in $B_{12}As_2$ for example) [12,13].

Boron Compounds and Properties

Some candidates for boron containing semiconductors are summarized in Table 1-1. There are relatively few studies on the synthesis of boron-rich compounds (materials with a majority concentration of boron), and even fewer crystal growth studies [14-29]. Crystals are the

preferred form for obtaining the best electrical properties since the charge transport mobility can be reduced by as much as 3 orders of magnitude in amorphous or polycrystalline materials [30]. Structural characterization of boride crystals and thin films revealed poor quality materials (high densities of dislocations, twins, and high impurity concentrations). The electrical properties of boron-based semiconductors as a function of the impurities is only reported in a few studies [26-29]. Thus, the intrinsic electrical properties of boron-based semiconductors could be significantly different than the reported values.

More specifically, the icosahedral boron pnictides, $B_{12}As_2$ and $B_{12}P_2$, of III-V semiconductors have rarely been studied; fewer than 100 papers report any aspect of the materials. Table 1-2 lists the fundamental properties of three boron-rich solids, and two other common semiconductors. $B_{12}As_2$ semiconductors have several advantages over other boron-rich compounds for neutron detection [35-38]. First, $B_{12}As_2$ hole mobilities are relatively high, on the order of 50-100 $cm^2/V \cdot s$ [18]. A high mobility enables electrons and holes to reach the contacts of the device; this is an essential property for good charge collection efficiencies in electrical devices. $B_{12}As_2$ also has a wide energy band gap, 3.2 eV, and a low intrinsic carrier concentration [35]. Consequently, $B_{12}As_2$ diodes will have low reverse bias leakage currents and better signal to noise ratios than semiconductors with smaller band-gaps [35].

$B_{12}As_2$ crystals are also thermally stable, which makes crystal growth more convenient than BP and BAs. In unpublished experiments performed at Kansas State University, no changes in morphology or composition (as measured by Auger electron spectroscopy) were observed with an epitaxial $B_{12}As_2$ on a 6H-SiC substrate heated to 1350 °C for 30 minute in flowing hydrogen. Thus, changes in the stoichiometry of the compounds due to incongruent evaporation of its elements are insignificant at high temperatures. By contrast, BAs and BP have relatively high vapor pressures, and decompose by the loss of the group V element upon heating above 900 °C [18,19].

Another interesting property of $B_{12}As_2$ is an ability to self-heal from radiation damage [12,13]. Radiation damage creates interstitial-vacancy pairs known as Frenkel defects, and limits the lifetime of common semiconductor detectors. However, icosahedral boron compounds are highly resistant to radiation damage. Carrard *et. al.* [12] showed that bombarding $B_{12}As_2$ compounds with high-energy electrons and ions, at doses that would make most materials amorphous, resulted in no detectable crystal damage [12,13].

Table 1-2 – Fundamental properties of some boron-rich semiconductors compared to two common substrate materials for the crystal growth of $B_{12}As_2$ [18,31-34].

Property	Boron Carbide	$B_{12}P_2$	$B_{12}As_2$	Si	SiC
Color	Orange, Yellow	Black, Blue, Transparent	Amber, Transparent	Black	Brown, Transparent
Structure	Rhombohedral	Rhombohedral	Rhombohedral	Cubic	Hexagonal, Cubic
Lattice constant (Å)	a = 5.987 c = 11.841	a = 5.987 c = 11.841	a = 6.156 c = 11.929	5.4307	3C-4.359 4H-3.073,10.053 6H-3.073,15.11
Melting (°C)	2450 C	2120 C	2027 C	1414 C	2730
Bandgap (eV)	2.5	3.35	3.2	1.12	3C-2.36, 4H-3.23 6H-3.05
Resistivity (Ωcm)	0.1-10	*p*-type, $5.2x10^4$, $9.2x10^4$	*p*-type, 10^4-10^5	10^3	10^2-10^6
Mobility (cm^2/Vs)		50		1400	900
Thermal Expansion (K^{-1})	$5x10^{-6}$			$2.6x10^{-6}$	$4.0x10^{-6}$
Thermal Conductivity (W/mK)	29-67	38	120	149	3C-3.6, 4H-3.7, 6H-4.9

The unusual three-atom chemical bonding of the boron icosahedra structures in these semiconductors is hypothesized to be the reason for the radiation resistance. When an energetic electron, ion, or neutron displaces a boron atom, a negatively charged degenerate icosahedra (with only eleven boron atoms) and a positively charged isolated boron ion is formed. The attractive force between the icosahedra and the boron ion is strong enough to draw the relatively small boron ion back into the structure in order to complete the icosahedra. This self-healing is a distinctive property of boron compounds that form icosahedra, and is not observed in other boron compounds with regular two-atom chemical bonds (such as cubic BP and BAs). In boron

compounds with the cubic structure, crystal damage increases with radiation dose, until the solid is eventually rendered amorphous [18,19]. Clearly, the contrasting self-healing process of icosahedral boron semiconductors would be advantageous for devices subject to high-energy particles.

Crystal Growth Methods for $B_{12}As_2$

Chemical Vapor Deposition (CVD)

Although $B_{12}As_2$ crystals have many desirable properties, the high melting temperature and large thermal expansion make some crystal growth techniques, such as melt growth and CVD, prohibitively difficult. The high melting temperature of $B_{12}As_2$ (2027°C) [35] makes crystal growth from the melt difficult. Thus, the most commonly reported technique for synthesizing boron arsenide crystals is chemical vapor deposition (CVD).

Thin films are produced from gas-phase reactants in an open system, shown schematically in Figure 1-3. As a process, CVD enables excellent control of the composition, stoichiometry, and impurity concentrations in the thin films - all necessary properties for making electronic devices [35]. $B_{12}As_2$ was deposited on several foreign substrates including silicon and silicon carbide (4H-SiC, 6H-SiC, and 15R-SiC), but the mismatch of properties creates stresses, crystalline defects and contamination from the substrate, degrading the properties of the films. High temperatures (>1300 °C) are generally necessary to produce good quality $B_{12}As_2$ by CVD, but at this temperature silicon substrates react with the film. Silicon contamination is a common problem reported for boron containing films on silicon substrates [35]. Similarly, $B_{12}As_2$ can react with SiC to form a boron carbide transition layer between the film and substrate at high temperatures [35]. Bowing and cracking in $B_{12}As_2$ films suggests that the coefficient of thermal expansion is significantly different than those of Si and SiC. The crack density increases with film thickness, ultimately resulting in the films delaminating from the substrate, observed with films as thin as 4 to 5 microns [35]. To completely avoid these problems, and to produce the best possible electrical properties, bulk crystals are needed. Thus, the synthesis of thin films of $B_{12}As_2$ on foreign substrates does not produce the quality of material necessary for good devices.

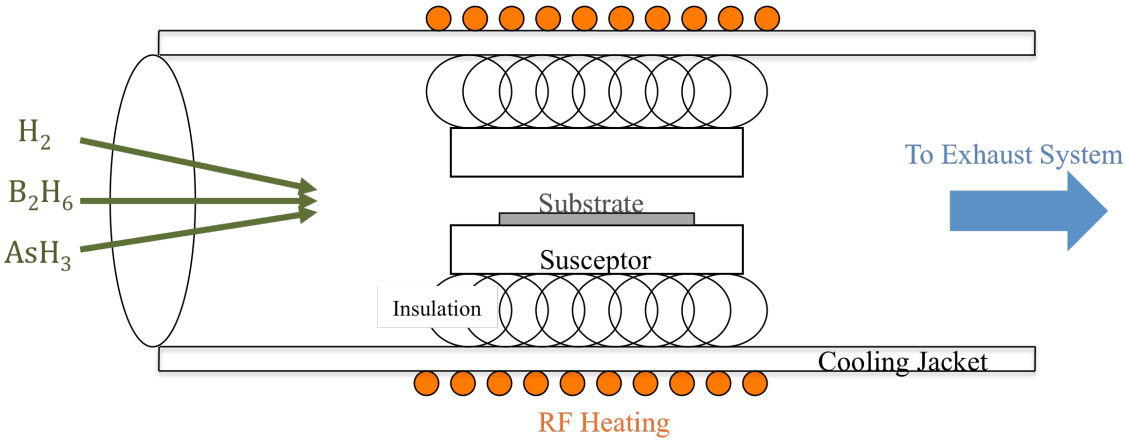

Figure 1-3 – Apparatus for the chemical vapor deposition (CVD) of $B_{12}As_2$ crystals.

The Flux Growth Method

To avoid the problems associated with thin film crystal growth, in this study bulk $B_{12}As_2$ crystals were grown by precipitation from molten metal fluxes at temperatures below 1300°C in sealed quartz ampoules. The challenges associated with growing $B_{12}As_2$ crystals by the flux method include: excess arsenic must be present in the vapor phase in the tube, the arsenic must be held at a lower temperature than the nickel boride solution (to maintain a safe vapor pressure within the tube), a homogeneous liquid must be produced at the reaction temperature, no binary B:As phase diagram exists, and no ternary B:As:Ni phase diagram exists. The feasibility of precipitating boron arsenide crystals from molten metal solutions was examined by several researchers [22,37], but producing large crystals was not the primary goals of the previous research. To produce larger crystals, an exploration of the ternary flux system (B:As:Ni) was undertaken to determine the optimum growth conditions.

The flux growth method follows many of the same principles as the more common melt growth method: heating to a high temperature, forming a homogeneous liquid, and crystallization during a cooling process. However, melt growth has higher growth rates and there is no contamination from a solvent. Although using the melt growth method would be preferred, boron arsenide has a prohibitively high melting temperature, and the vapor pressure of the group V material is too high at the melting temperature of boron arsenide. These two factors would make any attempt at growing boron arsenide from the melt both extremely expensive and dangerous.

In the flux growth method, the constituents of the material to be crystallized are dissolved in a suitable solvent and crystallization occurs as the solution becomes critically supersaturated,

as seen in Figure 1-4. The supersaturation may be promoted by evaporation of the solvent, by cooling the solution or by a transport process in which the solute is made to flow from a hotter to a cooler region [40]. The principal advantage of flux growth is a greatly reduced crystal growth temperature compared to melt growth. A reduction in the temperature is desirable or even essential for many materials, in particular for the following categories [40].

- *Incongruent melting* – the compound decomposes before melting causing crystallization from the solution to produce other phases.
- *Materials that undergo a phase transition* - resulting in severe strain or even fracture. The phase transition is avoided by crystal growth at a temperature lower than the phase transition.
- *Materials with a high vapor pressure at the melting point*.
- *Materials with volatile constituent* - whose chemical composition may change on heating close to the melting point.
- *Highly refractory materials* - which require difficult or expensive techniques for crystallization from the melt.

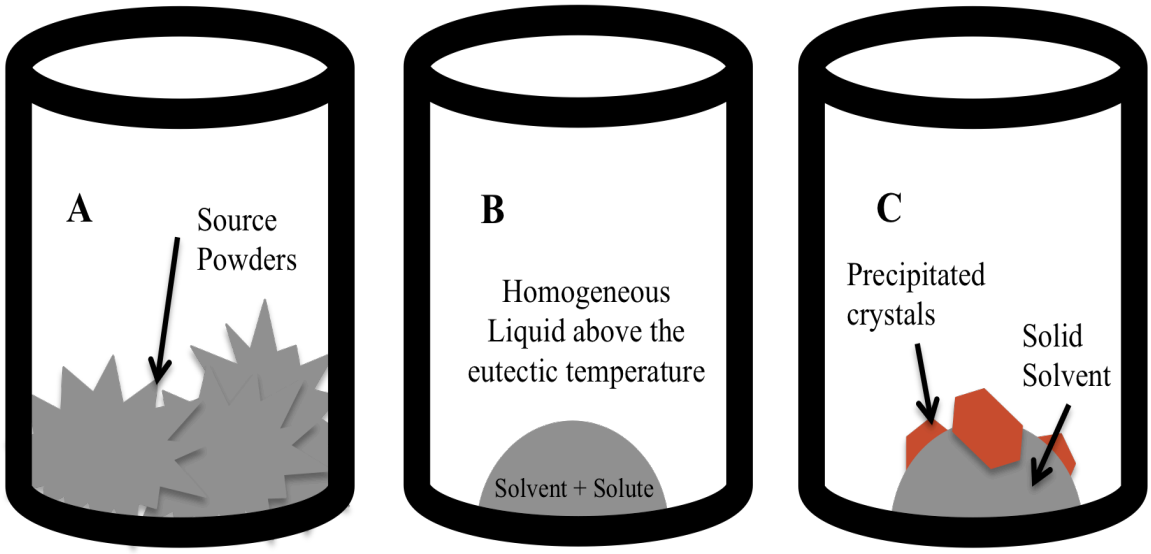

Figure 1-4 – Schematic depicting (A) the source materials before flux growth, (B) the homogeneous liquid produced above the eutectic temperature, and (C) crystals precipitated out of the solution during the cooling process.

Other advantages of the flux method include a low temperature gradient and unconstrained crystal growth; that is the crystal can grow free from mechanical or thermal constraints into the solution and develop facets. Additionally, the relatively low growth

temperature compared with the melting point of the solute often results in a better crystal quality with respect to point defects, dislocation densities and low-angle grain boundaries, compared to crystals grown directly from the melt [40]. Comparatively, the disadvantages of the method are substitutional or interstitial incorporation of solvent ions into the crystal, microscopic or macroscopic inclusion of solvent or impurities, non-uniform doping, and a slow growth rate [40].

Several molten metal solutions have proven successful for the growth of boride crystals including copper, nickel, palladium, silver, and platinum [20-24]. The choice of solvent is dictated by solubility of boron or boron compounds, the vapor pressure of the molten metal, and the tendency of the solvent to react or form solid solutions with the boride of interest [20].

The focus here was on nickel as the solvents of choice, as boron has a high solubility in nickel and nickel is not prohibitively expensive. The minimum temperature possible for crystal growth is determined by the boron-metal eutectic, approximately 1018 C [20]. Previous attempts to grow bulk $B_{12}As_2$ crystals produced only 0.5-1mm specimens because the key parameters governing the growth (starting composition, high-temperature dissolution time, and cooling rate) were not fully considered [20-25]. Thus, by optimizing the crystal growth process large (>1cm) $B_{12}As_2$ crystals can be produced, allowing for a wide range of characterization techniques to be used to delineate the material properties. Furthermore, understanding the fundamental properties (thermal stability, crystal quality, impurity concentrations, mobility, etc.) of $B_{12}As_2$ is the best way to evaluate its potential for electronic devices such as neutron detectors.

$B_{12}As_2$ Semiconductor Applications

Radiation Detectors

The Department of Homeland Security spent $230 million to develop a better technology for detecting nuclear bombs (^{3}He gas detector), but has had to stop deploying the new machines because the supply of ^{3}He has plummeted. ^{3}He is an unusual isotope of helium, formed as a daughter product when tritium (^{3}H), part of the trigger mechanism in nuclear bombs, decays. Over the years the Department of Energy accumulated a substantial stockpile ^{3}He by maintaining nuclear weapons. The tritium decays into ^{3}He at the rate of 5.5% per year. Thus, the tritium in each bomb must be removed, purified (by removing the ^{3}He), and replenished every few years. However, governments mostly stopped making tritium in 1989. Demand for ^{3}He is estimated at 65,000 liters per year through 2013, but its production by the United States and Russia is only

about 20,000 liters. Additionally, the price has jumped to $2,000 per liter, from $100, in the last few years. With the steady decrease in supply of ^{3}He for neutron detectors, the search is on for a replacement material [41].

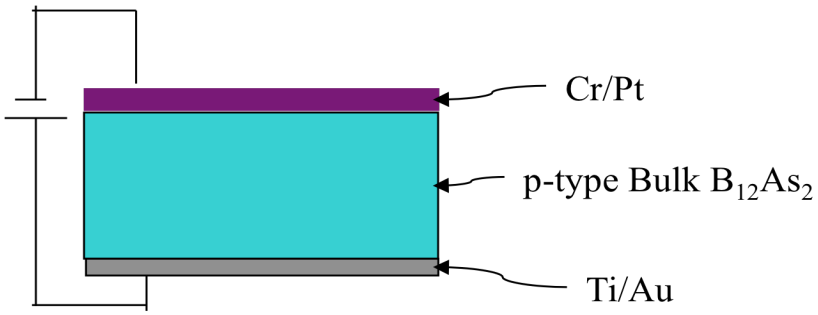

Figure 1-5 – Proposed design for a Schottky diode using a *p*-type $B_{12}As_2$ crystal [39].

Table 1-3 lists the three most common materials used in neutron detectors and the prominent reaction products [42]. The ^{10}B isotope has a large thermal neutron capture cross-section (3840 barns) – orders of magnitude larger than most elements, and on the same order as ^{3}He (5400) [42]. Thus, even thin layers of elemental ^{10}B or compounds rich in ^{10}B can absorb all incident thermal neutrons (100% efficiency). ^{10}B undergoes two nuclear reactions with thermal (~0.025 eV) neutrons [42]:

(1) $^{10}B + n \rightarrow {}^{7}Li\ (0.84\ MeV) + {}^{4}He\ (1.47\ MeV) + \gamma\ (0.48\ MeV)$ (94%)

(2) $^{10}B + n \rightarrow {}^{7}Li\ (1.02\ MeV) + {}^{4}He\ (1.78\ MeV)$ (6%)

In a boron semiconductor, each neutron produces three orders of magnitude more (~1.5 x 10^{6}) electron-hole pairs, compared to gas filled detectors like ^{3}He, as the energetic ^{7}Li and ^{4}He ions pass through the material [42]. In addition, reaction (1) produces a gamma ray that is undesirable, but, given the low atomic number (Z) of boron, photons are not expected to interact significantly with the $B_{12}As_2$. Thus, a thermal neutron detector could be based on a boron-rich Schottky, or *pn* diode, as seen in Figure 1-5.

Table 1-3 - Exothermic nuclear reactions between thermal neutrons and the three most common capture materials [42].

Reaction	Charged Particles Produced	Q Value (MeV)	σ (barns) for E_n = 0.025eV
^{10}B(n,α), ^{7}Li	α, ^{7}Li	2.78	3840
^{6}Li(n,α), ^{3}H	α, ^{3}H	4.78	937
^{3}He(n,*p*), ^{3}H	*p*, ^{3}H	0.765	5400

Semiconductor detectors are solid-state devices that utilize the movement of electrons and holes to measure interactions with radioactive particles [42]. An electric field is applied to the detector volume, and electrons in the semiconductor are fixed in the valence band until a radiation interaction provides the electron with enough energy to move it to the conduction band. Electrons in the conduction band can respond to the electric field in the detector, and therefore move to the positive contact that is creating the electrical field. The missing electron is called a "hole," and is filled by an adjacent electron. The shuffling of holes effectively moves a positive charge to the negative contact. The arrival of the electron at the positive contact and the hole at the negative contact produces the electrical signal that is sent to the detection system, as seen in Figure 1-6. Presently, the most common materials for semiconductor radiation detectors are: silicon, germanium, cadmium telluride, cadmium zinc telluride, and mercuric iodide [42]. The most important advantages of the semiconductor detectors, compared to other types of radiation counters, are the superior energy resolution and the detection speed [42], which is the ability to resolve the energy of particles out of a high flux poly-energetic energy spectrum.

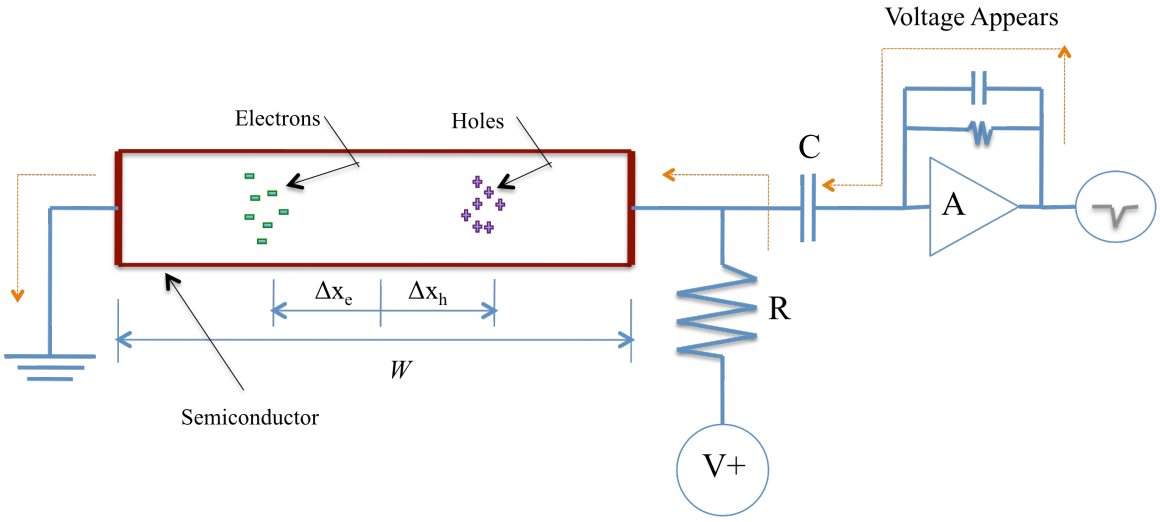

Figure 1-6 - Schematic diagram of the movement of electrons and holes in a semiconductor detector, which produces a measurable signal [42]. The detector is biased with a voltage, which creates an electric field within the detector. When an interaction with a radioactive particle happens the energy deposited by the radiation produces a current, the movement of electron-hole pairs, that is measured as a signal.

The superior resolution of a semiconductor detector is based on the premise that the starting material is a high quality crystal with low impurity concentrations and defect densities.

This is a reasonable assumption for the beginning-of-life of a semiconductor, but detectors will suffer damage after being exposed to radiation [42]. The principal type of radiation damage is caused by the collision of an incident radioactive particle with a lattice atom. As a result of the collision, the atom may be displaced into an interstitial position, thus creating an interstitial-vacancy pair known as a Frenkel defect, depicted in Figure 1-7. A recoiling atom may also have enough energy to displace other atoms, potentially producing many Frenkel defects [42].

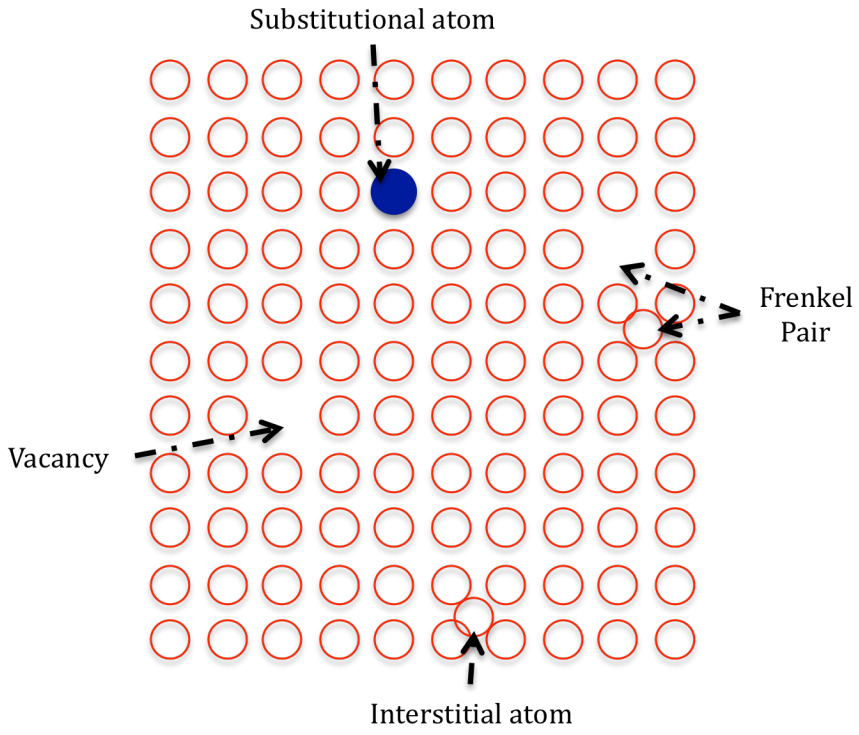

Figure 1-7 – Depiction of some different types of crystal defects [42]. All of which degrade the electrical properties of a semiconductor.

Crystal imperfections affect the performance of the detector because trapping centers for electrons and holes may be created, or new donor or acceptor states can be formed. Additional trapping centers and energy states change the fundamental properties of a semiconductor, such as the carrier lifetime, mobility, and energy resolution of the detector. The changes are gradual, but the final result is shortening of the detector lifetime. Because of radiation damage, semiconductor detector lifetimes can be limited to as little as a few hours depending on the energy of the radiation source and semiconductor material [42]. Thus leading to the need for a detector with superior radiation resistance.

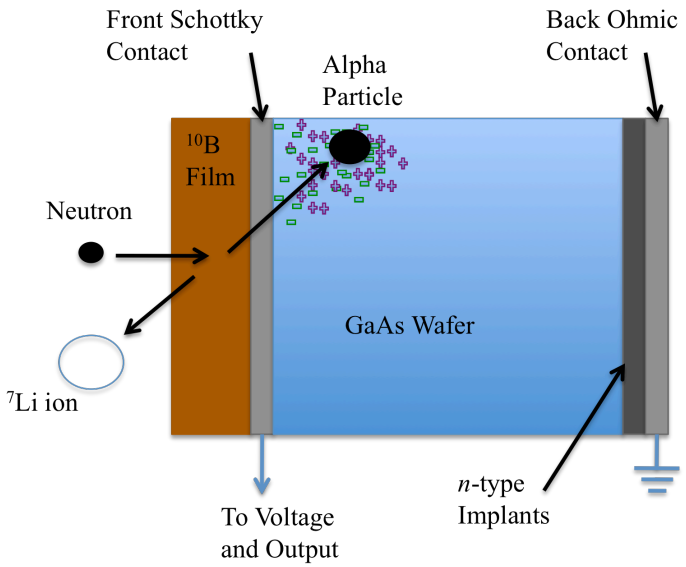

Figure 1-8 – Schematic diagram depicting a neutron detector comprised of a neutron capture and conversion layer on a semiconductor diode [43-45].

Despite the lack of fundamental information on the crystallographic and electrical properties, several attempts to make neutron detectors from boron-based semiconductors have been reported in the literature; however, the efficiency and stability of the reported boron devices was quite poor [46-48]. Low efficiencies can be attributed to the poor quality of materials employed. The early work by Wald and Bulitt [30], who proposed using α-rhombohedral boron for neutron detectors, is typical of these attempts. However, the α-B crystals had high electron trap densities and carrier concentrations, which resulted in low device charge collection efficiencies [30].

An alternate technique is to introduce a neutron conversion layer adjacent to a semiconductor, as seen in Figure 1-8 [43-45,49,50]. For example, a ^{6}Li or ^{10}B layer can be placed adjacent to a conventional semiconductor such as silicon or gallium arsenide, to convert the neutrons into ^{7}Li and ^{4}He ions. Some of the ions enter the semiconductor creating electron and hole pairs that can be subsequently detected. McGregor *et al* [43-45] reported perforated silicon diode devices backfilled with neutron reactive conversion layers. The basic configuration consists of a Schottky barrier or *pin* junction silicon diode, in which the diode is permeated with perforations that are backfilled with neutron reactive materials. While these detectors show promise as neutron detectors, they are still limited by two factors, namely, the energetic particles

lose energy in the conversion layer (limiting efficiency to 50-60%), and the inherent lifetime limitations of Si semiconductor detectors (vulnerability to radiation damage).

High quality materials for a direct conversion detector would help to advance the technology of boron-based neutron sensors. To discover why the early devices did not perform as anticipated, information is needed about the type, concentration, and densities of specific impurities and defects present.

Beta Voltaic Devices

There is an increasing need for improved batteries in the consumer and military sectors where reliability, longevity, and durability are primary concerns [51-53]. Chemical batteries have many advantages: instantaneous power, low unit cost, wide variety of applications, etc. However, chemical batteries also have disadvantages: relatively short lifetimes (1-3 years), the inability to scale to very small sizes, hazardous chemicals, etc [51]. Traditional batteries utilize chemical reactions for power generation and storage, and have lifetimes on the order of months (or years if no load is applied). Chemical battery lifetimes are extended by the use of secondary (rechargeable) batteries, but even the best secondary batteries are limited to a lifetime of 1-3 years [51-53]. The limitations on lifetime and scaling could be addressed with beta or alpha voltaic batteries.

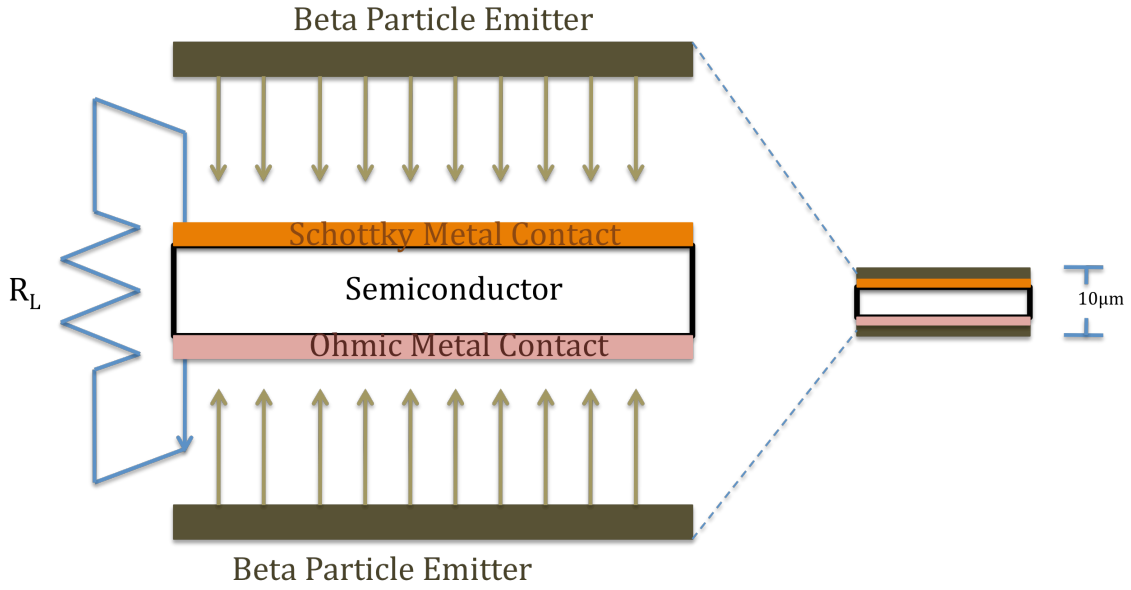

Figure 1-9 – Design for a planar beta voltaic device illustrating how the device works and how they can be scaled to micro sizes [51-53].

Radioisotope batteries convert nuclear radiation to electricity, which enables scaling to very small sizes, as seen in Figure 1-9. Additionally, radioisotope batteries have lifetimes from 10-100 years depending on the radiation source and solid-state material. This extended lifetime is a function of the half-life of a radioisotope. The half-life of an isotope is the amount of time required for half of the mass of the Parent element to decay to a daughter element, or a combination of daughter elements. Half-lives for radioisotopes cover a wide range of time (^{228}Pu – 10 ms, ^{238}U – 4.4x10^{9} y), and can include many radioactive daughter products [54]. Radioactive materials follow a unique decay chain that begins with the parent atom, which is radioactive, and ends with a daughter atom that is not radioactive. The decay chain can be simple like ^{63}Ni, which decays in one step to ^{63}Cu by a beta particle emission, or complex like ^{238}U, which decays in 33 steps to ^{206}Pb [54].

The electrical energy of a radioisotope battery is produced from radioactive materials decaying by a suitable energy conversion process. Theoretically, any kind of radiation (alpha, beta and low energy gamma/x-rays) can be used to produce electricity, see Table 1-4. For a long-lived semiconductor-based device, however, beta-emitting radioisotopes are most suitable because semiconducting materials are susceptible to the point defect damage caused by alpha particles, and there are no known low-energy gamma/x-ray emitting isotopes that have a long enough half-life to satisfy the device lifetime requirement [51].

Beta particles are high-energy electrons created when a neutron decays into a proton. There are actually three particles produced during beta decay: beta particles, protons, and antineutrinos. Antineutrinos only weakly interact with matter, and therefore are commonly ignored. The division of energy between the three particles causes beta particles to be emitted with energies ranging over a continuous spectrum from nearly zero up to maximum energy depending only the radiation source. The maximum energy of a single beta particle emission equals the difference in rest energies between the parent atom, the daughter atom, and the electron. In order to obey the law of conservation of electric charge, the previously neutral neutron takes on a positive charge, which forms a proton. From the addition of a proton, the daughter atom has one atomic number greater than the parent atom. The maximum energy of a beta particle can exceed 2 MeV (^{90}Y – 2.27 MeV), however most maximum energy emissions are <500 keV (^{63}Ni – 67KeV) [54].

Table 1-4 – Properties of radioactive isotopes; note that not all of the sources are mono-energetic. The gray-filled boxes represent the most commonly utilized radioisotopes, and the yellow-filled box indicates a valuable isotope that is not used because the kinetic energy is high enough to permanently damage beta voltaic batteries [51,54].

Radioisotope	Half-Life (yr)	Energy (MeV)	Specific Power (W/g)	Ci/g
Cf-251: α,γ	898.4	5.7	0.053	2
Cm-248:α	3.4E+05	4.65		
Cm-243:α,γ	29.0	5.8	1.7	52
Cm-244:α,γ	18.0	5.8	2.7	81
Am-241:α,γ	435.0	5.5	0.1	3
Pu-241:α,β,γ	14	4.9	3.2	103
Pu-238:α,γ	86.4	5.6	0.6	17
U-232:α,γ	70.0	5.3	0.7	22
Ac-227:α,β,γ	21.0	0.0679		72
Pm-147:β,γ	2.6	0.062	0.34	927
Cs-137:β,γ	30.2	0.662	0.048	87
Sr-90:β	28	0.9	0.75	139
Tc-99:β,γ	2.14E+05	0.085		
Mo-99:β,γ	7.50E+05	0.0176	48.9	4.8E+5
Kr-85:β,γ	10.75	0.687		400
Ni-63:β	100	0.067	0.55	10
Co-60:β,γ	5	2.50442	16.6	1,130
H-3:β	12.3	0.0057	0.3	9,664

When a beta particle enters a solid-state material a portion of the particle kinetic energy is lost to the lattice while the remainder creates electron-hole pairs all along the particle range; the current is the manifestation of the energy conversion process. The voltage of the device is a function of the generation current, the semiconductor band gap, and the *p*- and *n*-doping levels [50]. As stated previously, the radiation damage threshold is a concern for almost all radiation detectors because of the generation of Frenkel defects within the lattice. The same problem is a major limitation for the advancement of radioisotope batteries as well [53]. It is for this reason that only very low energy radiation sources (^{63}Ni – 67 keV) can by used to power beta voltaic devices [52]. However, $B_{12}As_2$ is well known to "self-heal" from radiation damage when irradiated with alpha particles of up to 1MeV [12,13]. Beta voltaics made with boron arsenide should have the unique advantage of using higher energy beta particle emitters (^{90}Sr – 900KeV)

as sources. Thus they should be able to produce more power, and be alternatives for a wider range of applications.

To compete with chemical batteries, radioisotope batteries need to both exceed the power output and have an equivalent cost. However, even the most efficient materials, if scaled to a AA battery size and power output, would probably cost many tens of thousands of dollars; compared to a Ni/Cd secondary battery that only cost ~$2. Current power output values indicate that beta voltaic batteries can compete with chemical batteries on the micro scale, but improvements in the semiconductor materials need to be made to increase the power output allowing for use of higher energy isotope sources.

Social skepticism about the dangers of radiation will remain a major impediment, limiting the wide-scale commercialization of these devices. [51-53]. Operating under the assumptions that the materials (both semiconductor and radioisotope) are abundantly available, the radiation is permanently sealed inside the battery, and radioisotope batteries will only have equivalent regulatory restrictions; radioisotope batteries are suited for long autonomous electronic circuits such as GPS satellites, sensor data transmission, and military devices where cost is less of a concern [51,52].

CHAPTER 2 - ANALYSIS TECHNIQUES

There are no ideal crystals; all crystals contain some defects, impurities and inhomogeneities. Most of the properties of a material are sensitive to the deviation from ideality; therefore the characterization of grown crystals is a necessity in order to understand why a material has its specific properties.

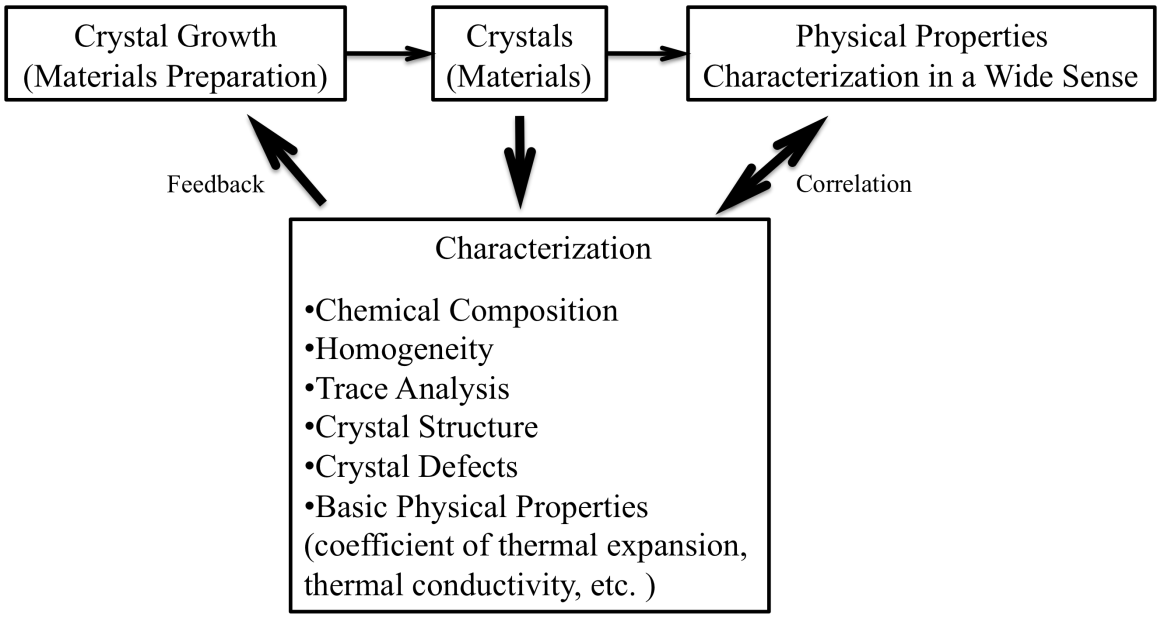

Figure 2-1 –Interrelation between crystal characterization, growth and properties [40].

The relationship between crystal growth (or materials preparation), characterization and physical properties is depicted in Figure 2-1. Careful characterization should be made of representative crystals, and the resulting information used by the crystal grower to optimize the growth technique. In the present work, the combined use of SEM, EDS, XPS, SIMS, XRD, SWBXT, Raman spectroscopy, the Hall effect, and the thermal conductivity was employed for the characterization of $B_{12}As_2$ crystals.

Scanning Electron Microscope (SEM) and Energy Dispersive X-ray Spectroscopy (EDS)

In a scanning electron microscope (SEM), images of the sample surface are generated from a high-energy beam of incident electrons scanned in a raster pattern. The signals result from interactions of the electron beam with atoms at or near the surface of the sample, and contain information about the topography, composition, and electrical conductivity of the surface. The

energy of the incident electrons in the SEM are typically in the 5–30 keV range, although there is occasion to use lower values near 1 keV for insulating samples [55-58].

Modern instruments can resolve features less than ~1 nm across, while retaining crisp focus throughout a range of several microns in the vertical direction. However, the resolution realized during microprobe detection is typically much worse because the points of origin for the detected signal are distributed throughout the excited volume [55-58]. As a rule of thumb, one can expect about 1μm resolution in this case, regardless of the initial probe diameter.

There are a variety of signals generated by the electron beam in an SEM, and perhaps the most useful are the secondary and back scattered electrons, as these are used to form the images. The x-ray emissions are also useful for examining compositions. x-ray detectors are found on nearly all electron microscopes today enabling accurate identification of high atomic weight (Z) elements ($Z \geq 23$), and some low Z ($Z \geq 4$-6) materials, in the periodic table with minimal investment in new equipment. Early detectors were of the wavelength dispersive (WDS) type [55-58] and even today offer superior spectral resolution relative to the simple and more compact energy dispersive detector (EDS).

By combining high spatial resolution, depth of field in the same image, and minimal sample preparation SEM/EDS systems are versatile tools for examining the microstructure and compositions of solid surfaces [55-58].

X-ray Photoelectron Spectroscopy (XPS)

The purpose of x-ray photoelectron spectroscopy (XPS) is to determine the chemical composition and bonding on the surface of a material. In XPS, x-rays strike the surface of a sample in an ultrahigh vacuum environment. The emission process was described by Berglund and Spicer [59] as a three-step model. First an x-ray or UV photon is absorbed and an electron is promoted from the ground state to the final state above the Fermi level. The final state lies within the potential field of the solid and satisfies the Schrodinger equation for that field. Second an electron is transported, and third, the electron escapes into the vacuum. Since the electron is generated within the potential of the solid, the wave function contains contributions from the solid even after it has escaped into the vacuum [59].

XPS is a surface-specific technique in that the information obtained originates from within the outermost 6 nm of the sample. The incident photons penetrate deeply, and do not

govern the depth specificity. The deciding factor is the attenuation length of the photoelectrons, which is a function of photoelectron kinetic energy (KE) for elements, inorganic compounds, and organic compounds [59].

XPS can provide good compositional information, but only if the sample is homogeneous. Except for pure metals, relatively few samples have homogeneous near-surface regions, and the matrix effect (the spatial distribution of elements in the near-surface region of a homogeneous sample) can have a very large effect on peak intensities [59]. Therefore, any quantification based on the assumption of homogeneity must be viewed with great caution. A useful way of reporting comparative XPS data is by way of peak –area ratios. Such ratios contain both composition and matrix effects, of course, but the use of ratios tends to minimize those effects, and the resulting relative compositions are more accurate than those based on the assumption of homogeneity [59].

XPS provides information about the composition, chemical state, electronic structure, and geometrical structure, which are all important factors that can be used to improve the design of a crystal growth system. XPS is widely used for the study of solid surfaces both in fundamental scientific studies and in applied studies of polymers, ceramics, heterogeneous catalysts, metals and alloys, semiconductors, nano-particles, biomaterials, etc [59].

Secondary Ion Mass Spectrometry (SIMS)

Secondary ion mass spectroscopy (SIMS) offers a unique combination of small analytical spot and high sensitivity for detecting dopants and trace impurities in $B_{12}As_2$ crystals. As the surface is etched, atoms and molecules are liberated, which make up the detected signal, making it ideally suited for profiling beneath the surface as erosion takes place.

The ion sputtering process can be understood in qualitative terms, but is difficult to predict and model in detail because of the arbitrary way that the etching method proceeds [55,60-63]. Hence, carrying out quantitative analysis is completed with the aid of a set of carefully prepared reference standards. Ideally, the standards must be as close to the unknown as possible, both in dopant or impurity level and in matrix composition. In the optimum case, precisions near 1%–5% can be realized, based on custom standards prepared by ion implantation [60-63].

The rate of removal of material from the surface may vary from several micrometers per minute to a single monolayer every one or two hours. The high rates liberate more secondary

ions and result in the best sensitivity for impurities and dopants, usually at the parts-per-million atomic (ppma) level. High sputter rates define the mode of operation known as dynamic SIMS, which is commonly used for qualifying the performance of ion implanters in manufacturing, for example. The collision cascade results in the ejection and ionization of atoms and molecules from the surface layers of the sample. These secondary ions are accelerated into a double focusing mass spectrometer where they are separated according to their energy and mass/charge ratio before being detected [60-63].

Most SIMS techniques are destructive, but each offers exceptional sensitivity because there is little or no background. This applies to all elements in the periodic table, including H, C, and O, although these are also common contaminants found in the vacuum environment. SIMS works especially well for verifying dopant distributions prepared by diffusion or ion implantation, and in favorable cases is capable of reaching parts-per-billion-atomic (ppba) sensitivity [60-63].

X-ray Diffraction (XRD) and the Coefficient of Thermal Expansion

X-ray diffraction (XRD) techniques are able to directly identify the structure of crystalline and polycrystalline semiconductor powders, thin films, and substrates. XRD also provides unique information about strain, grain size, crystalline phases, and preferred orientation. The primary requirement for successful x-ray diffraction is that the samples contain single-crystal or polycrystalline components. On the sub-nanometer scale, samples are composed of parallel lattice planes that are spaced at regular intervals. The condition for constructive interference of x-rays of wavelength (λ) is given by Bragg's law in equation (1)

$$\lambda = 2d_{hkl}\sin\theta_{hkl} \qquad (1)$$

where d is the spacing between the planes in the atomic lattice and θ is the angle between the atomic planes and the incident (and diffracted) beam [55,64-67].

When measurements are taken with varying temperature, XRD spectra can be used to calculate the coefficient of thermal expansion. The coefficient of thermal expansion is a valuable factor in crystal growth because, in addition to the lattice constants, it indicates if a material will be a good substrate for epitaxial experiments. If the lattice constants of a possible substrate is too dissimilar to the desired thin film, the epitaxial layer will have poor structural quality. The same could happen if the coefficients of thermal expansion are very different (± one order of

magnitude) [64-67]. The volumetric and linear coefficients of thermal expansion are given, respectively, by equations (2) and (3) [64-67]

$$\alpha_V = \frac{1}{V}\left(\frac{\partial V}{\partial T}\right)_P \tag{2}$$

$$\alpha_L = \frac{1}{L}\left(\frac{\partial L}{\partial T}\right)_P \tag{3}$$

If the expansion coefficients do not change much over the temperature range, these equations can be estimated by equations (4) and (5) [64-67]

$$\alpha_V = \frac{1}{V}\left(\frac{\Delta V}{\Delta T}\right) \tag{4}$$

$$\alpha_L = \frac{1}{L}\left(\frac{\Delta L}{\Delta T}\right) \tag{5}$$

The coefficient of thermal expansion is one of the few thermodynamic values that can be measured directly. Using x-ray diffraction, the lattice constants can be measured over a temperature range, and the thermal expansion can be directly observed. The two main directions, parallel and perpendicular to the c axis of the unit cell, are calculated from equations (6) and (7) [64-67].

$$a_{\perp}(T) = \frac{a - a_{293}}{a_{293}(T - 293)} \tag{6}$$

$$a_{\parallel}(T) = \frac{c - c_{293}}{c_{293}(T - 293)} \tag{7}$$

Procedures and tools for evaluation of x-ray powder patterns rely on the reference powder diffraction file (PDF) published by the Joint Committee on Powder Diffraction Standards (JCPDS) of the International Centre for Diffraction Data (ICDD) [55].

X-ray Diffraction Topography (XRT)

X-ray topography (XRT) is the general term for a family of x-ray diffraction imaging techniques, which is capable of providing information on the nature and distribution of structural defects in single crystal materials. The local changes in spacing and rotations of these planes are detected, rather than the external surface topography [55,67,68]. This technique is usually nondestructive and suitable for studying single crystals of large cross-section areas, with thickness ranging from hundreds of microns to several millimeters.

XRT refers to a detailed mapping of the physical features of a crystalline solid, such as a wafer, either throughout the bulk or in the near surface region, depending on the camera used. The images formed reveal surface relief, wafer warpage, small changes in crystallographic orientation, strains associated with epi-films and lattice defects, oxygen precipitates, and thermal process deformations.

The lateral resolution in topography is limited not by wavelength of the x-rays but by grain size of the recording medium, which for the best nuclear emulsion films is about 1μm [55,67,68]. Although this is clearly inadequate for direct imaging of point defects, dislocations, and atom aggregates, the strain fields associated with these imperfections generally extend over distances of several micrometers or more and can thus be detected. The superior strain sensitivity of double and triple crystal configurations derives from the low divergence of x-rays presented to the sample by a high-quality reference crystal [55,67,68].

In x-ray diffraction topography, a collimated area-filling ribbon of x-rays is incident on the single crystal sample at a set Bragg angle, and the corresponding area-filling diffracted beam is projected onto a high-resolution x-ray film or detector. The two-dimensional diffraction spot thus obtained constitutes an x-ray topograph, and it precisely displays the variation of the diffracted intensity as a function of position, depending upon the local diffracting power as well as the prevailing overall diffraction conditions [55,67,68]. Local diffracting power is affected by the distorted regions surrounding a defect, leading to differences in intensities between these regions and the surrounding more perfect regions. The variation in intensity can be characterized from the specific contrast produced by the way defects distort the local crystal lattice, and thereby the local diffracting power. The absence of magnification enables the correlation of the relative position of the image of a defect and the location inside the crystal [55,67,68]. For crystals with sufficiently low dislocation densities, standard Burgers vector analysis, which enables the determination of the direction of the Burgers vector, is readily carried out in the low absorption regime, using the $\mathbf{g} \bullet \mathbf{b} = 0$ criterion for invisibility of screw dislocations, and the combination of $\mathbf{g} \bullet \mathbf{b} \times \mathbf{1} = 0$ and $g \bullet b = 0$ criterion for invisibility of edge or mixed dislocations (where **b** is the dislocation Burgers vector, and l is the dislocation line direction) [55,67,68].

Quantitative information, such as the line direction and Burgers vector of a dislocation, can be obtained by detailed interpretation of the variations in contrast, obtained under different diffraction conditions. The technique is rapid; several high-resolution topographs are made on ~l

μm in an exposure time as short as 1 s. Topography measuring stations are available and used in all major synchrotron radiation facilities around the world [55,67,68].

Raman Spectroscopy

Raman spectroscopy provides a fingerprint by which the solid can be identified. The Raman effect occurs when photons impinge upon a molecule or crystalline solid and interact with the electron cloud and chemical bonds. For the spontaneous Raman effect, which is a form of light scattering, a photon excites the electron from the ground state to a virtual energy state [69]. When the electron relaxes, a photon is emitted and the electron returns to a different rotational or vibrational state. The difference in energy between the original state and the new state leads to a shift in the frequency of the emitted photon away from the excitation wavelength. If the final vibrational state of the solid is more energetic than the initial state, then the emitted photon will be shifted to a lower frequency so the total energy of the system remains balanced; designated as a Stokes shift. If the final vibrational state is less energetic than the initial state, then the emitted photon will be shifted to a higher frequency; designated as an Anti-Stokes shift. Raman scattering is an example of inelastic scattering because of the energy transfer between the photons and the molecules during the interaction [69].

A change in the molecular polarization potential — or amount of deformation of the electron cloud — with respect to the vibrational coordinate is required for a solid to exhibit a Raman effect. The amount of the polarizability change will determine the Raman scattering intensity. The pattern of shifted frequencies is determined by the rotational and vibrational states of the sample [69]. Raman spectroscopy is commonly used in chemistry, since vibrational information is specific to the chemical bonds and symmetry of the solid [69]. Furthermore, Raman spectroscopy also indicates whether the specimen is strained, from shifts in the peak position, and the crystal quality by the width of the peaks, the narrower the peaks the better the material quality.

Van der Pauw and the Hall Effect

The overall benefit of measuring the Hall effect is to calculate the resistivity (ρ), mobility (μ), and conductivity type (*p* or *n*). The basic physical principle underlying the Hall effect is the Lorentz force, which is a combination of two separate forces: the electric force and the magnetic

force. When an electron moves along the electric field direction perpendicular to an applied magnetic field, it experiences a magnetic force acting normal to both directions. The resulting Lorentz force **F** is therefore equal to - q(**E** + **v** x **B**) where q (1.602×10^{-19} C) is the elementary charge, **E** is the electric field, **v** is the particle velocity, and **B** is the magnetic field [70-74], as seen in Figure 2-2.

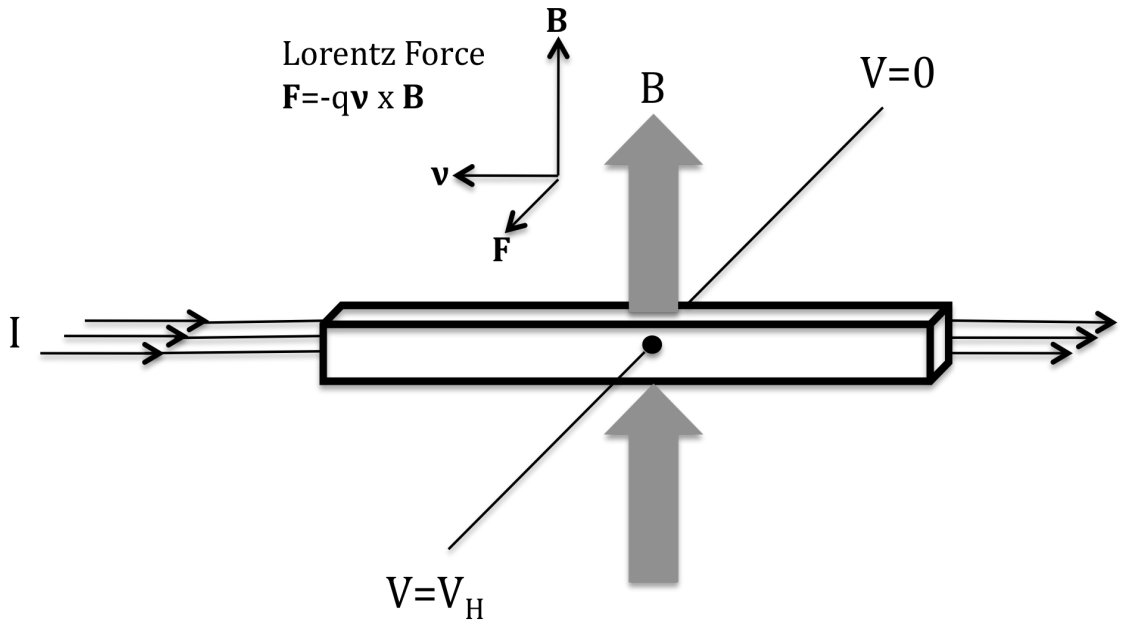

Figure 2-2 - Schematic diagram depicting the Hall effect measurement.

Assuming that a constant current (I) flows along the x-axis from left to right in the presence of a z-directed magnetic field then electrons are subjected to the Lorentz force and initially drift away from the current direction toward the negative y-axis, resulting in an excess negative surface electrical charge on this side of the sample. The resulting charge is the Hall voltage (V_H), a potential drop across the two sides of the sample. The magnitude of the Hall voltage is equal to *IB/qnd*, where *I* is the current, *B* is the magnetic field, *d* is the sample thickness, and *q* (1.602×10^{-19} C) is the elementary charge. If the conducting layer thickness d is known, the sheet density ($n = n_S/d$) can be determined. The sheet density can be solved by equation (8):

$$n_S = \frac{IB}{q|V_H|} \tag{8}$$

By measuring the Hall voltage V_H and from the known values of I, B, and q, the sheet density n_s of charge carriers in semiconductors can be measured [70-74]. With the Hall voltage,

and the sheet density, one need only measure the sheet resistance to calculate the Hall mobility. The sheet resistance R_S of the semiconductor can be conveniently determined by using of the van der Pauw resistivity measurement technique. Van der Pauw demonstrated that there are actually two characteristic resistances R_A and R_B, associated with the corresponding terminals shown in Figure 2-3 [70-74]. R_A and R_B are related to the sheet resistance R_S through equation (9):

$$e^{\left(\frac{-\pi R_A}{R_S}\right)} + e^{\left(\frac{-\pi R_B}{R_S}\right)} = 1 \tag{9}$$

Which can be solved numerically for R_S. Since sheet resistance involves both sheet density and mobility, the mobility then follows from equation (10).

$$\mu = \frac{|V_H|}{R_S I B} = \frac{1}{(q n_S R_S)} \tag{10}$$

As originally devised by van der Pauw, the general setup consists of an arbitrarily shaped thin-plate sample containing four small Ohmic contacts placed on the periphery of the plate [70-74]. A schematic of a rectangular van der Pauw configuration is shown in Figure 2-3. A modification can be made to the four contacts if the sample is not very thin (>1mm), shown in Figure 2-4. For thick samples, placing the contacts over the thickness of the sample helps maintain the two dimensional current flow that van der Pauw originally described [70-74].

A second type of geometry that is sometimes used includes the parallelepiped or bridge-type sample, as seen in Figure 2-4. This geometry may be more desirable in the case of anisotropic material properties. The restrictions on shape and size are more rigid than those of the van der Pauw specimen, but measurements can be made using either a six or an eight contact configuration [70-74]. The bridge-type specimen differs from the parallelepiped in that the contacts are placed on arms that branch off the main parallelepiped base.

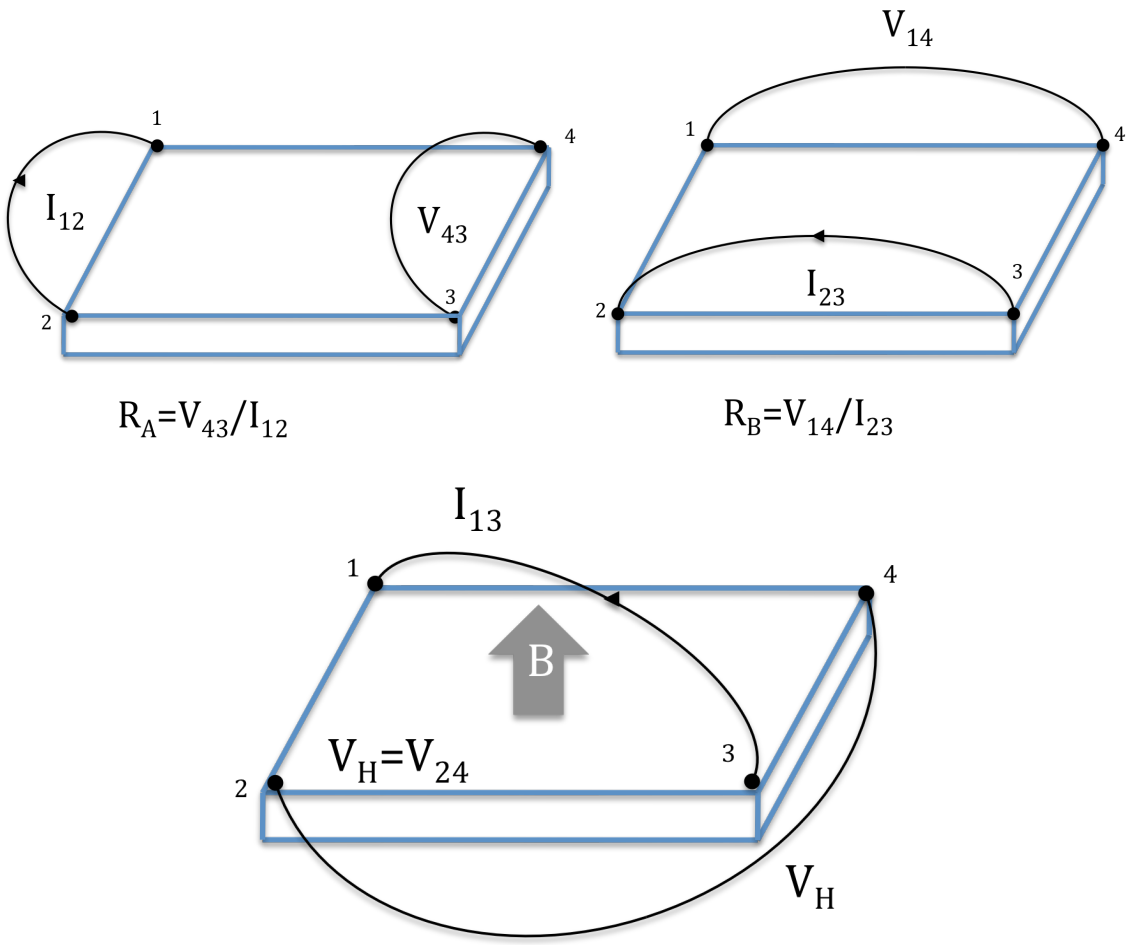

Figure 2-3 - van der Pauw four point probe setup, and depiction of measurements to determine R_A, R_B, and V_H.

There are practical aspects that must be considered when carrying out Hall and resistivity measurements. Primary concerns are (1) ohmic contact quality and size, (2) sample uniformity and accurate thickness determination, (3) thermomagnetic effects due to nonuniform temperature, and (4) photoconductive and photovoltaic effects which can be minimized by measuring in a dark environment [70-74]. Also, the sample lateral dimensions must be large compared to the size of the contacts and the sample thickness. Finally, one must accurately measure sample temperature, magnetic field intensity, electrical current, and voltage.

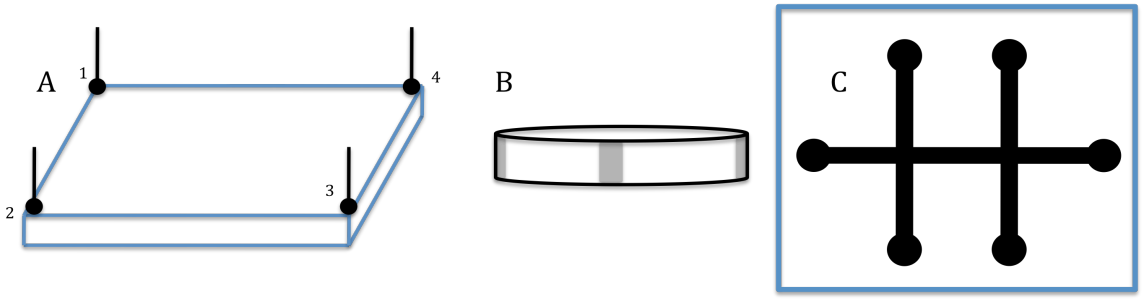

Figure 2-4 - Configurations for conducting a Hall effect measurement. A) the traditional approach is to place the contacts at the very edge of the sample. Alternatives include B) to place the contacts over the thickness of the sample, and C) to construct a "Hall Bar".

The importance of the Hall effect is supported by the need to accurately determine carrier density, electrical resistivity, and the mobility of carriers in semiconductors. The Hall effect measurement provides a relatively simple, low cost, and fast turnaround time, which makes it an indispensable characterization technique in the semiconductor industry and in research laboratories.

CHAPTER 3 - COEFFICIENT OF THERMAL EXPANSION BETWEEN 25°C AND 850°C

Abstract

The semiconductor boron arsenide has a high ^{10}B density, a wide bandgap, and a high melting temperature, all of which make it an interesting candidate for high-temperature electronic devices and radiation detectors. The present investigation was undertaken to determine the coefficients of thermal expansion for boron arsenide. $B_{12}As_2$ powder was synthesized from boron and arsenic heated in a sealed quartz ampoule at 1100 °C for 72 hrs with excess boron. Using high temperature x-ray diffraction (HTXRD) between 25°C and 850°C, the average unit cell volumetric and lattice coefficients of thermal expansion were measured perpendicular and parallel to the <111> axis in the rhombohedral setting (equivalent to the *a* and *c* axes in the hexagonal setting): $1.5x10^{-5}$ K^{-1}, $4.9x10^{-6}$ K^{-1}, and $5.3x10^{-6}$ K^{-1} respectively. [1]

[1] Submitted to the J. of the Phys. and Chem. of Sol. (2011), by C.E. Whiteley, M.J. Kirkham, and J.H. Edgar

Introduction

Wide bandgap semiconductors, such as SiC, AlN, GaN and ZnO, are attractive for high-power and high frequency electronics, short wavelength optoelectronics, and chemical, biological, and radiation sensors, which has led to a surge of research in these materials [1]. In contrast, boron compound semiconductors have rarely been studied, which is especially true of the icosahedral-structure boron-rich compounds, such as α-boron, $B_{12}P_2$, $B_{12}As_2$, and $B_{12+x}C_{3-x}$, where two or three-atom chains, As-As or B-C-B for example, lie along the <111> axis of the rhombohedral unit cell, (equivalent to the *c*-axis of the hexagonal unit cell) [1,2,3]. Icosahedral borides contain 12- boron atom clusters where the boron atoms reside on the vertices of an icosahedron, as seen in Figure 3-1. The icosahedral borides hold a unique position within chemistry because the internal bonding is based on an electron-deficient three-center bonding scheme whereby two electrons are shared among three boron atoms. The excellent strength of the three-center bonds imparts the icosahedral borides with extraordinary hardness (212GPa) and high melting temperatures, >2000°C. [1,2,3,4].

The synthesis of icosahedral $B_{12}As_2$ is only mentioned in the literature in passing; cubic BAs powder is known to decompose to $B_{12}As_2$ at high temperature (>1000 °C) and atmospheric pressure (≤1atm) [5-7]. In the past, BAs studies were primarily driven by the desire to use the powder as a source material for single crystal growth of cubic BAs [5-7]. Similarly, in this work, $B_{12}As_2$ was synthesized in order that it may be used as a source material in the single crystal growth of icosahedral boron arsenide.

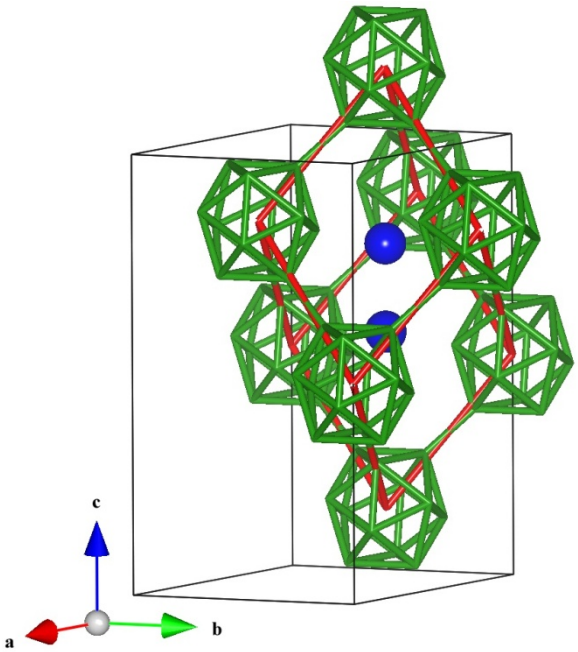

Figure 3-1 - Rhombohedral unit cell of $B_{12}As_2$, shown in red, with icosahedral boron clusters (in green) at the vertices and As-As (in blue) chains along the body diagonal, the rhombohedral [111] direction, and also showing the relationship to the axes and unit cell (in black) of the hexagonal setting.

In addition to the synthesis method, the coefficient of thermal expansion of $B_{12}As_2$ has a significant influence on both solution growth and chemical vapor deposition (CVD). Reports show that thin films of $B_{12}As_2$ grown on foreign substrates are not of the high-quality material necessary for good devices. $B_{12}As_2$ has been deposited on various substrates including silicon and silicon carbide (4H-SiC, 6H-SiC, 15R-SiC), but crystalline defects and contamination from the substrate form during the crystal growth, which degrades the properties of the film [1]. Bowing and cracking in $B_{12}As_2$ films suggests that the coefficient of thermal expansion is significantly different than the values for the Si and SiC substrates, but a comparison has never been reported. The crack density increases with film thickness, ultimately resulting in the films delaminating from the substrate, occurring in $B_{12}As_2$ films as thin as 4 to 5 μm [1].

The coefficient of thermal expansion (CTE) describes the lattice expansion with temperature [8]. The anisotropy of the icosahedral borides requires that the lattice coefficients of expansion in multiple crystallographic directions be examined. From the lattice CTE values, the lattice volumetric expansion can be calculated.

The volumetric and linear coefficients of thermal expansion are given, respectively, by equations (1) and (2) [8,9].

$$\alpha_V = \frac{1}{V}\left(\frac{\partial V}{\partial T}\right)_P \tag{1}$$

$$\alpha_L = \frac{1}{L}\left(\frac{\partial L}{\partial T}\right)_P \tag{2}$$

If the expansion coefficients do not change much over the temperature range, the equations can be estimated by equations (3) and (4) [8,9].

$$\alpha_V = \frac{1}{V}\left(\frac{\Delta V}{\Delta T}\right) \tag{3}$$

$$\alpha_L = \frac{1}{L}\left(\frac{\Delta L}{\Delta T}\right) \tag{4}$$

Using x-ray diffraction (XRD), the lattice constants can be measured over a temperature range, and the thermal expansion can be directly calculated. The thermal expansion in the two main directions, parallel to the *a* and *c* axes of the hexagonal unit cell, are calculated from equations (5) and (6) [10].

$$\alpha_a(T) = \frac{a - a_{293}}{a_{293}(T - 293)} \tag{5}$$

$$\alpha_c(T) = \frac{c - c_{293}}{c_{293}(T - 293)} \tag{6}$$

Note that 293 K is used by convention as the reference temperature for thermal expansion coefficients. Tsagareishvili *et al* [10], Rice [11] and Yakel [12] completed thorough investigations of the coefficient of thermal expansion of boron carbide, reporting an average CTE for the *a* direction of 5.73×10^{-6} K^{-1} (25-940 °C), 5.29×10^{-6} K^{-1} (25-600 °C) and for the c direction of 5.65×10^{-6} K^{-1} (25-940 °C), and 6.25×10^{-6} K^{-1} (25-600 °C) [11]. Anisotropy in boron carbide of up to 15% can be explained by the differences in the *a* and *c* directions of the hexagonal structure [10-12]. The strong covalent bonds of the icosahedral should show less flexibility than the bonds between the carbon atoms parallel to the *c* axis.

Boron carbide and boron arsenide have the same space group (R-3m) and similar boron-to-boron bonds between boron icosahedra, thus it is expected that the coefficients of thermal

expansion should also be comparable, and anisotropic. For that reason, the coefficients of thermal expansion of $B_{12}As_2$ powder were measured by HTXRD between 25 and 850 °C.

Experimental Methods

$B_{12}As_2$ powder was synthesized by a method similar to that described by Ku [5]. The fine powder boron (99.999%) and arsenic (99.999%) source materials were first weighed (150g each) and placed in the unsealed quartz ampoule, separated by 15cm. The tube was then evacuated to 10^{-6} torr, and heated to 125 °C for 5h to remove any residual contaminates that were absorbed on the surface of the powders. After the baking cycle, the ampoule was sealed and inserted into a horizontal resistance heater, as seen in Figure 3-2. The boron was maintained at 1100 °C, and the arsenic was held at 600 °C (creating an As vapor pressure of approximately 0.5 atm) [13]. After 72h the ampoule was cooled to room temperature. XRD measurements were then taken to confirm the phase purity of icosahedral boron arsenide, and identify any peaks that were due to residual impurities.

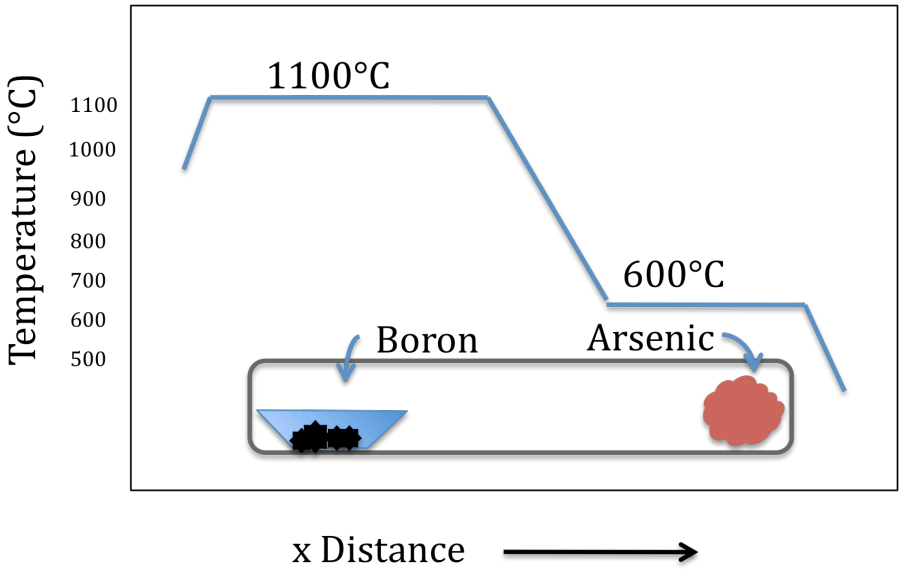

Figure 3-2 - Temperature profile of the resistance heater during the synthesis of $B_{12}As_2$ powder. Notice the boron is held in the hot zone and the arsenic is held in a cooler zone (to maintain 0.5atm).

In order to monitor the crystal structure of $B_{12}As_2$, high temperature X-ray diffraction measurements were carried out on both heating and cooling between 25 °C and 850 °C in 1 atm of N_2. A PANalytical X'Pert Pro MPD X-ray diffractometer with automatic divergence slits and a position sensitive detector was employed to record the diffraction data in the 2θ range 10–140°

with a step of 0.0167 degrees. The X-ray source was Cu Kα with a wavelength of 1.54060 Å. The accelerating voltage was 45 kV and the current was 40 mA. The samples were heated with an Anton Paar XRK 900 reaction chamber under a flow of N_2. The heating rate was 25 °C min^{-1} between data collection steps at 25 °C, every 100 degrees between 100 and 800 °C, and at 850 °C. After the measurements were taken, the data were analyzed with JADE v.3.5 software [MDI, Livermore, CA], and the spectra were analyzed to determine the change in lattice parameters as a function of temperature. The precision of the lattice parameters was 0.0002Å and the temperature error was ±2 °C.

Results and Discussion

The synthesis of $B_{12}As_2$ is easily accomplished in sealed quartz ampoules at 1100 °C and 0.5 atm. The XRD analysis at room temperature revealed high purity boron arsenide powder with all diffraction peaks matching the known $B_{12}As_2$ structure (Inorganic Crystal Structure Database #68151), as seen in Figure 3-3. While examining the $B_{12}As_2$ powder at high temperature, no fundamental changes in the spectrum took shape. Decomposition from boron arsenide to pure boron would be observed by the appearance, and increase in intensity, of new peaks as the temperature approached 850 °C; however, no new peaks were observed. The XRD spectra before and after heating show no changes, as seen in Figure 3-3.

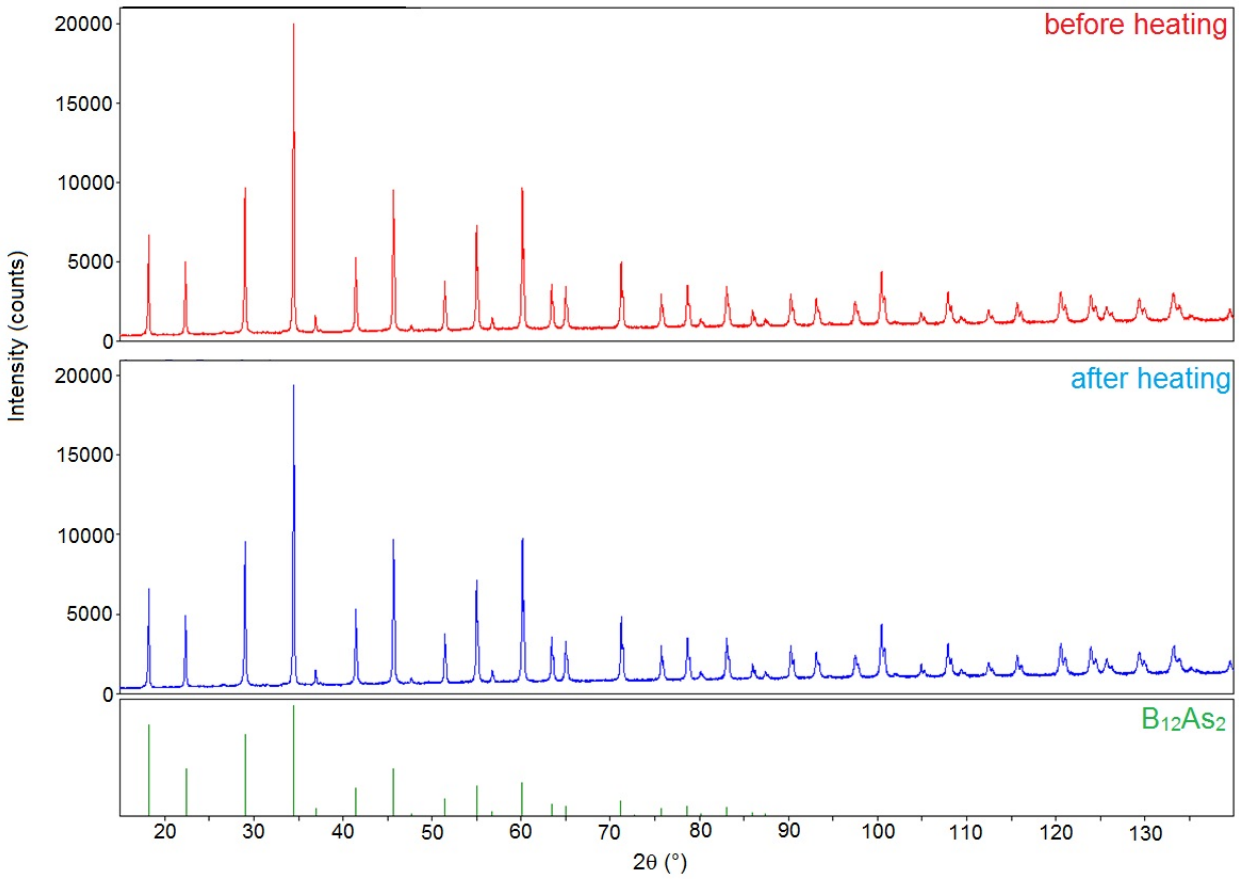

Figure 3-3 - Room temperature XRD spectrum for $B_{12}As_2$ powder before (top) and after (bottom) heating to 850°C. All peaks were identified to be associated with boron arsenide, by comparison with the $B_{12}As_2$ reference pattern at the bottom.

The lattice parameters of the $B_{12}As_2$ powder increased with temperature between 25 °C and 850°C, fitting closely to quadratic curves (R^2 = 0.9999). The volumetric and linear coefficients of thermal expansion determined from the lattice parameters for $B_{12}As_2$ powder are shown versus temperature in Figure 3-4. Their relationships with temperature were fitted using a least-squares regression; the equation and values are given in Table 3-1.

Table 3-1 - Coefficients of thermal expansion for $B_{12}As_2$ (25-850°C).

	α average (10^{-6} K^{-1})	α_0 (10^{-6})	α_1 (10^{-9})	α_2
a axis	4.9(6)	4.21(6)	1.30(6)	-0.12(1)
c axis	5.3(7)	4.9(1)	1.2(1)	-0.20(1)
volume	15(2)	13.3(2)	3.9(2)	-0.44(2)

The average coefficients of linear expansion of the *a* and *c* axes were $4.9x10^{-6}$ K^{-1}, and $5.3x10^{-6}$ K^{-1}, respectively. There was some anisotropy between the axes, with a 10% difference in the coefficient of thermal expansion for the *a* and *c* axis, which is similar to what was found for $B_{12}As_2$ in a diamond anvil compression study [16], and with boron carbide [10-12]. This anisotropy is significant because it shows the fundamental difference in properties that exists in these two different directions in the $B_{12}As_2$ crystal structure.

The large average volumetric thermal expansion coefficient ($1.5x10^{-5}$ K^{-1}) suggests that in the solution growth of $B_{12}As_2$ crystals, a low cooling rate (<3 °C/h) should be adopted. Otherwise, the difference in the coefficient of thermal expansion between the crystals and the nickel solvent ($1.34x10^{-5}$ K^{-1}) will cause the crystals to be compressed and possibly crack [14,15]. Additionally, the coefficient of thermal expansion for $B_{12}As_2$ was proposed as one reason for the poor quality of the heteroepitaxially grown layers [1]. The coefficient of thermal expansion for Si and SiC are $2.6x10^{-6}$ K^{-1} and $2.77x10^{-6}$ K^{-1}, respectively [17,18]. This is a difference of 59% and 56%, respectively, from the values in this paper for $B_{12}As_2$, which is is significant, and quite clearly indicates that bowing and cracking would result during the cooling of a $B_{12}As_2$ film on a Si or SiC substrate.

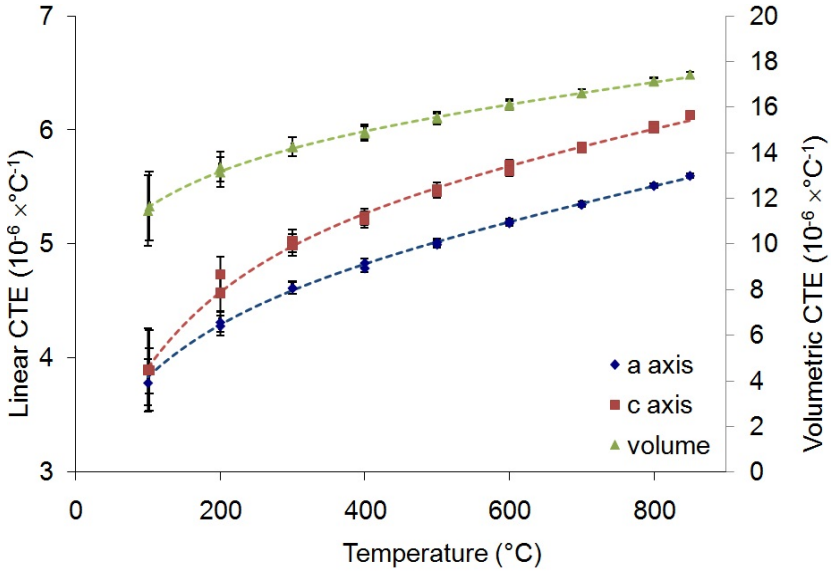

Figure 3-4 - Linear and volumetric coefficients of thermal expansion of $B_{12}As_2$ as a function of temperature. Note the large value of the volumetric coefficient (right axis) and the anisotropy of the perpendicular (*a* axis) and parallel (*c* axis) coefficients (left axis). The dotted lines are fits to the data of the form $\alpha=\alpha_0+\alpha_1*T+\alpha_2/T^2$, with the values of α_0, α_1 and α_2 given in Table 3-1.

Conclusions

The coefficients of thermal expansion of icosahedral boron arsenide ($B_{12}As_2$) powder were calculated from HTXRD data up to 850 °C. The average coefficients of linear expansion of the *a* and *c* axes were $4.9x10^{-6}$ K^{-1}, and $5.3x10^{-6}$ K^{-1} respectively. HTXRD revealed a large volumetric coefficient of thermal expansion ($1.5x10^{-5}$ K^{-1}), and a 10% anisotropy between the *a* and *c* directions. The expansion data exposes the importance of a slow cooling rate during the flux growth method, and the large difference between $B_{12}As_2$ and Si or SiC (common substrates for thin films) is likely the cause of the strain and cracking of the $B_{12}As_2$ thin films which has been experimentally observed [1,19].

Acknowledgements

Financial support was supplied by the National Science Foundation (CBET 0736154), the Department of Homeland Security (2008-DN-077-ARI013-03), and the II-VI Inc. Foundation. Additionally, this research was supported in part by Oak Ridge National Laboratory's SHaRE User Facility, which is sponsored by the Office of Science, U.S. Department of Energy. The X-

ray diffractometers are part of the High Temperature Materials Laboratory sponsored by the U.S. Department of Energy, Office of Energy Efficiency and Renewable Energy, Vehicle Technologies Program.

References

[1] H. Chen, Defect Structures and Growth Mechanisms of $B_{12}As_2$ Epilayers Grown on 6H-SiC and 15R-Sic Substrates, Dissertation, Stony Brook University (2008)

[2] M. Carrard, D. Emin, and L. Zuppiroli, Phys. Rev. B **51**, 11270 (1995)

[3] D. Emin, J. Solid State Chem. **179** 2791 (2006)

[4] S. Ovsyannikov, A. Polian, P. Munsch, J. Chervin, G. Marchand, and T. L. Aselage, Physical Review B **81**, 140103 (2010)

[5] S.M. Ku, Impurity Distribution in Crystals, **113** 813-816 (1966)

[6] A. Armington, Journal of Crystal Growth, **1** 47-48 (1967),

[7] J. Osugi, K. Shimizu, Y. Tanaka, and K. Kadono, The Review of Physical Chemistry in Japan, **36** 54-57 (1966)

[8] P. Tipler, and G. Mosca Physics for Scientists and Engineers, 6th Edition,
New York, NY: Worth Publishers (2008).

[9] D.L. Turcotte, and G. Schubert, Geodynamics, 2nd Edition, Cambridge, (2002).

[10] G. V. Tsagareishvili, T.G. Nakashidze, J. Sh. Jobava, G.P. Lomidize, D.I. Khulelidze, D. Tsagareishvili, and O.A. Tsagareishvili, Journal of the Less-Common Metals, **117** 159-161 (1986)

[11] R. Rice, Journal of American Ceramic Society, **73** 3116-3118 (1990)

[12] H. L. Yakel, Journal of Crystals, **6** 471 (1973)

[13] G. Rosenblatt, and P. Lee, J of Chem. Phys. **49** 2995-3006 (1968)

[14] L. Wang, W. Jie, Y. Yang, and L. Fu, Journal of Physics D: Applied Physics, **41** 085411-085415 (2008)

[15] L. Wang, Y. Dong, and W. Jie, J. Phys. D: Appl. Phys. **40** 3921 (2007)

[16] J. Wu, H. Zhu, D. Hou, C. Ji, C.E. Whiteley, J.H. Edgar, Y. Ma, Journal of Physics and Chemistry of Solids **72** 144–146 (2011)

[17] S.M. Sze, Physics of Semiconductor Devices, John Wiley and Sons, Inc, New York, (1981)

[18] G.A. Slack, and S.F. Bartram, J. Appl. Phys. **46** (1975) 89.

[19] C.E. Whiteley, A. Mayo, J.H. Edgar, M. Kuball, and Y. Zhang J. Cryst. Growth **318** 553-557 (2011).

CHAPTER 4 - Crystal Growth of $B_{12}As_2$

Abstract

Semiconducting icosahedral boron arsenide, $B_{12}As_2$, is an excellent candidate for neutron detectors, thermoelectric converters, and radioisotope batteries, for which high quality single crystals are required. Thus, the present study was undertaken to grow $B_{12}As_2$ crystals by precipitation from metal solutions (nickel) saturated with elemental boron (or $B_{12}As_2$ powder) and arsenic in a sealed quartz ampoule. $B_{12}As_2$ crystals of 10-15mm were produced when a homogeneous mixture of the three elements was held at 1150°C for 48-72 hours and slowly cooled (3.5°C/hr). The crystals varied in color and transparency from black and opaque to clear and transparent. X-ray topography (XRT), and elemental analysis by energy dispersive x-ray spectroscopy (EDS) confirmed that the crystals had the expected rhombohedral structure and chemical stoichiometry. The concentrations of residual impurities (nickel, carbon, etc) were low, as measured by Raman spectroscopy and secondary ion mass spectrometry (SIMS). Additionally, low etch-pit densities ($5x10^7 cm^{-2}$) were observed after etching in molten KOH at 550°C. Thus, the flux growth method is viable for growing large, high-quality $B_{12}As_2$ crystals.[1]

[1] Published in J. Cryst. Growth **318** (2011) 553-557, by C.E. Whiteley, A. Mayo, J.H. Edgar, M. Kuball, and Y. Zhang.

Introduction

Boron and boron compound semiconductors are of interest for neutron detectors because the boron-10 isotope has a large thermal neutron capture cross-section (3840 barns)—orders of magnitude larger than most elements [1]. Several candidates for boron containing semiconductors are listed in Table 1-1, along with the barriers to crystal growth. There are relatively few studies on the synthesis of boron-rich compounds, and even fewer crystal growth studies [2-17]. Crystals are the preferred form for obtaining the best electrical properties since the charge carrier mobility can be reduced by orders of magnitude in polycrystalline materials. The measurement of the electrical properties of the boron-based semiconductors listed in Table 1-1 is limited, and most measurements are reported on materials of undefined quality (high densities of dislocations, twins, and inclusions) [18–21]. Thus, the actual electrical properties of boron-based semiconductors could be significantly different than the reported values. Despite the lack of fundamental information on the crystallographic properties, several attempts to make neutron detectors from boron-based semiconductors are reported; however, the efficiency and stability of the reported boron devices were quite poor [22–24]; low efficiencies can be attributed to the poor quality of produced crystals.

Icosahedral boron arsenide ($B_{12}As_2$) has rarely been studied (fewer than 30 papers report any aspect of the materials), even though the unique properties of $B_{12}As_2$ make it the most promising candidate for bulk crystal growth. $B_{12}As_2$ semiconductors have several advantages over other boron-rich compounds for neutron detection [4]. The reported hole mobilities in $B_{12}As_2$ are relatively high, on the order of 50–100 $cm^2/V\ s$ [4], high enough that fabricated devices will operate efficiently. $B_{12}As_2$ also exhibits self-healing from radiation damage. Radioactive particles create interstitial-vacancy pairs, Frenkel defects, and limits the lifetime of common semiconductor detectors. However, Emin [7] and Carrard et al. [8] showed that bombarding icosahedral boride compounds with high-energy electrons (400 keV), at doses high enough to make most materials amorphous (10^{18} e $/cm^2$ s), resulted in no detectable damage. Lastly, $B_{12}As_2$ has a wide energy band gap, 3.2 eV [9], resulting in a low intrinsic conductivity (in the absence of light or neutron irradiation) and a potentially low reverse bias leakage current ($1x10^{-10}$ A).

The high melting temperature of $B_{12}As_2$ (2400 °C) [9] makes crystal growth from the melt difficult. Consequently, $B_{12}As_2$ crystals are grown by chemical vapor deposition and precipitation from molten metal fluxes at temperatures below 1300 °C in quartz ampoules. $B_{12}As_2$ was deposited on several foreign substrates including silicon and silicon carbide (6H-SiC), but the mismatch of properties creates stresses, crystalline defects, and contamination from the substrate in the thin film, all of which degrade the properties of the film [4]. To completely avoid the problems associated with CVD, and to produce the best possible electrical properties, bulk crystals with low defect densities are needed.

The feasibility of precipitating $B_{12}As_2$ crystals from metal fluxes was previously demonstrated by Slack et al. [5] and Aselage [14], but producing large crystals was not the primary concern of the research, and only resulted in the production of numerous small crystals (~1 mm). While small crystals are adequate for determining crystal structures, observing morphological characteristics, and making physical property measurements, large bulk crystals (>1 cm) are needed for device fabrication [25,26]. To produce larger crystals, the present study focused on determining the growth mechanism.

Like melt growth, flux growth also employs precipitation from a liquid, but a solution is employed, and crystals are formed by precipitation rather than by freezing. Thus, the temperature at which the crystals form can be much lower than the melting point of the source compounds. The crystals are grown when the solubility in the metal solvent decreases. Growth rates in metal fluxes must be low, an order of magnitude slower than melt growth, to avoid incorporation of the solvent into the crystal lattice [25,26].

In general, the most practical metal solvents for flux growth [27–29] (1) are readily available and safely handled, (2) dissolve sufficient quantities of solute, (3) have low solution vapor pressures at growth temperatures to prevent unwanted loss of solvent and to avoid the danger of high pressure, (4) are chemically inert with respect to container materials, and (5) are easily separable from the solute crystals. Several molten metal solutions have proven successful for the growth of boron arsenide crystals including copper, nickel, palladium, silver, and platinum [5,11– 17,30]. An examination of binary phase diagrams reveals nickel as the most promising candidate for the molten metal in the flux growth, as seen in Figure 4-1. The relatively large solubility of boron (45 mole%) at the lowest eutectic temperature (1018 °C), and the low

cost of nickel metal compared to Pd, Ag, and Pt are the primary reasons nickel was employed as the solvent in the present work.

In previous studies the $B_{12}As_2$ crystals contained high charge trap densities, which degrade the electrical properties, and consequently the device efficiency and stability. Thorough characterization of material properties is invaluable for improving crystal quality; there- fore, attention to the growth mechanism will allow optimization of the material properties to maximize the performance of devices. To advance the technology of boron-based solid-state neutron detectors, the focus was on producing low defect density boron arsenide ($B_{12}As_2$) crystals and accurately measuring the crystallographic properties

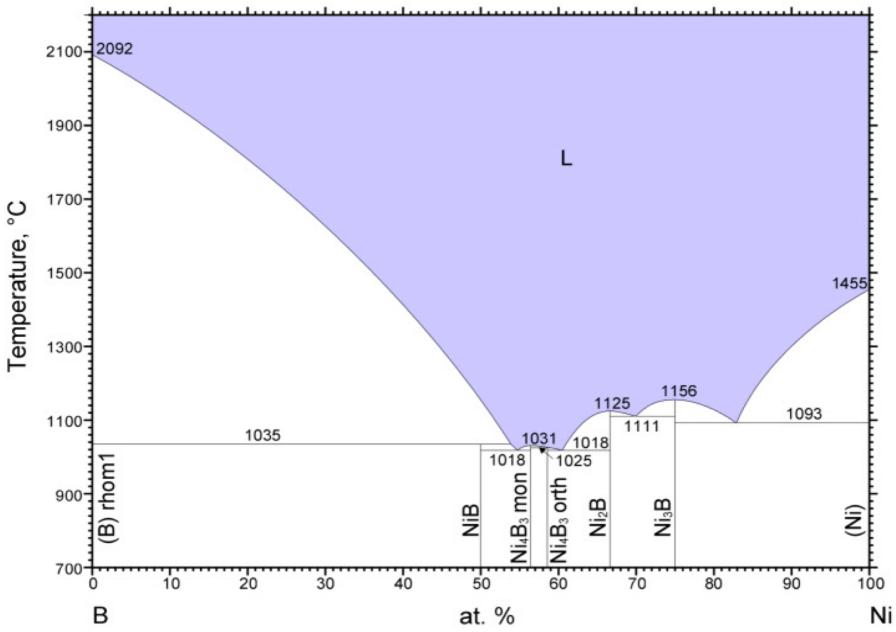

Figure 4-1 - The nickel boron binary phase diagram. The liquid phase is maintained down to the eutectic temperature of 1018°C (55mol% Ni) [34].

Experimental Methods

$B_{12}As_2$ crystals were grown in a four zone horizontal furnace, shown schematically in Figure 4-2. Two methods for preparing the flux were utilized; boron arsenide as the boron source and elemental boron as the source. First the source material, $B_{12}As_2$ (2.9 g) powder or B (3.6 g) powder, and Ni (25.8 g) powders were placed in a 15 cm long pyrolytic boron nitride (PBN) sample boat. In the case of the Ni and B, the amounts corresponded to the 1018 °C eutectic composition on the nickel–boron phase diagram. Next, As (29.1 g) was placed in the closed end

of the quartz tube, and the PBN sample boat was placed in the center of the quartz tube (approximately 15 cm from the closed end). Many other compositions were examined and the change in crystal size was observed, as seen in Table 4-1.

The tube was evacuated to 5.5×10^{-6} Torr, and, while still under vacuum, the tube was heated with a heating tape to 125 °C for one hour to evaporate excess water from the source materials. Next, the quartz tube was sealed, and placed inside a 90 cm reaction furnace; shown schematically in Figure 4-2.

To form the nickel boride before any reaction between the B and As took place, the PBN sample boat was heated to and allowed to dwell at 1150 °C for 48 h. While the nickel boride solution was held at 1150 °C, the group V material was heated to 600 °C at 12.5 °C/h (producing an arsenic vapor pressure approximately equal to 0.5 atm) [32]. The furnace was then held at temperature for 24, 48, and 72 h during which the group V material dissolved in the molten nickel boride solution and reacted to form $B_{12}As_2$ crystals. Quench cooling (>100 °C/h) and slow cooling rates (3.5 °C/h) were employed to observe the growth rate and mechanism, as seen in Table 4-2.

The crystals and metal ingot were then mechanically separated and treated with aqua regia to remove any excess nickel solvent. Next the crystals were cleaved into flat platelets. The $B_{12}As_2$ crystals were polished with a sub-micron alumina slurry, and photographs were taken in reflection and transmission. The crystals were characterized for composition and quality using secondary ion mass spectrometry (SIMS), energy dispersive X- ray spectroscopy (EDS), Raman spectroscopy, and X-ray topography (XRT). Finally, the number of defects on the crystal surface were estimated, by visually marking the $B_{12}As_2$ crystals for etch pits before and after etching with molten potassium hydroxide (KOH) at 550 °C for two minutes.

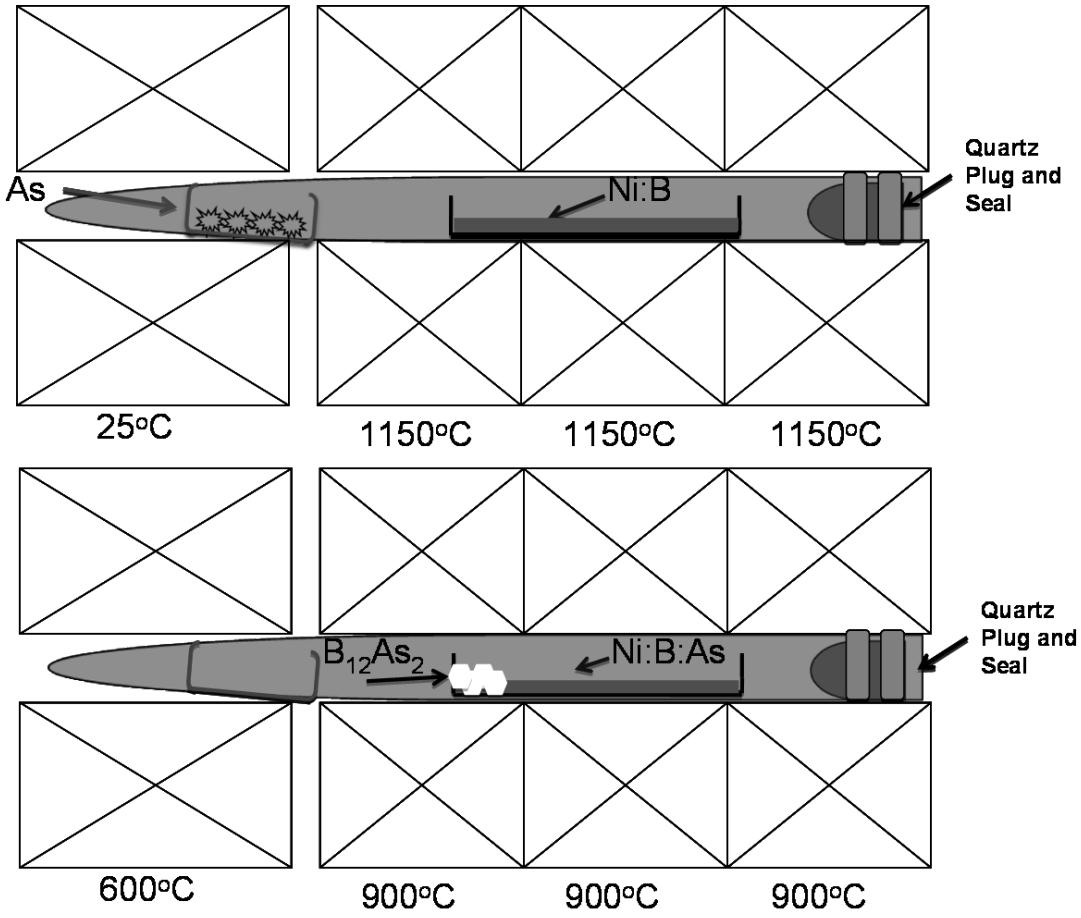

Figure 4-2 - In the first step of crystal growth, a homogeneous nickel boride liquid mixture is created by heating only the B-Ni component mixture (Top). Icosahedral boron arsenide crystal growth is initiated by subliming the arsenic, which then reacts with the boron in solution to form icosahedral boron arsenide crystals (Bottom).

Results and Discussion

Attempts to employ $B_{12}As_2$ powder as a source for crystal growth were unsatisfactory, as the solubility of $B_{12}As_2$ in Ni at temperatures less than 1150 °C was poor (> 2 mol%). Subsequently, boron powder was preferred as the starting source material. Table 4-2 lists the icosahedral boron arsenide crystal size in relation to the cooling rate and high temperature dwell time; the size represents the largest dimension of the crystals. The size of the $B_{12}As_2$ crystals increased with increasing dwell time (72 h) and slower cooling rates (3.5 °C/h).

The compositions listed are the ternary composition of the liquid alloy (boron, arsenic, and nickel at 1150 °C), and are based on the initial amount of each element placed in the

ampoule. The actual composition of the alloy could not be measured during the experiment because the amount of each element changed as a function of time as the crystals were growing. The most successful initial composition (30 mol% B, 30 mol% As, and 40 mol% Ni) corresponds to the crystals produced at the longest dwell time at 1150 °C and the slowest cooling rate. The compositions that did not result in crystal growth either had too much or too little boron, which did not allow for a homogeneous liquid, or the arsenic composition was too small.

Table 4-1 - Crystal size as a function of ternary molar composition (B:As:Ni) of the starting materials. The highlighted values are the important factors that hindered the crystal growth; boron composition too high, boron composition too low, and arsenic composition too low, respectively. Note that the listed values only represent the most interesting of the 25 tested compositions.

Crystal Size	Ternary Compositions – B:As:Ni (mol%)			Mol% B in Ni
11-15mm	29.1	33.1	37.6	43.6
8-10mm	35.0	25.0	39.9	46.7
5mm	23.5	36.4	39.9	37.1
NA	45.0	14.9	40.0	**52.9**
NA	16.9	23.2	59.7	**22.1**
NA	24.1	**16.3**	59.4	28.9

The boron arsenide crystals always formed on the end of the boat closest to the arsenic, independent of cooling rate or dwell time, as seen in Figure 4-2. The position of the crystal growth within the reaction boat can be explained by the excess amount of arsenic that dissolves first in the end of the homogeneous molten liquid closest to the arsenic. The excess arsenic then reacts, forms the $B_{12}As_2$ crystals, and precipitates out of the solution. The $B_{12}As_2$ formed crystal platelets (0.5 mm thick), and large single crystals with many facets (single crystalinity was confirmed by XRT), as see in Figure 4-3. Because the band gap of $B_{12}As_2$ is 3.24 eV the crystals should be transparent and colorless, and some crystals were transparent, but most were black and opaque.

After polishing, the crystals were analyzed with SIMS, EDS, Raman, defect selective etching (DSE), and X-ray topography (XRT). The SIMS results indicate low concentrations of oxygen and nickel compared to B. Compositional analysis of the $B_{12}As_2$ crystals by EDS demonstrated 86at% B and 14at% As; i.e. the stoichiometric composition for $B_{12}As_2$. The SIMS

and EDS results offer only a qualitative analysis of the composition because there was no standard to measure the results against.

Table 4-2 - Icosahedral boron arsenide crystal size as a function of cooling rate and high temperature dwell time.

Cooling Rate (°C/hr)	Time at 1150°C (hr)		
	24	**48**	**72**
100	1mm	1mm	1mm
10	1mm	1-2mm	2-3mm
5	1mm	5mm	5mm
3.5	1mm	8-10mm	11-15mm

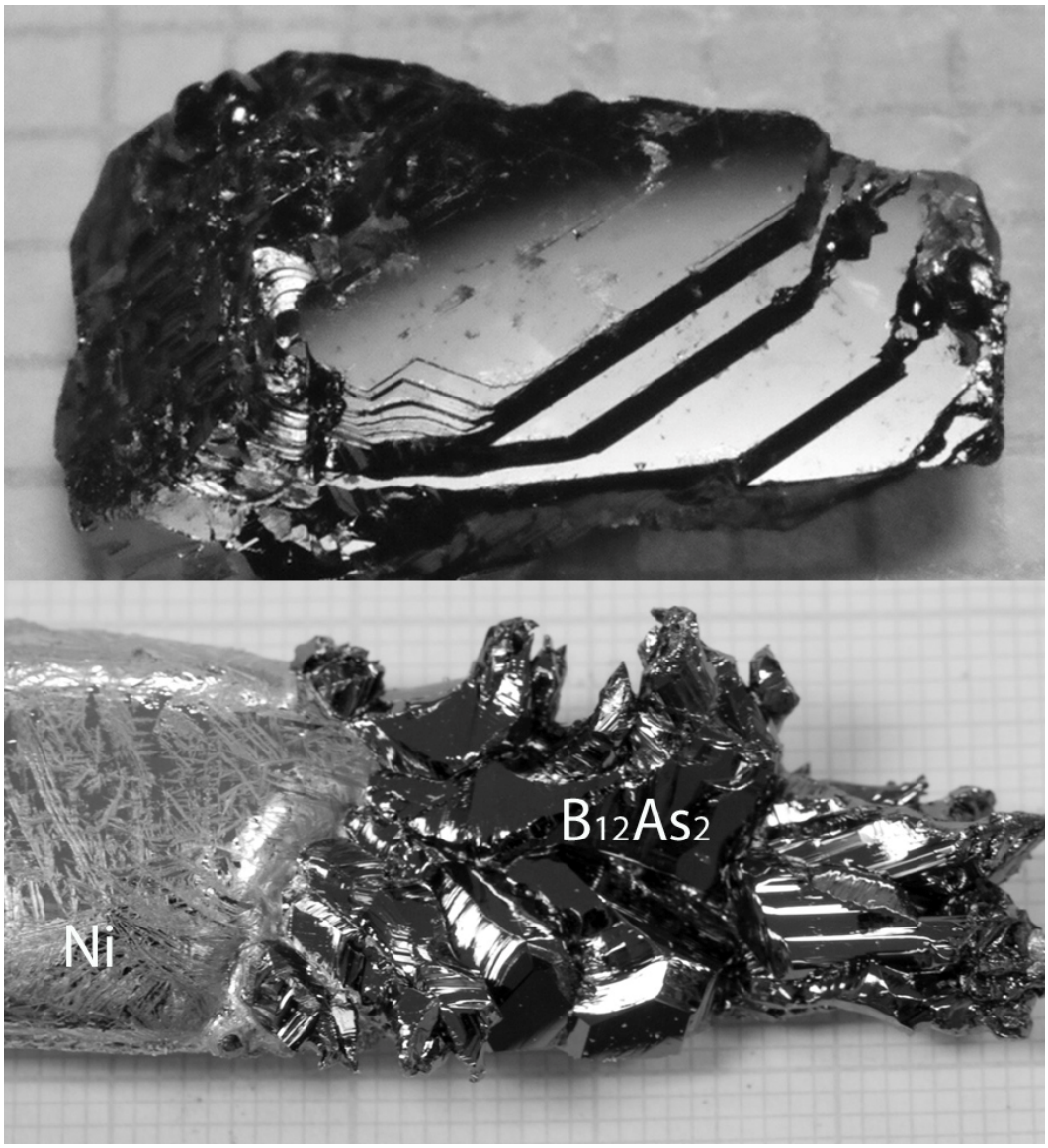

Figure 4-3 - Image of a $B_{12}As_2$ crystal in reflection, 7mm in longest dimension, depicting platelet shaped crystals (Top). Image of $B_{12}As_2$ crystals growing with many facets on the arsenic end of the ingot (bottom).

The Raman results are shown in Figure 4-4. The spectrum has sharp peaks at 307, 505, 622, 679, 737, and 791 ± cm^{-1}. The listed peaks are all characteristic of $B_{12}As_2$ crystals, and the lack of any other peaks indicates low impurity concentrations [31]. Narrow linewidths (2 and 8 cm^{-1}) indicate a highly ordered chain structure, and excellent crystal quality. The compositional analysis as well as the results from the Raman spectrum confirm that $B_{12}As_2$ crystal was grown and not other compounds such as BAs, or some combination of the two.

Further, the quality of the crystals was confirmed with defect selective etching, as seen in Figure 4-5. The number of etch-pits only increased slightly ($5x10^7$ pits/cm^2) after two minutes of etching at 550 °C indicating a low defect density. In general, the observed etch pits correspond to dislocations (screw, edge, or mixed). The etch pits still need to be analyzed to show that they form at defects. However, for many different materials (AlN, SiC, GaN) etch pits were associated with dislocations using transmission electron microscopy (TEM) [33,34]. Correlating the etch pits with dislocations, or other defects, specifically for $B_{12}As_2$ will be the subject of a future study.

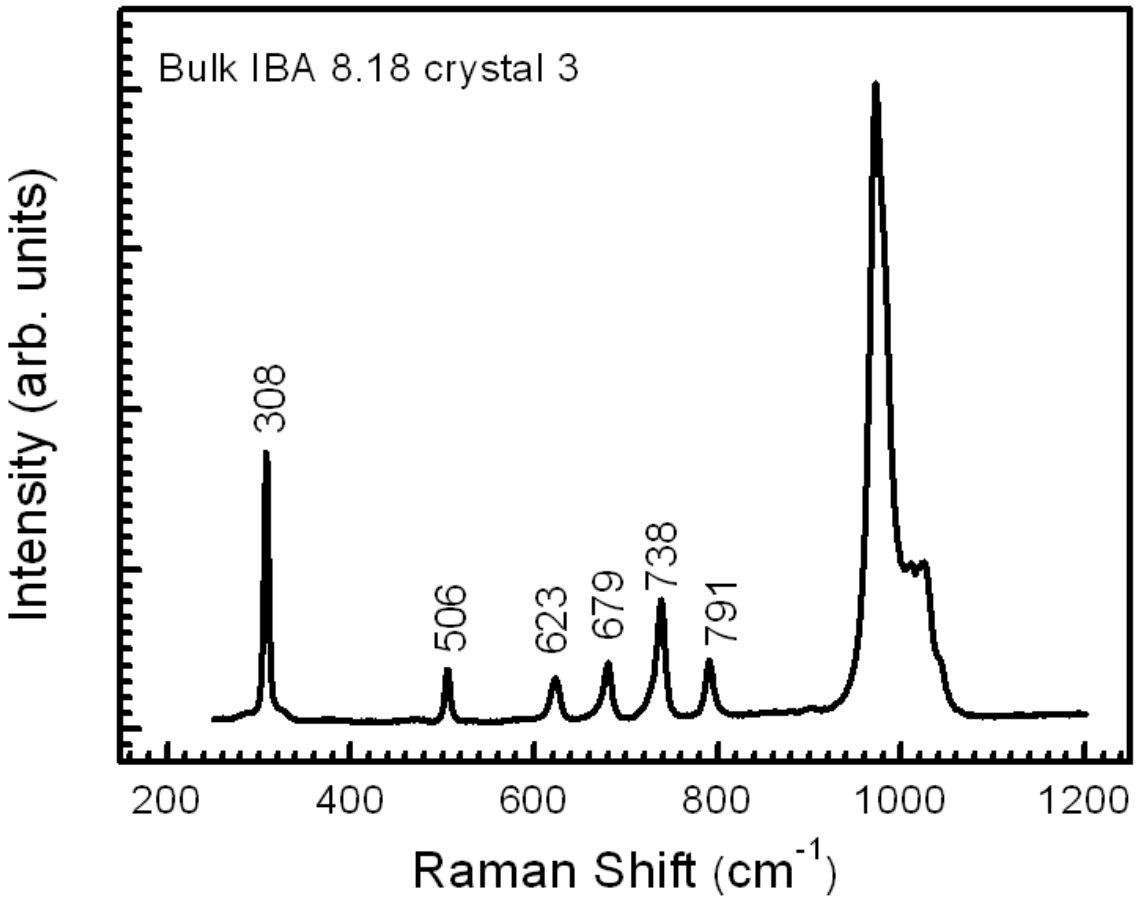

Figure 4-4 - Raman energy spectrum for flux grown boron arsenide crystals.

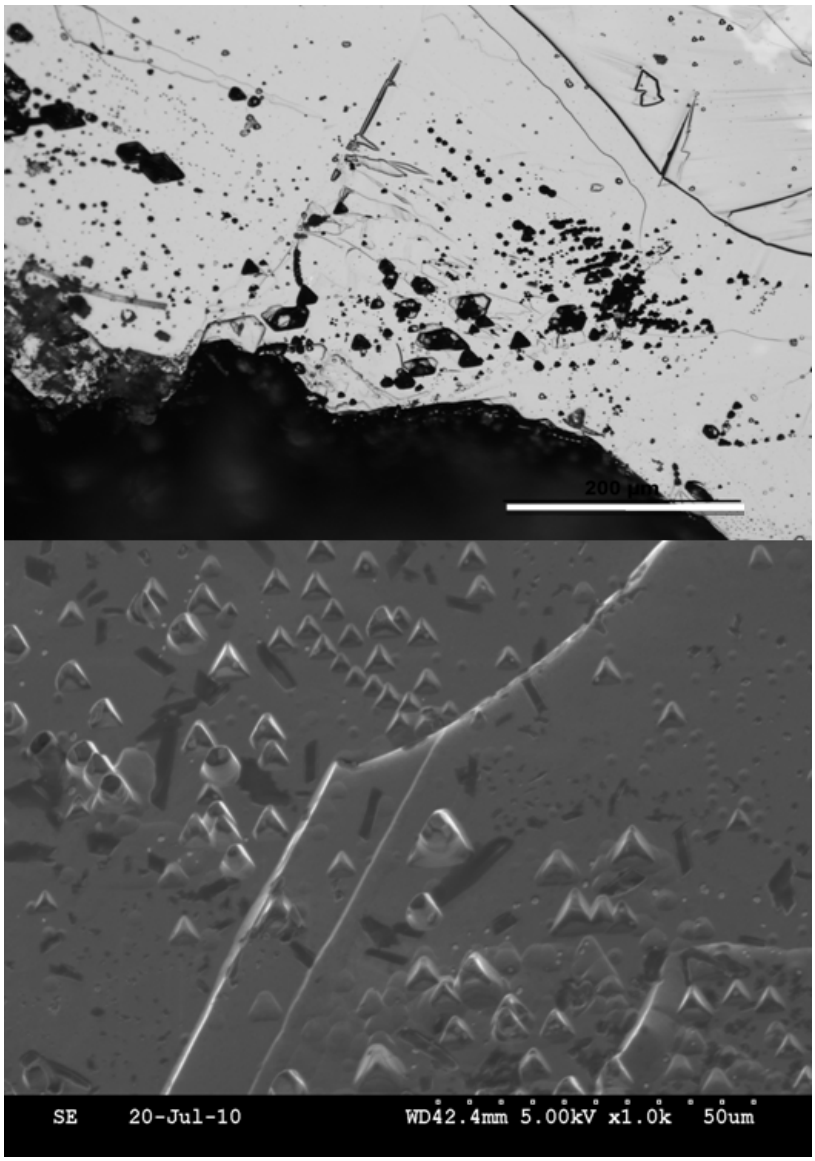

Figure 4-5 - Image of $B_{12}As_2$ crystals after defect selective etching for 5 minutes at 500°C. The etch-pit density was $4.4x10^7$pits/cm^2. The scale on the images is 200µm (Top). SEM image of the typical triangular etch pits (Bottom).

Conclusions

The hole mobility, radiation hardness, and wide band gap of the icosahedral boron arsenide crystals are all properties that favor the fabrication of detector devices, and knowledge of the crystal growth mechanism is the first step in determining the fundamental properties. A detailed exploration of the growth parameters of boron arsenide revealed that large (15 mm) $B_{12}As_2$ crystals can be grown via a flux growth mechanism with nickel as the solvent. Using elemental

boron (instead of $B_{12}As_2$ powder) as the source material is a superior method for producing large crystals; 15 mm compared to 1 mm. The crystals formed in the flux and, due to a very low solubility of the crystals in the solution, precipitated out of the solution when the temperature was slowly decreased (3.5 °C/ h); indicating that the cooling rate is a significant factor in the growth mechanism. Characterization of the $B_{12}As_2$ crystals demonstrates that high quality semiconductors can be produced at a relatively low temperature, much lower than the melting points of the source materials.

References

[1] N. Tsolfanidis, Measurement and Detection of Radiation, second ed., Taylor & Francis, Bristol, (1995).

[2] W. Orellana, H. Chacham, Phys. Rev. B **63** 125205 (2001).

[3] Y. Kumashiro, J. Mater. Res. **5** 2933 (1990).

[4] T.L. Chu, A.E. Hyslop, J. Electrochem. Soc. **121** 412 (1974).

[5] G.A. Slack, T.F. McNelly, E.A. Taft, , J. Phys. Chem. Solids **44** 1009 (1983).

[6] F. The´venot, J. Eur. Ceram. Soc. **6** 205 (1990).

[7] D. Emin, J. Solid State Chem. **179** 2791 (2006).

[8] M.Carrard,D.Emin,L.Zuppiroli, Phys. Rev. B **51** 270 (1995).

[9] S. Bakalova, Y. Gong, C. Cobet, N. Esser, Y. Zhang, J.H. Edgar, Y. Zhang, M. Dudley, M. Kuball, Phys. Rev. B **81** 075114 (2010).

[10] J.R. Michael, T.L. Aselage, D. Emin, P.G. Kotula, J. Mater. Res. **20** 3004 (2005).

[11] F.H. Horn, J. Electrochem. Soc. **106** 905 (1959).

[12] R.A. Burmeister Jr., P.E. Greene, Trans. Metall. Soc. AIME **239** 408 (1967).

[13] Y. Kumashiro, T. Yao, S. Gonda, J. Cryst. Growth **70** 515 (1984).

[14] T.L. Aselage, Mater. Res. Soc. Symp. Proc. **97** 101 (1987).

[15] T.L. Aselage, S.B. Van Deusen, B. Morosin, J. Less-Common Met. **166** 29 (1990).

[16] P. Yang, T.L. Aselage, in: Proc. 11th Int. Symp. Boron, Borides and related compounds, JJAP Series **10**, 130 (1994).

[17] M.Yamamoto,Y.Hamazaki,M.Tsukihara,Y.Naoi,K.Nishino,S.Sakai , Jpn. J. Appl. Phys. **46** 323 (2007).

[18] O.A.Golikova, Phys. Status Solidi A **51** 11 (1979).

[19] T.L. Aselage, D. Emin, G.A. Samara, D.R. Tallant, S.B. Van Deusen, M.O. Eatough, H.L. Tardy, E.L. Venturini, S.M. Johnson, Phys. Rev. B **48** 11759 (1993).

[20] Z.Xu, J.H.Edgar, D.C.Look, S.Baumann, R.J.Bleiler, S.H.Wang, S.E.Mohney, J. Appl. Phys. **101** 053710 (2007).

[21] H. Werheit, U. Kuhlmann, J. Solid State Chem. **133** 140 (1997).

[22] L. Vel, G. Demazeau, J. Etourneau, Mater. Sci. Eng. B **10** 149 (1991).

[23] Y. Kubota, K. Watanabe, T. Taniguchi, Jpn. J. Appl. Phys. **46** 311 (2007).

[24] J.D.Buckley, J.A.Cooley, Mater. Sci. Res. **5** 547 (1971).

[25] B. Pamplin, Crystal Growth, second ed., Pergamon Press, New York, (1980).

[26] R.H. Deitch, Int. Ser. Monogr. Sci. Solid State **6** 427–496 (1975).

[27] P.D. Peshev, Bulg. Chem. Commun. **24** 235–243 (1992).

[28] D. Elwell, H.J. Scheel, Crystal Growth from High-Temperature Solutions, Academic Press, London, (1975).

[29] K.E.Spear, in: Proceedings of Applications of Phase Diagrams in Metallurgy and Ceramics, NBS special Publication **496** 744–762 (1978).

[30] B. Wodniecka, P. Wodnieckit, K. Krolas, L. Thome, J. Phys. F: Met. Phys. **16** 1629–1637 (1986).

[31] J.W. Pomeroya, M. Kuball, J. Appl. Phys. **96** 910–912 (2004).

[32] G. Rosenblatt, P. Lee, J. Chem. Phys **49** 2995–3006 (1968).

[33] M. Bickermann, S. Schmidt, B.M. Epelbaum, P. Heimann, S. Nagata, A. Winnacker, Phys. Status Solidi **4** 2609–2612 (2007).

[34] D. Zhuang, J.H. Edgar, Mater. Sci. Eng. R **48** 1–46 (2005).

CHAPTER 5 - DEFECT SELECTIVE ETCHING

Abstract

The present work reports on the defect-selective etching (DSE) for estimating dislocation densities in icosahedral boron arsenide ($B_{12}As_2$) crystals using molten potassium hydroxide (KOH). DSE takes advantage of the greater reactivity of high-energy sites surrounding a dislocation, compared to the surrounding dislocation-free regions. The etch pits per area are indicative of the defect densities in the crystals, as confirmed by x-ray topography (XRT). Etch pit densities were determined for icosahedral boron arsenide crystals produced from a molten nickel flux as a function of etch time (1-5 minutes) and temperature (400-700°C). The etch pits were predominately triangle shaped, and ranged in size from 5-25μm. The average etch pit density of the triangle and oval etch-pits was on the order of $5x10^7cm^{-2}$ and $3x10^6cm^{-2}$ (respectively), for crystals that were etched for two minutes at 550°C.[1]

[1] Published in the Proc. of the Mat. Res. Soc. Meet. (2010), by C.E. Whiteley, A. Mayo, J.H. Edgar, M. Dudley, and Y. Zhang.

Introduction

The high neutron absorption capture cross-section (~3800 Barns) of ^{10}B allows for even thin layers of compounds rich in ^{10}B to absorb all incident thermal neutrons (100% efficiency). If the radiation interaction occurs in a semiconductor, for each neutron captured, ~1.5 x 10^6 electron-hole pairs are produced as the energetic ^7Li and ^4He ions pass through the material [1,2]. This ionization generates a current that can be detected directly without further amplification. Thus, a boron-rich semiconductor radiation detector could be based on a Schottky, pn, or pin diode.

There are two rhombohedral boron-rich III-V wide bandgap semiconductors: $B_{12}As_2$ (3.24 eV) and $B_{12}P_2$ (3.35 eV) [3]. The structure of the two borides consists of 12-boron-atom icosahedra located at the corners of a rhombohedral (trigonal) unit cell and a two-atom As-As or P-P chain spanning the unit cell body diagonal aligned with the c-axis, as seen in Figure 1-1 [3]. For the boride semiconductors to work well as radiation detectors, the crystals must be excellent quality and have favorable electrical properties, i.e. a large mobility and charge carrier lifetime (a large $\mu\tau$ product, ~10^{-3} cm^2/V) [1,2].

The electrical properties of a semiconductor are heavily influenced by the density of defects (imperfections in the crystal lattice structure) on the surface and within the material. The study of such imperfections or defects is important for understanding the influence of imperfections on crystal-growth processes, and conversely, such feedback can be used to optimize the process to produce higher quality crystals [4]. Hence, it is essential for process engineers and crystal growers to characterize and identify the density, distribution, and nature of defects present in crystals.

Defect-selective etching is a technique developed to take advantage of the high-energy sites on the surface of crystals. The etchant oxidizes and dissolves material at the defect site, producing an etch pit on the surface [5]. The most effective etchants are molten salts, namely potassium hydroxide (KOH) [5]. A general rule for all wet etching processes is that diffusion-limited etching results in a smooth and pit-free surface, while reaction-limited etching produces a rough surface and delineates etch pits under certain conditions [5]. After etching, small, usually geometrically shaped pits, will form on the crystal surface over a defect. In general, the etch pits correspond to dislocations (screw, edge, or mixed).

Previous characterization of defects in boron rich compounds, $B_{12}As_2$ thin films and boron carbide, revealed double positioning twins and dislocations (edge and screw) [4,8,9]. For many other materials (AlN, SiC, GaN, boron carbide) the association of etch pits with dislocations was confirmed by transmission electron microscopy (TEM) and x-ray topography (XRT) [9-18]. Determining whether trends exist in etch-pit shape and density as a function of facet orientation would be a significant step towards growing high quality ($<10^8$ cm^{-2}) and low impurity ($<10^{19}$ cm^{-3}) homoepitaxal layers of $B_{12}As_2$. Thus, the optimum etching conditions for DSE were determined, and the results were compared to known x-ray topography data.

Experimental Procedure

$B_{12}As_2$ crystals were grown by precipitation from molten nickel solutions saturated with elemental boron and arsenic in a sealed quartz ampoule at 1150°C [19]. The $B_{12}As_2$ single crystals selected for the study were typically about 5 x 4 x 2 mm^3 in size and had well-developed facets with mirror-like surfaces. Crystallographic indexing of the facets was determined based on the natural growth habit using XRT.

To determine the optimal etching conditions, $B_{12}As_2$ crystals (with single facets) were placed in molten KOH at temperatures between 400-700°C (±10°C), for times ranging from 1-5 minutes (±15sec). The etching apparatus consisted of a resistance heated crucible furnace with a 10 Amp external temperature controller. A vitreous carbon crucible was placed a few inches from the top of the furnace on a ceramic holder. The top of the furnace was covered with alumina insulation to stabilized the KOH melt temperature. The thermocouple probe and power-control sensor rested vertically in the ceramic holder inside the furnace, directly next to the reaction crucible.

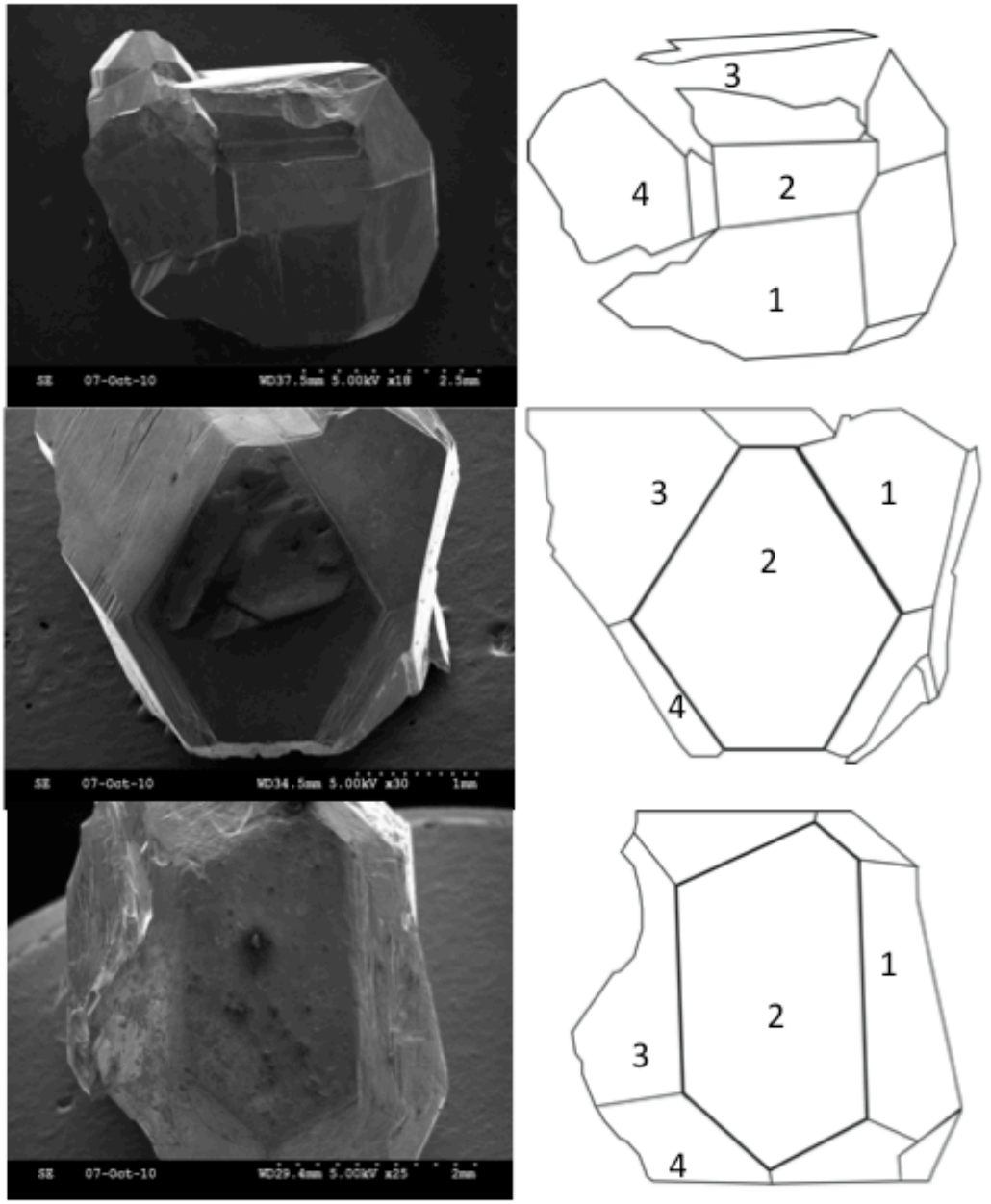

Figure 5-1 - SEM images of the three multi-faceted crystals with illustrations of the crystals and the label given to each facet.

The optimum etching conditions and the reaction mechanism were determined from variable time (1, 2 and 5 minutes) and temperature (ranging from 400 to 700 C) experiments. These determined: (1) the temperature dependence, (2) the time dependence, and (3) time and temperature independence. First, three samples were etched for 1, 2, or 5 minutes, respectively, in order to observe the affect of increasing temperature from 400-700°C in 50°C increments. Next, five new samples were etched at the incremental temperatures (one for each temperature),

and three different times; the effect of increasing time was observed. Then, fifteen more $B_{12}As_2$ crystals were etched once each at a particular temperature and time (400-700°C in 50°C increments and 1, 2, or 5 minutes) in order to compare with the first two trials and observe the affects of accumulating time and temperature, and the optimum etching conditions were established.

Next, to study the etching behavior of different facets of the $B_{12}As_2$ crystals, three different crystals (with multiple facets each) were photographed (as seen in Figure 5-2) and etched at the optimal etching conditions. Finally, all samples (single and multi faceted) were photographed with an optical microscope and an SEM, and the areal etch pit density (EPD) was measured.

Results and Discussion

Table 5-1 -Results of the DSE optimization experiments revealing the optimum etching conditions (550 C for 2 min) for $B_{12}As_2$ crystals. The "0" indicates no etch pits or etch pits that were <5 µm in diameter. The "∞" means the entire surface etched or no change in EPD from the previous trial.

		Temperature (^oC)						
Time (min)		**400**	**450**	**500**	**550**	**600**	**650**	**700**
1	Exp 1	0	0	0	0	∞	∞	∞
	Exp 2	0	0	0	**10^7**	∞	∞	∞
	Exp 3	0	0	0	0	∞	∞	∞
2	Exp 1	0	0	0	**10^7**	∞	∞	∞
	Exp 2	0	0	0	**10^7**	∞	∞	∞
	Exp 3	0	0	0	**10^7**	∞	∞	∞
5	Exp 1	0	0	**10^7**	∞	∞	∞	∞
	Exp 2	0	0	∞	∞	∞	∞	∞
	Exp 3	0	0	**10^7**	∞	∞	∞	∞

In the temperature dependent experiment, some samples were etched at multiple temperatures; in a few cases the surface became too rough to distinguish individual etch-pits. Etching selectivity may be lost when general etching of the dislocation-free material occurs, resulting in the entire surface etching. The time dependent experiment revealed that etching the

samples at a constant temperature with increasing time produced no more etch pits; however the etch-pits did increase in size. No additional etching was expected because the first experiment tentatively established reaction-limited kinetics. Making time and temperature independent confirmed the observations from the first two trials; reaction-limited kinetics [5,9-18]. Combining the results from the 3 experiments, the optimum etching temperature and time was narrowed to 550°C for 2 minutes.

To explain this behavior, the facets of the multi-faceted crystals were labeled, as seen in Figure 5-1. While etching the multi-faceted $B_{12}As_2$ crystals, three of the four facets etched, as shown in Table 5-2, suggesting that crystal facet orientations have specific etch conditions. Side one did not appear to etch at all, even upon closer inspection with SEM. Side two and three etched similarly to the $B_{12}As_2$ samples in experiments 1-3. Where triangle shaped etch-pits of two distinct sizes developed, some formed along lines, suggesting a dislocation or grain boundary, as seen in Figure 5-2 and 5-3.

Side four of the multi-faceted crystals was the only orientation that produced irregular shaped (oval) etch pits all oriented in the same direction, as seen in Figure 5-3. The average EPD of the triangle and oval etch-pits was on the order of $5x10^7$ cm^{-2} and $3x10^6$ cm^{-2} (respectively), based on the change in pits between pre and post-etching.

XRT was used to determine that the predominate growth facet was (111), which was subsequently etched and depicted only triangle-shaped etch pits. This result shows that all of the single facet crystals were the (111) orientation. However, the oval shapes that appeared on side four still need to be examined for facet orientation.

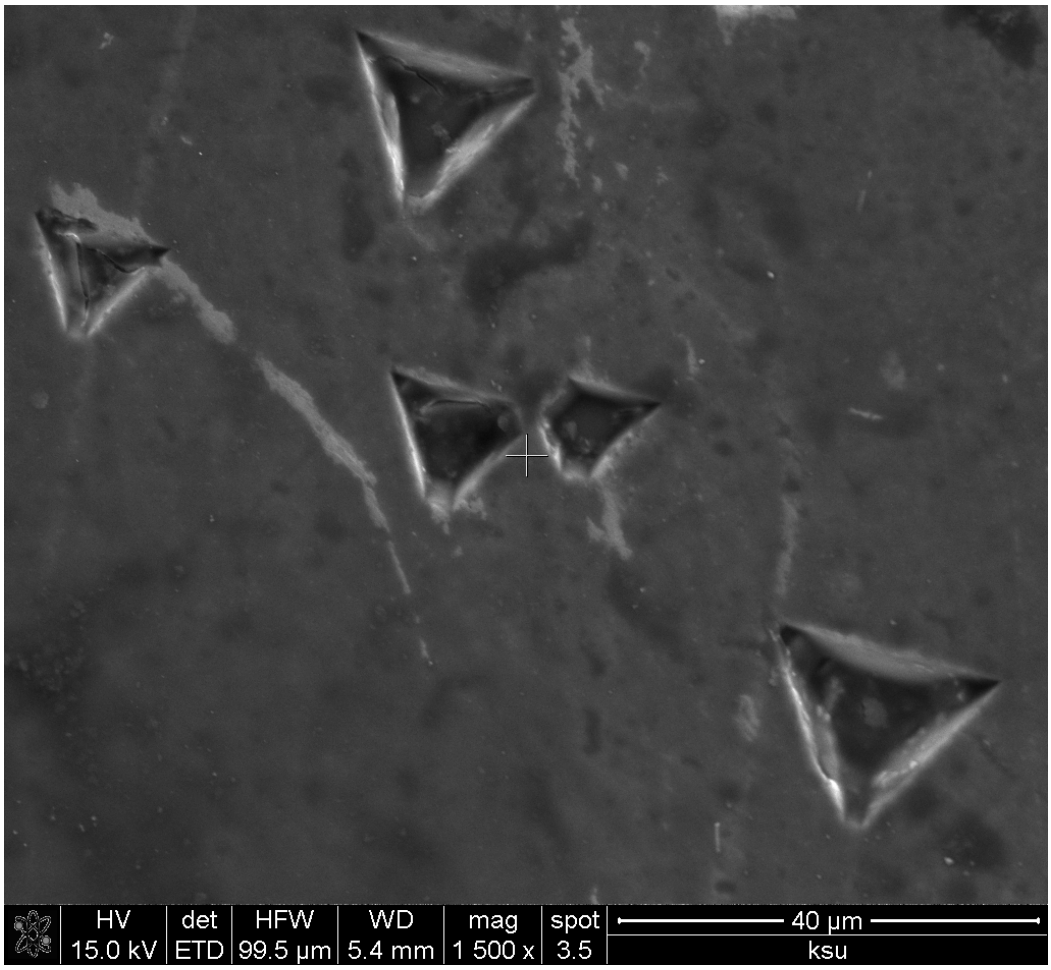

Figure 5-2 - SEM image of typical triangle etch pits.

Table 5-2 - Tabulated results from etching the multi-faceted crystals. There was etching on 3 of the 4 studied sides. General observations about the pre-etch structures, the shape and pattern of the etch pits, and additional notes were recorded.

Crystal Facet	Etch pit shape(s)	Etch pit pattern(s)	Notes
Side 1	None	None	None
Side 2	Triangles, Figure 5-2	Lines	Results are similar to those on the (111)
Side 3	Triangles, Figure 5-4	Lines/clusters; consistent orientation	Triangular pits different than side 2
Side 4	Ovals and triangles, Figure 5-3	Random; lines; consistent orientation (ovals)	Ovals are depressions in surface

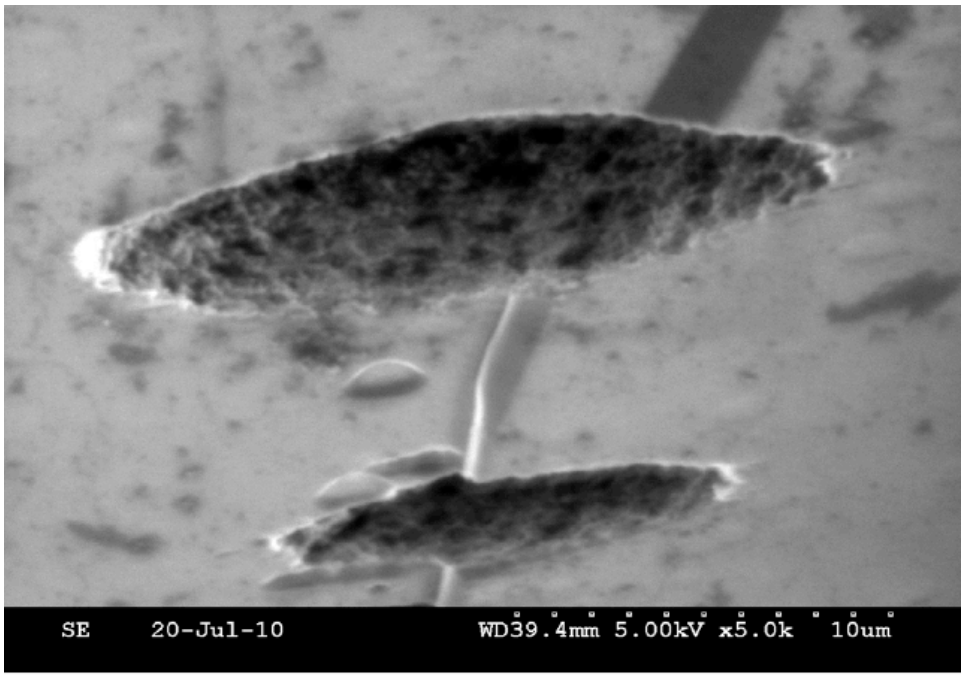

Figure 5-3 – SEM image of ovals that formed on side four of the multi-faceted crystals.

Based on previous work with defect-selective etching on other materials and the XRT results, the $B_{12}As_2$ etch pits correspond to edge dislocations [5,9-18]. The unique shapes, observed while etching the multi-faceted crystals, are indicative of the specific orientation of the crystals, as confirmed by XRT. An EPD of $5x10^7$ cm^{-2} is a low value (10^8 cm^{-2} was expected), compared to previous work [5,9-18], indicating excellent crystal quality. The crystal quality was also confirmed with Raman spectroscopy; where the characteristic peaks and narrow line widths reveal exceptional crystal quality [19].

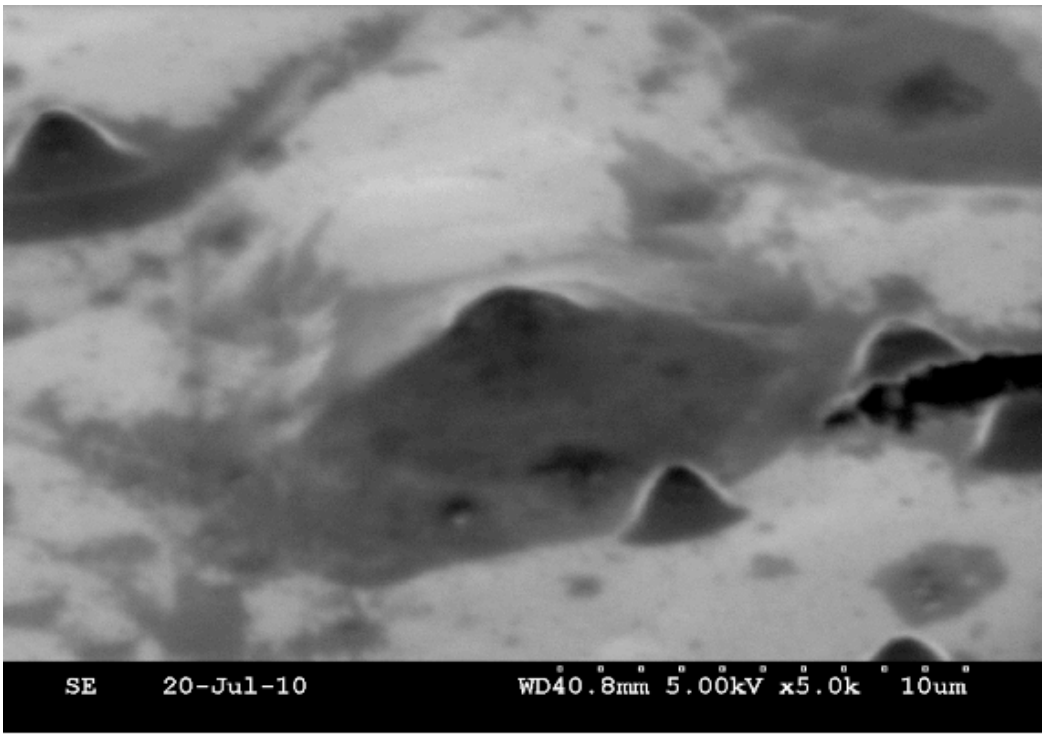

Figure 5-4 - Triangle shaped etch-pit that is a different size than the pits observed on side 2 of the multi-faceted crystals.

Conclusions

Defect selective etching of $B_{12}As_2$ crystals under reaction limited kinetics was demonstrated, and indicated a low density of etch pits ($5x10^7$ cm^{-2}) after etching at 550°C for 2 minutes; indicating excellent crystal quality. Additionally, etching multi-faceted crystals revealed that the facets have orientation specific defects, which require further investigation. By studying the etching behavior of unique crystal facets, a correlation was drawn that relates the etch pit shapes to particular defects (edge dislocations) and crystal orientation (the (111) facet orientation produced only triangle etch-pits). From these results, defect-selective etching was shown to be an effective method for determining the extent of defects on the surface of $B_{12}As_2$ crystals, and therefore an excellent way to judge the quality of the crystals.

References

[1] N. Tsolfanidis, Measurement and Detection of Radiation, 2nd Ed.; Taylor & Francis: Bristol, (1995)

[2] L. Gerhard, Semiconductor Radiation Detectors, 1st Ed.; Springer: New York, (2007)

[3] Z. Xu, J. H. Edgar, S. Speakman, J. Cryst. Growth **293** 162-168 (2006).

[4] K.H.G. Ashbee, and C.K.H. Dubose, Acta Meta. **90** 241-245 (1972)

[5] D. Zhuang, J.H. Edgar, Mater. Sci. Eng. Rev., **48** 1-46 (2005)

[6] W. Callister, and D. Rethwisch, Fundamentals of Materials Science and Engineering: an Integrated Approach. John Wiley and Sons, (2007)

[7] A. Bennet, Crystals Perfect and Imperfect. Walker and Company, (1965).

[8] H. Chen, Defect Structures and Growth Mechanisms of $B_{12}As_2$ Epilayers Grown on 6H-SiC and 15R-Sic Substrates, Dissertation, Stony Brock University (2008)

[9] D. Zhuang, Wet etching studies of aluminum nitride bulk crystals and their sublimation growth by microwaves, Dissertation, Kansas State University, 2004

[10] J.L. Weyher, M. Albrecht, T. Wosinski, G. Nowak, H.P. Strunk, S. Porowski, Mat. Sci. and Eng. **B80** 318-321 (2001)

[11] J.L. Weyher, L. Macht, G. Kamler, J. Borysiuk, and I. Grzegory, Phys. Stat. Sol. C 821-826 (2003)

[12] D. Zhuang, J.H. Edgar, B. Strojek, J. Chaudhuri, and Z. Rek, J. Cryst. Growth. **262** 89-94 (2004)

[13] J.L. Weyher, S. Lazar, J. Borysiuk, and J. Pernot, Phys. Stat. Sol., 578-583 (2005)

[14] Z. Gu, J.H. Edgar, D.W. Coffey, J. Chaudhuri, L. Nyakiti, R.G. Lee, and J.G. Wen, J. Cryst. Growth, **293** 242-246 (2006)

[15] M. Bickermann, S. Schmidt, B.M. Epelbaum, P. Heimann, S. Nagata, and A. Winnacker, J. Cryst. Growth **300** 299-307 (2007).

[16] M. Albrecht, J.L. Weyher, B. Lucznik, I. Grzegory, and S. Porowski, Appl. Phys. Lett., **92** 231909 (2008)

[17] L. O. Nyakiti, J. Chaudhuri, E. A. Kenik, P. Lu, J. H. Edgar, and P. Li, Mater. Res. Soc. Symp. Proc., **1040** 1069-D08-03 (2008)

[18] Y. Zhang, J.H. Edgar, J. Plummer, C.E. Whiteley, H. Chen, Y. Zhang, M. Dudley, Y. Gong, J. Gray, and M. Kuball, Materials Research Society Symposium Proceedings, **1164** (2009)
[19] C.E. Whiteley, A. Mayo, J.H. Edgar, M. Kuball, and Y. Zhang, J. Cryst. Growth **318** 553-557 (2011).

CHAPTER 6 - CRYSTAL FACET ORIENTATION

Abstract

The crystallographic properties of bulk icosahedral boron arsenide ($B_{12}As_2$) crystals grown by precipitation from molten nickel solutions were characterized. Large crystals (5-8 mm) were produced by first dissolving the boron in nickel at 1150°C for 48-72 hours, then reacting with arsenic vapor, followed by slow cooling to room temperature. The crystals varied in color from black and opaque to clear and transparent. Raman spectroscopy, x-ray topography (XRT), and defect selective etching revealed that the flux method produced high structural quality $B_{12}As_2$ single crystals with low dislocation densities. Furthermore, XRT results suggest that the major face of the plate-like crystals was (111) type, while (100), (010) and (001) type facets were also observed optically. The predominant defect in these crystals was edge character growth dislocations with a <001> Burgers vector, and <-110> line direction. In short, XRT characterization shows that solution growth is a viable method for producing good quality $B_{12}As_2$ crystals.[1]

[1] Published in the Proc. of the Mat. Res. Soc. Meet. (2010), by C.E. Whiteley, Y. Zhang, A. Mayo, J.H. Edgar, Y. Gong, M. Kuball, and M. Dudley.

Introduction

Due to the unique chemical, physical, and electrical properties, the semiconductor icosahedral boride $B_{12}As_2$ is a potential candidate for radiation detection devices. Combining the large capture cross-section for thermal neutrons (~3800 barns) of the ^{10}B isotope with semiconducting properties makes producing efficient, compact, and robust neutron detectors possible. In addition, the relatively high hole mobility and the ability to self-heal from radiation damage are additional properties that make this semiconductor worthy of study [1,8].

$B_{12}As_2$ was deposited on several foreign substrates including silicon and silicon carbide (4H-SiC, 6H-SiC, 15R-SiC), but the mismatch of structural parameters creates stresses, crystalline defects and contamination from the substrate in the thin film, all of which degrade the properties of the film [9-14]. With that said, microstructure of $B_{12}As_2$ epitaxial layers grown on m-plane 6H-SiC, 15R-SiC substrates have been studied with the aid of synchrotron white-beam x-ray topography (SWBXT). High temperatures (>1300 °C) are generally necessary to produce good quality $B_{12}As_2$ by CVD, but at this temperature silicon substrates react with $B_{12}As_2$ films [2,12]. Similarly, $B_{12}As_2$ can react with SiC to form a boron carbide transition layer between the film and substrate at high temperatures [10-14]. Figure 6-1 depicts some common facet orientations of the $B_{12}As_2$ crystals.

Previous SWBXT work on $B_{12}As_2$ thin films revealed multiple domains, including (1-21) $B_{12}As_2$, (2-12) $B_{12}As_2$, (353) $B_{12}As_2$ and their respective twins [10-14]. In $B_{12}As_2$ films grown on 3.5^o off-axis and on-axis (0001) 6H-SiC, Wang *et al* [11] observed polycrystalline grains with preferred orientation of [0001] $B_{12}As_2$ // [0001] 6H-SiC and [1010] $B_{12}As_2$ // [1010] 6H-SiC. Vetter *et al* [12] confirmed this orientation relationship for films grown on on-axis substrates although double positioning twins were also observed with one occurring more frequently than the other [12]. Michael *et al* [10] theoretically predicted the existence of a number of possible $B_{12}As_2$ structural variants based on the variety of non-equivalent nucleation sites available on the (0001) SiC surface; referred to as chemical, translational and rotational variants [14].

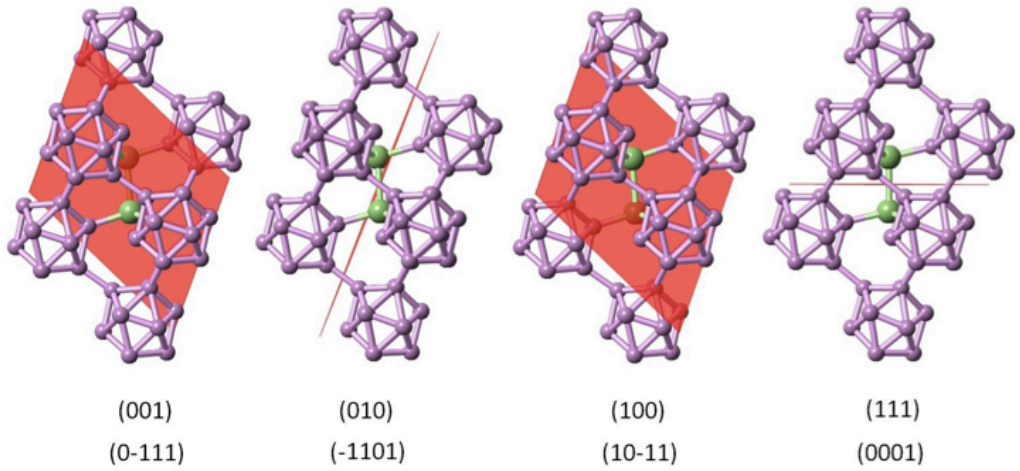

Figure 6-1 – Possible slip-planes in $B_{12}As_2$ crystals. The indicated plane is shown on each unit cell with a line or a square. Note that the four index hexagonal system is utilized. These planes can easily be related to the three-index rhombohedral system using the standard relationship such that [11-20] $B_{12}As_2$ is parallel to [10-1] $B_{12}As_2$, [9] [0001] $B_{12}As_2$ is parallel to [111] $B_{12}As_2$, and (0003) $B_{12}As_2$ is equivalent to (111) $B_{12}As_2$ [14].

With its high strain sensitivity, high intensity, suitable spatial resolution and broad spectral range, SWBXT is a powerful non-destructive tool to macroscopically investigate the crystallographic orientations and defect structures of crystals; it can document local changes in spacing and rotations of planes, and is not limited to external surface topography. For crystals with sufficiently low dislocation densities, standard Burgers vector analysis, which enables the determination of the direction of the Burgers vector, is readily carried out.

While there is extensive data in the literature regarding the analysis of $B_{12}As_2$ thin films with SWBXT [10-14], in contrast, there are no reports on the characterization of $B_{12}As_2$ bulk crystals with SWBXT. For any attempt at homoepitaxy with a $B_{12}As_2$ substrate to be effective, the preferred growth orientation, crystal quality, and predominate crystal defect of the bulk crystals must be determined. SWBXT is an excellent method for determining the orientation of crystal planes; which can be compared with Raman spectra and defect-selective etching (DSE) data to confirm the crystal quality. The present study reports on the preferred growth orientation and crystal quality of $B_{12}As_2$ bulk crystals.

Experimental Procedures

$B_{12}As_2$ crystals were grown by precipitation from molten nickel solutions saturated with elemental boron and arsenic in a sealed quartz ampoule at 1150°C [18]. The $B_{12}As_2$ single crystals selected for the study were typically about 5 x 4 x 1 mm^3 in size and had well-developed facets with mirror-like surfaces.

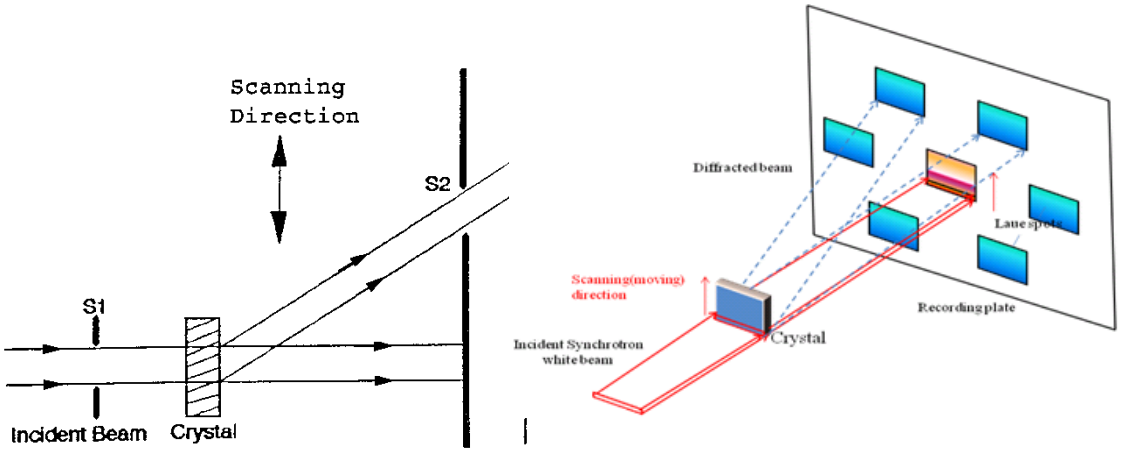

Figure 6-2 - Schematic of the scanning system at beamline X-19C at the NSLS. Both the crystal and film are scanned simultaneously through the incident beam enabling large-area coverage.

The diffraction images of the bulk crystal samples were recorded by transmission SWBXT. The SWBXT experimental procedure is similar to that done on heteroepitaxial $B_{12}As_2$ on SiC [10-14]. For epitaxial samples, the surface of the epilayer is the beam-exiting surface, so the most information from the epilayer can be gathered. However, for bulk samples there is no difference. The crystals were mounted perpendicular to the incident beam with a specimen-film distance as 11.5cm. Global views of the quality and structure of the crystals were initially obtained by recording transmission Laue patterns from the whole crystal volume. This was achieved by scanning the crystal and the film in the path of a slit-collimated beam as shown schematically in Figure 6-2, which enabled the distribution of defects and overall crystal quality to be determined.

SWBXT was performed at the Stony Brook synchrotron topography facility at the National Synchrotron Light Source (NSLS) in Brookhaven National Laboratory. The white beam x-ray had wavelength spectrum ranging from 0.01Å to 3.00Å, with the beam peak at a wavelength of

0.8 Å. Structural atomic-scale projection models were produced using the commercial software package CrystalMaker.

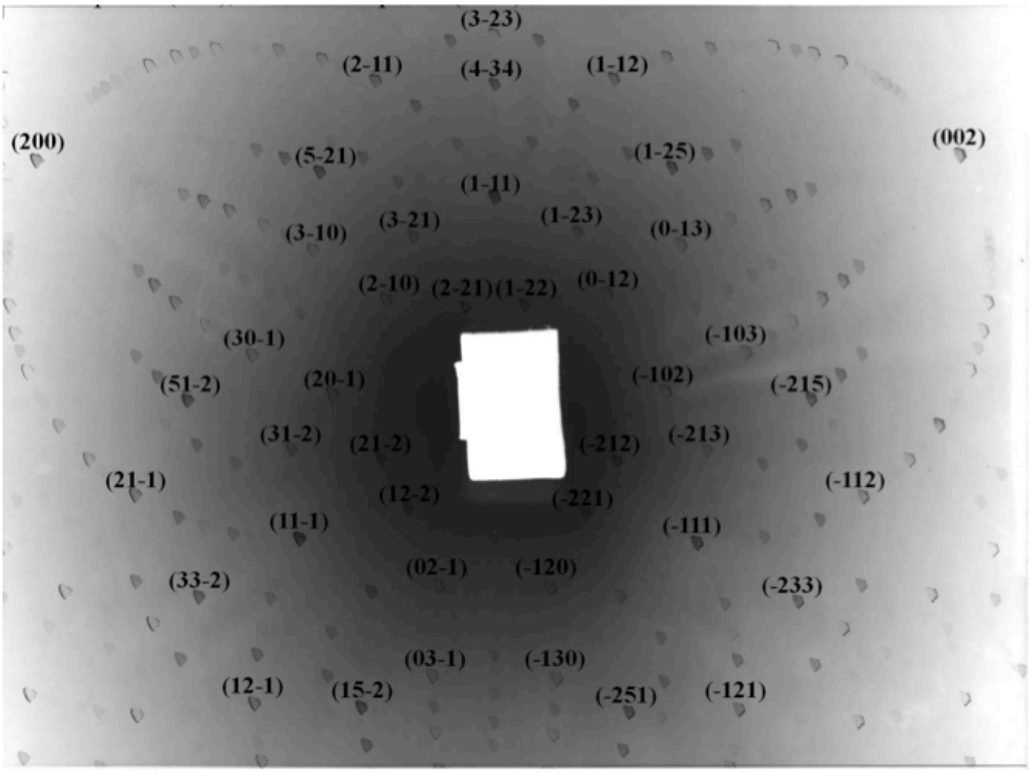

Figure 6-3 –SWBXT topograph of indexed $B_{12}As_2$ Laue pattern. The presence of distinct diffraction spots shows that the crystals are high quality single crystalline.

Results and Discussion

Figure 6-3 shows a transmission synchrotron white beam x-ray Laue pattern from the $B_{12}As_2$ bulk crystals produced in solution recorded with the crystals surface as the x-ray exit surface. In contrast to the thin-film grown on m-plane 6H-SiC and 15R-SiC [10-14], the $B_{12}As_2$ crystals grown in solution, produced much stronger and less streaked diffraction spots indicating improved mosaicity. The corresponding diffraction spots are marked with three indices shown as (hkl). The overall appearance of the $B_{12}As_2$ diffraction spots is consistent with a single crystalline and homogenous domain of (111) orientation, as seen in Figure 6-3 and 6-4. The Laue pattern of the bulk $B_{12}As_2$ crystals also lacked any evidence for the existence of twins,. In addition, the degree of asterism in the $B_{12}As_2$ spots is much lower than observed from the thin-films grown on m-plane 6H-SiC and 15R-SiC [10-14]. The dislocations were formed by deformation process during precipitation from the solution. Application of the $g \bullet b = 0$ criterion

showed the predominant defect in these crystals was edge character growth dislocations with < 001> Burgers vector, and <-110> line direction, as seen in Figure 6-5.

Raman spectra confirms the improvement with the Raman linewidths being narrower for the $B_{12}As_2$ bulk crystals, and in particular Raman intensity is stronger [18]. This illustrates that phonon properties and therefore also more macroscopic properties of the crystals are improved compared to epitaxial films. Only one type of equilateral triangular feature with a dimension of ~5-25μm and a density on the order of $5x10^7$ cm^{-2} was produced by DSE (Figure 6-6), which suggests the crystals are single crystalline and agree with the result from SWBXT.

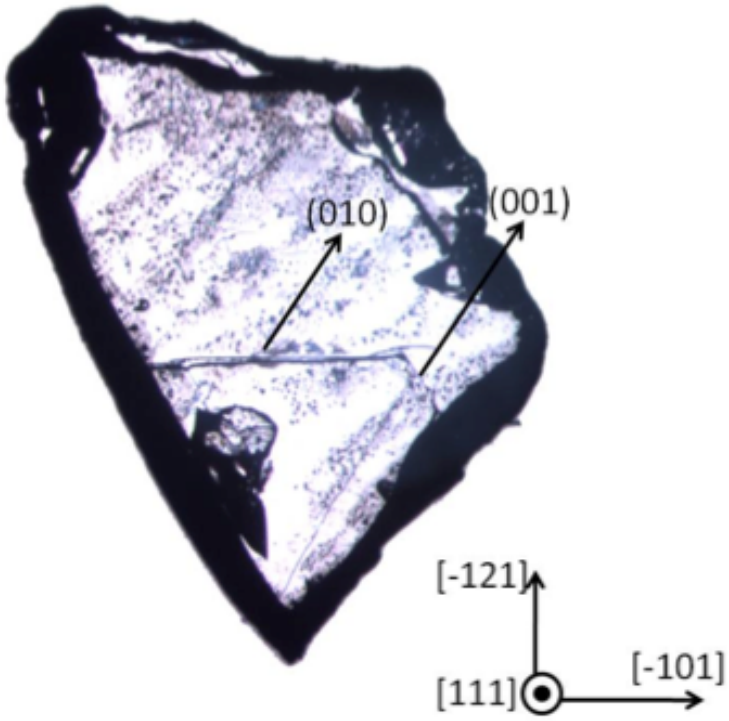

Figure 6-4 – Optical image of a $B_{12}As_2$ crystal depicting the preferred facet orientation.

For bulk crystals the SWBXT data show that the (111) facet is the slowest growing orientation, which indicates it as the most stable, or lowest energy, growth plane. $B_{12}As_2$ thin films readily adopt the (111) orientation when the substrate is also (111) [14]. Thus, the bulk $B_{12}As_2$ crystals are suitable as substrates for growing high quality thin films with low residual impurities.

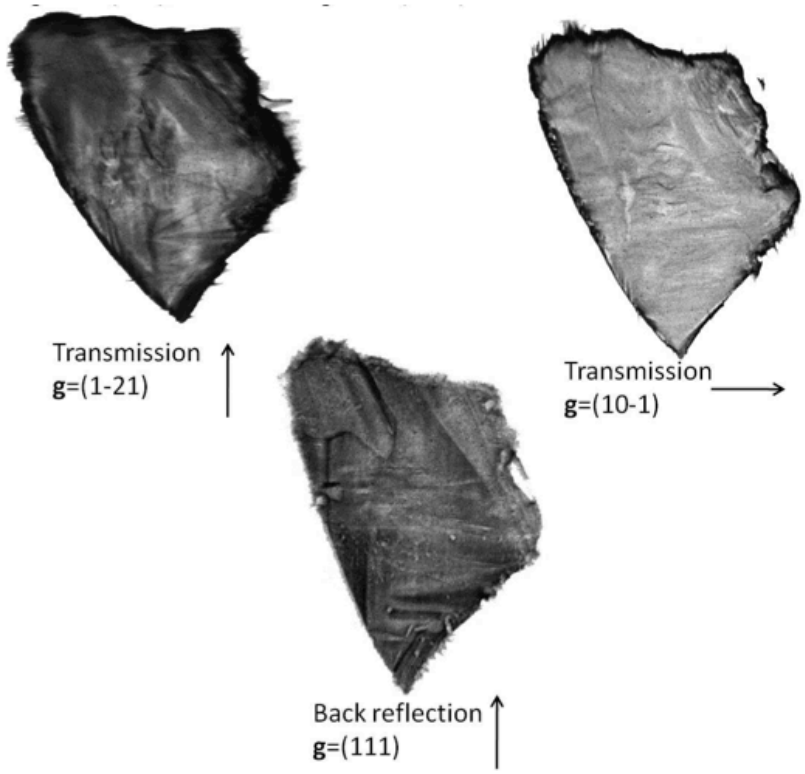

Figure 6-5 – Enlarged topographs with different g vectors of $B_{12}As_2$ crystal. Surface plane is (111) and vertical side plane is (-101).

Conclusions

The microstructure of $B_{12}As_2$ bulk crystals produced using the flux growth method was examined. XRT study suggests that the major face of the plate-like crystals was (111) type, while (100), (010) and (001) type facets were also observed optically. SWBXT revealed untwinned (111) orientated $B_{12}As_2$, with significantly improved macroscopic properties. The most prominent defects were typically edge-dislocations. In whole, SWBXT characterization shows that flux growth is a viable method for producing good quality $B_{12}As_2$ crystals, which have potential use as substrates for boron based devices.

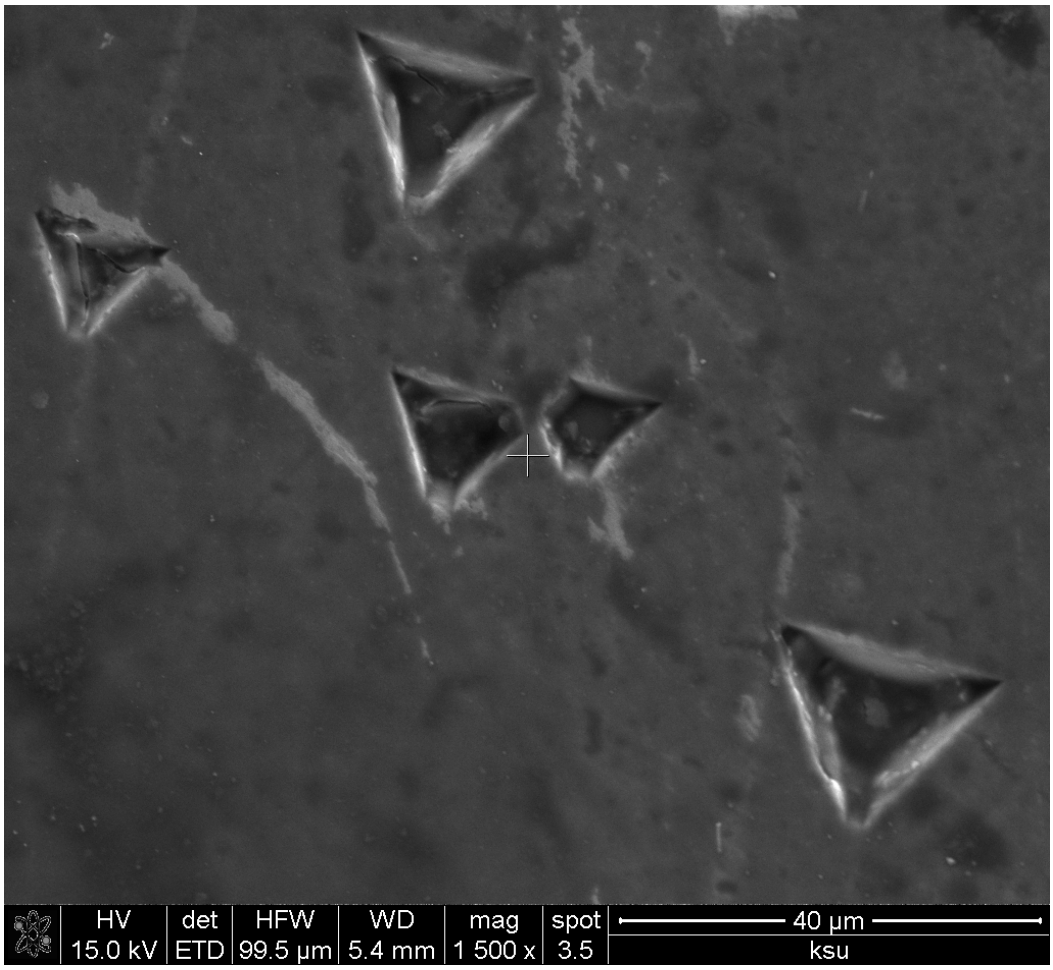

Figure 6-6 - SEM images of typical triangle shaped etch pits.

References

[1] D. Emin and T. L. Aselage, J. Appl. Phys. **97**, 013529 (2005)

[2]M. Dresselhaus, G. Chen, M. Y. Tang, R. Yang, H. Lee, D. Yang, Z. Ren, J. Fleurial, and P. Gogna, Int. Mater. Rev., **48**, 45 (2005)

[3] D. Emin, Physics Today, January, **55** (1987)

[4] G. A. Slack, D. W. Oliver and F. H. Horn, Phys. Rev. B, **4**, 1714, (1971)

[5] P. D. Ownby, Journal of the American Ceramic Society, **58**, 7-8, 359 (1975)

[6] D. Emin, J. Sol. Sta. Chem., **179**, 2791 (2006)

[7] D. Emin, J. Sol. Sta. Chem., **177**, 1619 (2004)

[8] M. Carrard, D. Emin and L. Zuppiroli, Phys. Rev. B, **51**, 11270 (1995)

[9] X. Zhou, J. H. Edgar and S. Speakman, J. Crystal Growth, **293**, 162 (2006)

[10] J. R. Michael, T. L. Aselage, D. Emin and P.G. Kotula, J. Mater. Res., **20**, 3004 (2005)

[11] R.H. Wang, D. Zubia, T. O' Neil, D. Emin, T. Aselage, W. Zhang and S.D. Hersee, J. Electronic Materials, **29**, 1304 (2000)

[12] W.M. Vetter, R. Nagarajan, J. H. Edgar and M. Dudley, Mater. Lett., **58**, 1331 (2004)

[13] R. Nagarajan, Z. Xu, J. H. Edgar, F. Baig, J. Chaudhuri, Z. Rek, E. A. Payzant, H. M. Meyer, J. Pomeroy and M. Kuball, J. Crystal Growth. **273**, 431 (2005)

[14] H. Chen, Defect Structures and Growth Mechanisms of $B_{12}As_2$ Epilayers Grown on 6H-SiC and 15R-Sic Substrates, Dissertation. Stony Brook University (2008)

[15] B. Raghothamachar, G. Dhanaraj, J. Bai, and M. Dudley, Micro. Res. Tech. 343-358 (2006)

[16] T. Shaffner, Proc. IEEE, Vol. **8**, (2000)

[17] T. Tuomi, J. Synchrotron Rad. 174-178 (2002)

[18] C.E. Whiteley, A. Mayo, J.H. Edgar, M. Kuball, and Y. Zhang J. Cryst. Growth **318** 553-557 (2011).

CHAPTER 7 - ELECTRICAL PROPERTIES AND DEVICE TESTING

Abstract

Icosahedral boron arsenide is a potential neutron detector and a beta voltaic battery because of its high thermal neutron capture cross-section and ability to resist radiation damage. Knowledge of both the μτ product and the majority carrier mobility is essential in determining the potential of a semiconductor for electronic devices. The impurity concentrations and defect densities are major factors that affect the electrical properties of all materials. Thus, obtaining knowledge of the impurities is essential in understanding how to improve the electrical properties of a material.

In this study, boron arsenide crystals were analyzed with secondary ion mass spectroscopy (SIMS) and x-ray photoelectron spectroscopy (XPS), and devices were fabricated for electrical property measurements. The impurity concentrations were shown to be high in both SIMS and XPS data: hydrogen (10^{20} cm^{-3}), carbon (10^{19} cm^{-3}), silicon (10^{17} cm^{-3}), and oxygen (3.9at%). The mobility and minority carrier concentration were calculated to be 24.5 cm^2/Vs and $7.28x10^{16}$ cm^{-3}. The μτ product measurement was unsuccessful, presumably due to the high impurity concentrations.

Introduction

$B_{12}As_2$ is a member of the icosahedral boride family, which are structures based on clusters of 12 boron atoms (located on the indices of a rhombohedral) and two-atom As-As chains (located along the body diagonal). It has a wide bandgap of 3.2eV [1,2] and high melting point of 2027°C [1,2]. The unique properties suggest $B_{12}As_2$ can be used as a high-temperature semiconductor, and in radiation detectors due to a self-healing mechanism [3-5]. To be applicable as a semiconductor device, the electrical properties must be well known. The electrical properties of $B_{12}As_2$ have only seldom been reported, and the materials were typically of poor structural quality [1-5].

Many factors can have an effect on the electrical properties of all materials, especially the impurity concentration and defect density. Thus, measuring the electrical properties is vitally important. Two fundamental methods for measuring the electrical properties of a semiconductor are the Hall effect, and current injection with a radioactive isotope. Electronic device performance is determined by the μτ product (mobility and charge carrier lifetime); a property heavily affected by the concentration of impurities. The importance of the Hall effect is supported by the need to accurately determine the charge carrier concentration, electrical resistivity, and the mobility of majority carriers in semiconductors [6,7].

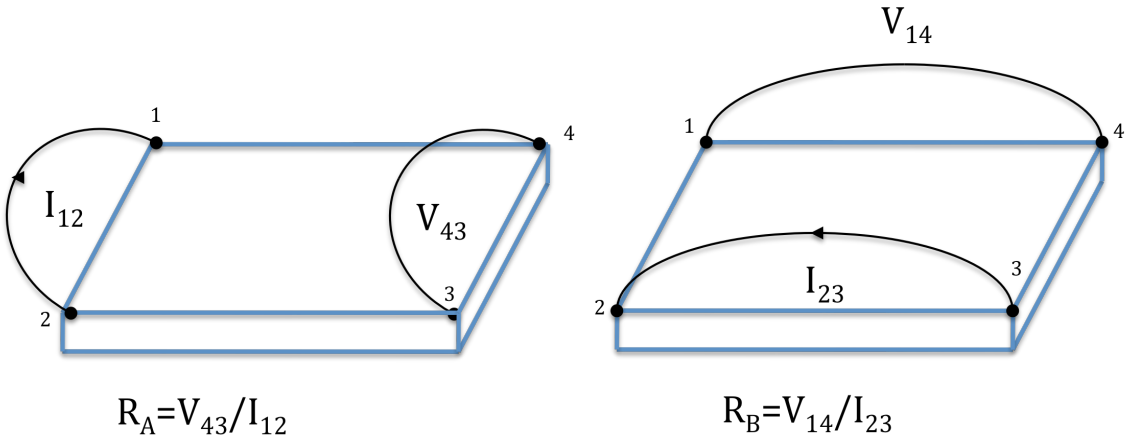

Figure 7-1 - van der Pauw four point probe setup depicting the measurements of R_A, and R_B.

The first step toward calculating the Hall mobility is measuring the Hall voltage V_H and then from the known values of the current (I), magnetic field (B), and q ($1.602x10^{-19}$ C), the sheet density n_s of charge carriers in semiconductors can be measured. Finally, by combining the

sheet density with the sheet resistivity in equations (1) and (2) results in the mobility. The sheet resistance R_S of the semiconductor can be conveniently determined by using the van der Pauw resistivity measurement technique [6-10]. Van der Pauw demonstrated [8,9] that there are actually two characteristic resistances R_A and R_B (Figure 7-1), which are related to the sheet resistance R_S through equation (1).

$$e^{\left(\frac{-\pi R_A}{R_S}\right)} + e^{\left(\frac{-\pi R_B}{R_S}\right)} = 1 \qquad (1)$$

Since sheet resistance involves both sheet density and mobility, the mobility can be calculated from equation (2).

$$\mu = \frac{|V_H|}{R_S I B} = \frac{1}{(q n_S R_S)} \qquad (2)$$

As originally devised by van der Pauw, the general setup consists of an arbitrarily shaped thin-plate sample containing four small ohmic contacts placed on the periphery of the plate [6-10].

There are practical aspects that must be considered when carrying out Hall and resistivity measurements, including the (1) ohmic contact quality and size, (2) sample uniformity and accurate thickness determination, (3) thermomagnetic effects due to nonuniform temperature, and (4) photoconductive and photovoltaic effects which can be minimized by measuring in a dark environment [6-10]. Also, the sample lateral dimensions must be large compared to the size of the contacts and the sample thickness. Finally, one must accurately measure the sample temperature, magnetic field intensity, electrical current, and voltage.

The Hall effect and subsequent mobility are calculated values based on the electrical properties of a semiconductor. Another method for determining the electrical properties of a semiconductor is by measuring the product of the mobility and charge carrier lifetime (the $\mu\tau$ product). The $\mu\tau$ product is significant because it is a direct indicator of whether the semiconductor will perform as an electronic device or not; namely, if the $\mu\tau$ product is large ($>1.0 \times 10^{-5}$ cm^2/V), then the material is suitable for electronic devices [11]. For example, if a material has a low mobility (<10 cm^2/Vs), but has a large charge carrier lifetime (1000 ns), then the material still has a large $\mu\tau$ product and is still suitable for device fabrication. In the example, if only the mobility was measured, then the material might have been deemed unsuitable for electronic devices.

A schematic diagram of the electronic system used to measure the μτ product is shown in Figure 7-2. The sample and the alpha source (Am-241) were placed in a vacuum chamber in order to reduce the possibility of free air ionization. The oscilloscope was used to measure the average pulse height with and without a source present, and the computer software Maestro was connected to the system in order to record the energy spectrum.

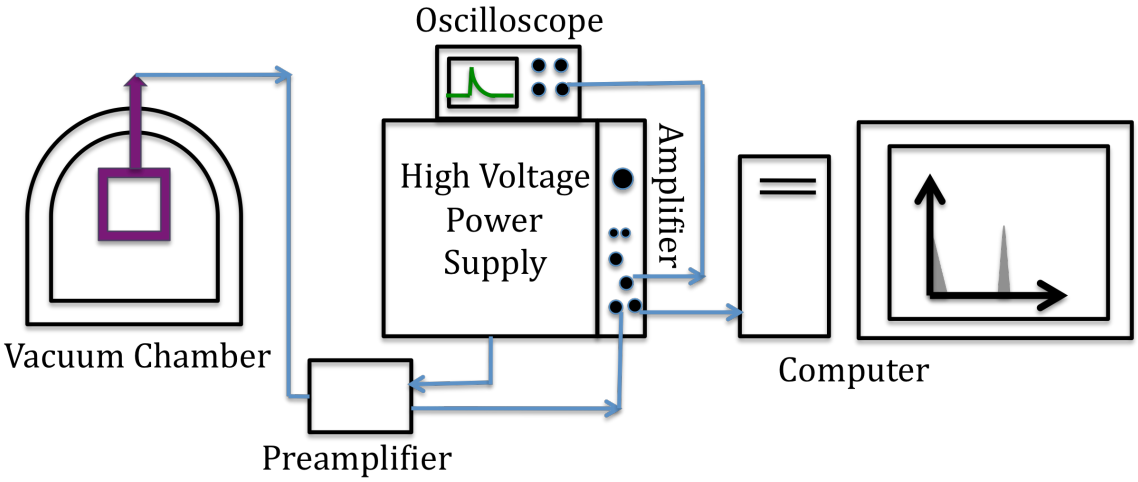

Figure 7-2 - Schematic diagram of the NIM-BIN electronic system for testing radiation detectors.

By injecting current into a biased semiconductor, with a radioisotope, and varying the voltage, it is possible to determine the μτ product using the following equations (3), (4), (5), and (6) [11]:

$$E = \frac{V}{W} \tag{3}$$

$$v_x = \mu E = \mu \frac{V}{W} \tag{4}$$

$$\rho = \frac{v\tau}{W} = \frac{\mu V \tau}{W^2} \tag{5}$$

$$\frac{Q}{Q_o} = pulseheight = \rho\left(1 - e^{-1/\rho}\right) \tag{6}$$

Where E is the electric field, V is the voltage, W is the sample width, ν is the velocity of the charge carriers, μ is the mobility, τ is the charge carrier lifetime, and ρ is a dimensionless variable. By varying the voltage and measuring the pulse height on the oscilloscope, it is possible to back calculate the μτ product from equations (5) and (6).

Previous reports on the electrical properties of boron arsenide included thin films grown by chemical vapor deposition (CVD), and contained high densities of defects [1,2]. In contrast the flux growth method that was used in this study produces crystals of much higher crystal quality, but the disadvantages of the flux method are substitutional or interstitial incorporation of solvent ions into the crystal, microscopic or macroscopic inclusion of solvent or impurities, and non-uniform doping [12]. Incorporation of impurities into the crystal lattice greatly degrades the electrical properties of a semiconductor. Thus, a good understanding of the concentration of impurities is essential to improving the flux growth procedure and the electrical properties.

To identify the type and concentration of impurities, secondary ion mass spectroscopy (SIMS) and x-ray photoelectron spectroscopy (XPS) were employed. Dynamic SIMS uses high sputtering rates to destruct the surface. The collision cascade results in the ejection and ionization of atoms and molecules from the surface layers of the sample. These secondary ions are accelerated into a double focusing mass spectrometer where they are separated according to their energy and mass/charge ratio before being detected [13-16].

The purpose XPS is to determine the chemical composition and bonding on the surface of a material. In XPS, x-rays strike the surface of a sample in an ultrahigh vacuum environment. The emission process was described by Berglund and Spicer [17] as a three-step model. First an x-ray or UV photon is absorbed and an electron is promoted from the ground state to the final state above the Fermi level. The final state lies within the potential field of the solid and satisfies the Schrodinger equation for that field. Second an electron is transported, and third, the electron escapes the vacuum. Since the electron is generated within the potential field of the solid, the wave function contains contributions from the solid even after it has escaped into the vacuum [17].

Previous reports show that thin films of $B_{12}P_2$ and $B_{12}As_2$ have mobilities on the order of 50-100 $cm^2/V \cdot s$ [1,2], in contrast to the low mobilities of boron carbide and β-boron (~1cm^2/V s) [18]. However, there are no reports of the $\mu\tau$ product of any icosahedral boride semiconductors. By comparing the mobility and the $\mu\tau$ product with the impurity concentrations, the prospects of successfully making a boron arsenide electronic device can be determined.

Experimental Procedures

$B_{12}As_2$ crystals were grown by precipitation from molten nickel solutions saturated with elemental boron and arsenic in a sealed quartz ampoule at 1150°C [19]. The $B_{12}As_2$ single crystals selected for the study were typically about 5 x 4 x 1 mm^3 in size and had well-developed facets with mirror-like surfaces. Raman spectroscopy, defect selective etching, and synchrotron white beam x-ray topography were used to analyze the structural quality of the crystals.

To measure the electrical properties two types of devices were fabricated. First, for the Hall effect measurement, four indium contacts (0.5mm in diameter) were soldered onto the periphery of the crystal. Second for the IV curve and the μτ product measurement, Schottky and Ohmic contacts were applied to opposite sides of the crystal. The crystals were planarized, polished, and cleaned with a standard buffered ion etch (BIE). Next the crystals were placed into an electron beam, and an Ohmic contact was evaporated on one side and a Schottky contact was evaporated on the exact opposite. The metal contacts were 500Å of Cr and 1000Å of Pt for the Ohmic, 200Å of Ti and 5000Å of Au for the Schottky, and 0.5-1 mm in diameter. The crystals were then annealed at 900 °C for 1 minute in accordance with the literature [20].

The room-temperature Hall effect measurement was conducted with an Accent HL5500 automated system with a magnetic field of 5 kG. I-V measurement of boron arsenide crystal samples were done using a Keithley 4200 SCS by considering the samples as two wire resistors. The two terminals of the samples (top and bottom contact) were connected to the probe of a signatone probe station, which was connected to the SMU1 (source measuring unit) and SMU2 of Keithley4200 by coaxial cables. The Voltage was swept from 40V to -40V and an I-V profile was obtained.

The μτ product was measured with standard NIM equipment, and Figure 7-3 depicts the boron arsenide devices and the project box used for measuring the μτ product. The device was placed in the vacuum chamber, attached to the electrical system and a reverse bias (-4V) was applied. The background pulse height and energy spectrum were then collected. Next the alpha source (Am-241) was placed in the vacuum chamber inline with the Schottky contact of the device. The bias was again applied and the pulse height and energy spectrum were collected. In both cases, with and without the source, the voltage was varied in approximately 4V increments up to -20V, and pulse height and energy spectrum were recorded. This process was repeated for all four samples, and the results were compared to the Hall effect, SIMS, and XPS analysis.

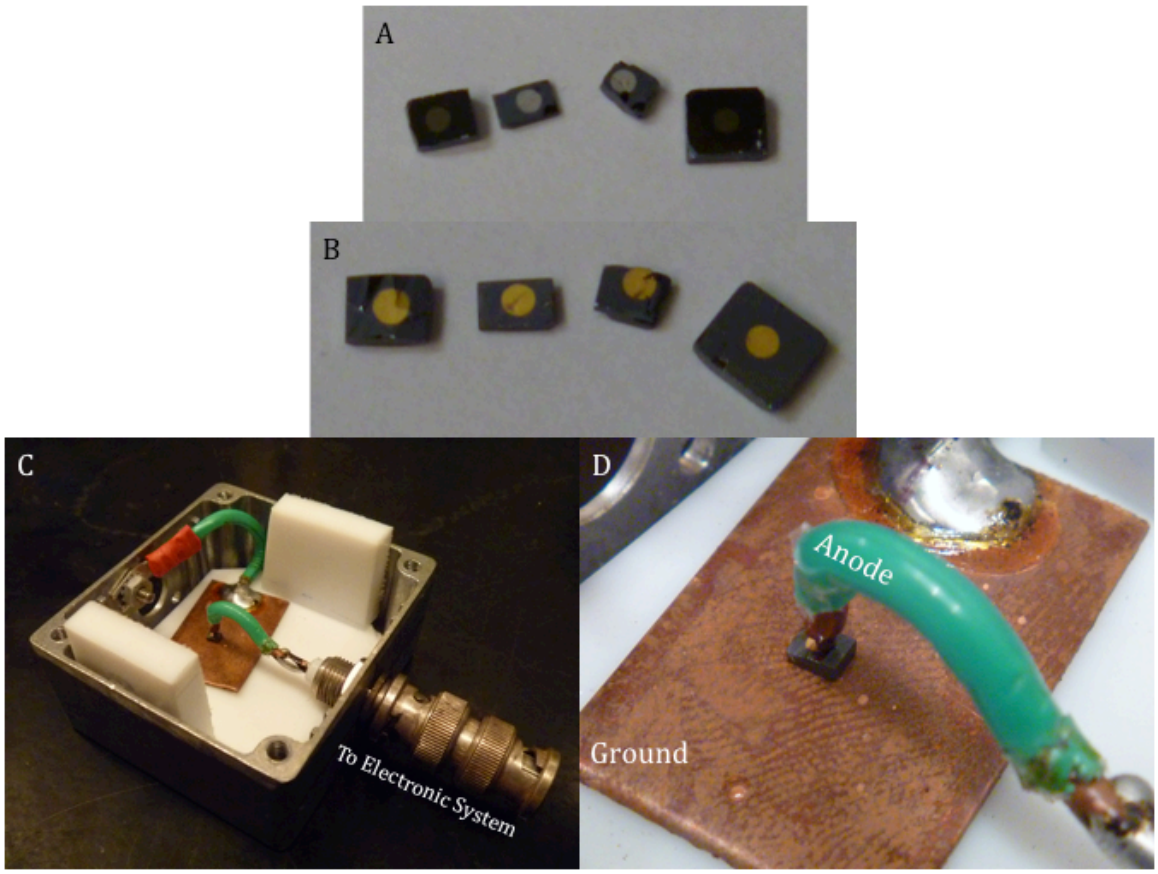

Figure 7-3 - Images of the boron arsenide crystals with (A) Ohmic and (B) Schottky metal contacts. (C) Image of the project box used to hold the electronic device in place, and (D) close-up of the electrical connections between the metal contacts and the Anode and ground.

Results and Discussion

The structural quality of the $B_{12}As_2$ crystals was high as indicated by several methods: Raman spectroscopy, DSE, and SWBXT. Raman spectroscopy detailed excellent quality with the Raman linewidths being narrower for the $B_{12}As_2$ bulk crystals, and in particular the Raman intensity was stronger, as compared to thin films [19]. This illustrates that phonon properties and therefore also more macroscopic properties of the crystals are improved compared to epitaxial films. Only one type of equilateral triangular etch pit with a dimension of ~5-25μm and a density on the order of $5x10^7$ cm^{-2} was produced by defect selective etching, which suggests the crystals are single crystalline and agree with the result from Raman. The SWBXT Laue pattern of the bulk $B_{12}As_2$ crystals lacked any evidence for the existence of twins. The dislocations were

formed by deformation process during precipitation from the solution, and showed the predominant defect in these crystals were edge character growth dislocations with < 001> Burgers vector, and <-110> line direction.

As stated previously, the electronic properties of a semiconductor can be significantly degraded by the concentration of impurities such as H, C, O, and Si. In silicon semiconductors for example, there are approximately $5x10^{22}$ atoms/cm³. Typical dopant concentration in silicon semiconductors may range anywhere from 10^{13} cm^{-3} to 10^{18} cm^{-3}. Doping concentrations above about 10^{18} cm^{-3} are considered degenerate at room temperature [21]. The results from the SIMS analysis of the boron arsenide crystals revealed the concentration of some major impurities (H, C, and Si) were high enough to be considered degenerate (10^{20}, 10^{19}, and 10^{17} respectively), as seen in Figure 7-4.

Table 7-1 – Tabulated atomic percent concentrations of the major impurities found using XPS.

At% ➔ Etch time ⬇	As	B	C	O	Ni	Si
0 s	5.8	28.0	38.2	22.1	1.7	4.0
30 s	11.1	70.4	11.0	5.0	0.9	0.9
60 s	11.7	76.3	7.2	3.9	0.5	0.0

Table 7-1 lists the atomic percent composition of a $B_{12}As_2$ crystal found using XPS analysis. After 60 s of etching with argon ions (a depth of ~6nm), the impurity compositions appear to decrease dramatically, and the B:As ration also becomes ~6:1 (6.52:1). The XPS results follow the SIMS data, where the impurity concentrations do decrease as the depth is increased. However, the SIMS data is quite compelling, and reveals the major disadvantage of the flux growth method, namely, the incorporation of impurities into the crystal lattice. The contamination is likely coming from the original source materials (boron, arsenic, nickel), which where purchased with as much as 2 at% oxygen and 0.35 at% carbon.

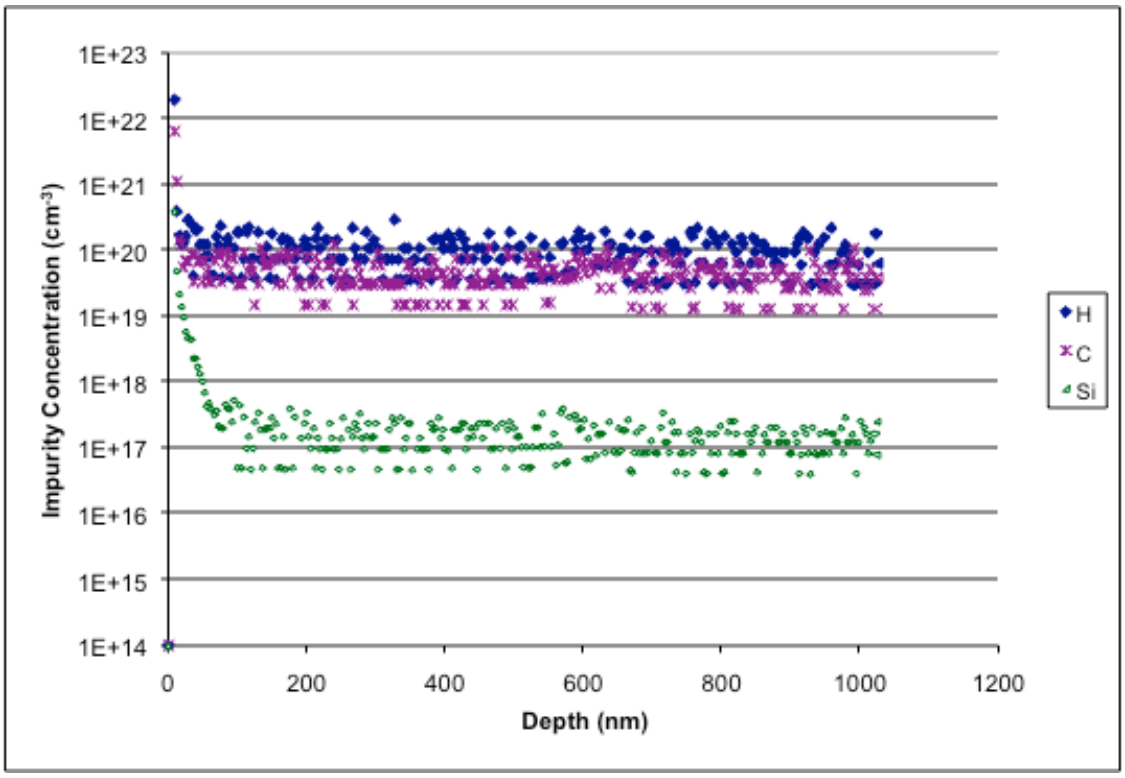

Figure 7-4 - Plot of the impurity concentration vs. the depth of the material. Concentrations above 10^{18} are considered degenerate [20].

Even though the impurity concentrations were found to be quite high, devices were still fabricated and tested. However, before moving forward with evaporating contacts on the boron arsenide crystals, the range of ions in matter (TRIM) was simulated. The simulation included a He (set to 5.5MeV) ion bombardment onto the sample, with a top Ti/Au (200Å/5000Å) layer on a boron arsenide layer (2mm). As seen in Figure 7-5, the ions were able to penetrate 12.9 μm into the sample. The alpha particles deposit most of their energy near the end of their range in the material, as seen in Figure 7-6.

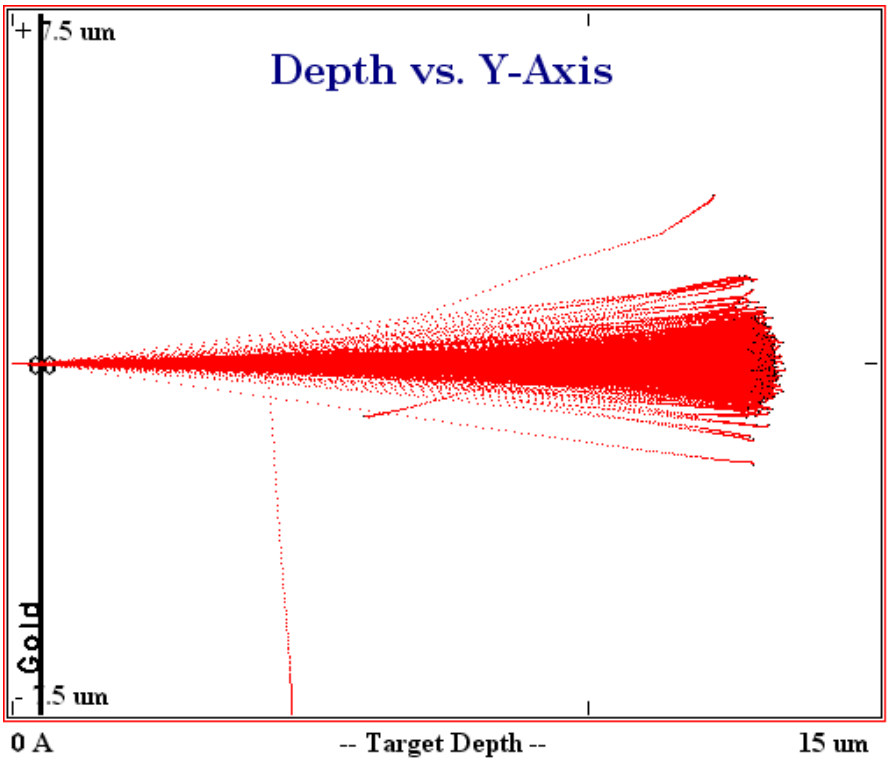

Figure 7-5 - TRIM simulation plot of the penetration distance of 5.5MeV alpha particles into boron arsenide crystals with a Ti/Au metal contact.

With the assurance that the alpha particles would be able to penetrate into the crystal, the metal contacts were placed on the samples. The Cr/Pt metal contact was chosen because Pt is an Ohmic contact on boron arsenide; the Cr was only used as an aid to help the Pt adhere to the crystals [20]. Similarly, the Ti was also used to help the Au adhere to the crystals. A Schottky contact was chosen for the opposite side of the crystals in order to create a blocking contact, which lowered the leakage current from 10^{-10} Amp to 10^{-12} Amp. Au was chosen as the other contact because it forms a Schottky contact to many semiconductors, such as cadmium zinc telluride (CZT). The contacts were annealed at 900°C to improve the connection between the metal and the crystal by lowering the contact resistance [20].

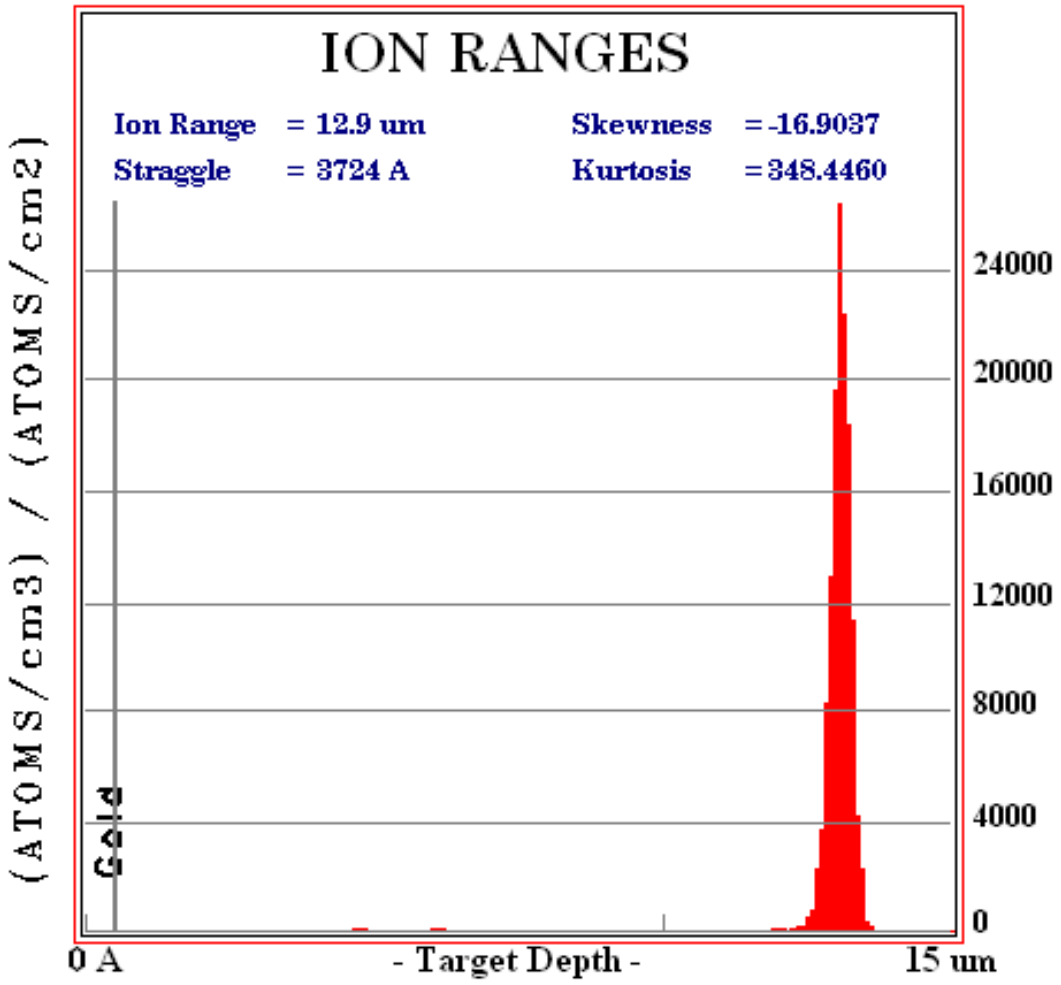

Figure 7-6 - TRIM ionization plot showing the alpha particles depositing their kinetic energy at the end of their range (12.9 µm).

To determine the turn-on and breakdown voltage and the leakage current of the devices, the I-V curves were measured, as seen in Figure 7-7. The devices generally turned-on around +10V, had a breakdown voltage around -20V, and a leakage current of $1x10^{-12}$ Amp. The low leakage current is certainly a result of the Schottky blocking contact, and means that the small changes in current (10^{-9}-10^{-10} Amp) produced from an interaction with a radioactive particle can be measured [12]. The devices all showed rectifying behavior, evident from the plateau on the I-V curve. Rectifying behavior is desired because when operating a radiation detector in this region (+5V ➔-15V, for these $B_{12}As_2$ devices), any small fluctuations in voltage will not produce a significant change in current. Thus, only changes in current produced by an interaction with a radioactive particle will be measured.

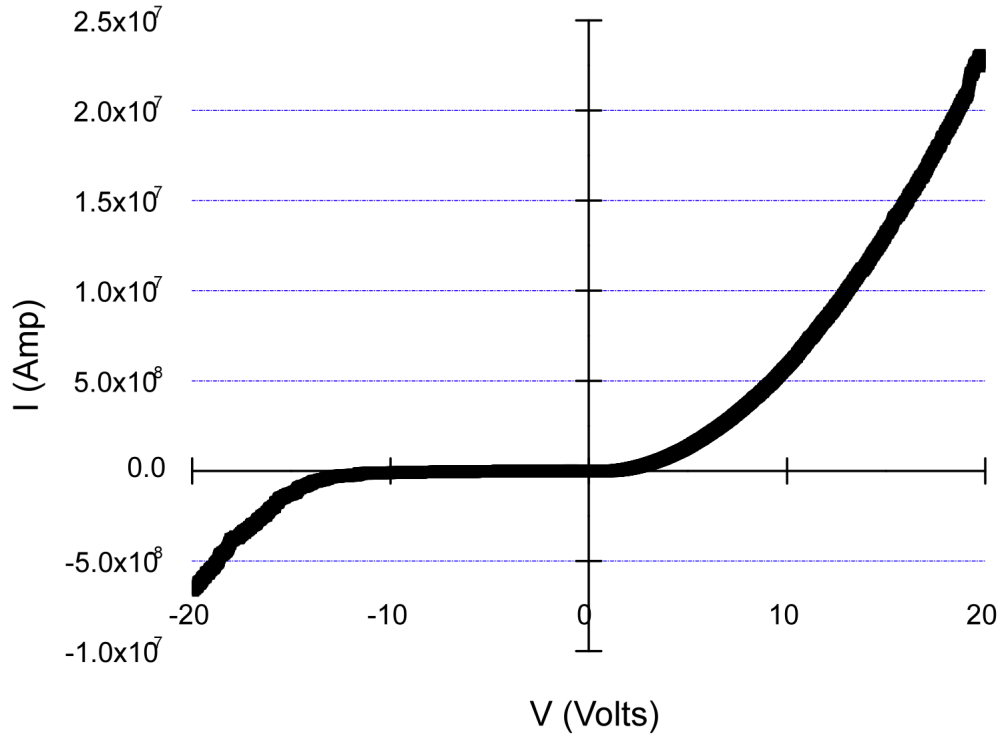

Figure 7-7 - I-V curve measured on a boron arsenide crystals with Ohmic and Schottky metal contacts. Notice the rectifying region between +5V and -15V.

Room temperature Hall effect measurements showed that the crystals were p-type, with a hole concentration of ~10^{17} cm^{-3}, and a hole mobility around 20 cm^2/Vs. The data are consistent with previous reports of boron arsenide thin films (Table 7-2), and show that both CVD and solution growth methods produce crystals of sufficient quality, and good electrical properties. As stated previous, for a semiconductor to work as an electronic device the mobility must be larger than 1 cm^2/Vs. However, the $\mu\tau$ product for thin films has not been reported, and thus no knowledge of the charge carrier lifetime for thin films is available for comparison.

The energy spectra with and without the Am-241 source was identical, indicating that the device did not appear to respond to the alpha particle bombardment, as seen in Figure 7-8. From the TRIM simulation data, the low leakage current, and the Hall effect data it is clear that the alpha particles were indeed entering the crystals, and the leakage current was low enough that the current produced by the alpha particle interactions could have been measured, and the mobility of the charge carriers should have been large enough to collect the current produced. However,

the devices were tested multiple times at the voltage increments listed above, with constantly negative results.

Table 7-2 - List of the data obtained from the Hall effect measurement conducted on a bulk boron arsenide crystal. For comparison the same data are included for a thin film of boron arsenide.

	R **Ωcm**	**R_S** **Ω/cm^2**	**N** **1/cm^3**	**N_S** **1/cm^3**	**μ** **cm^2/Vs**
Bulk $B_{12}As_2$	3.49	49.91	7.28×10^{16}	5.1×10^{15}	24.5
$B_{12}As_2$ Thin Film	5.69×10^{3}	4.22×10^{7}	1.45×10^{13}	7.25×10^{9}	27.9

Although the devices appeared to be excellent candidates for radiation detectors, the charge carrier lifetime must be too low (>1 ns) to allow for the produced current time to travel the width of the crystals. These results emphasize the importance of characterization with both the Hall effect and the μτ product. Indeed, without the μτ product measurement, the incorrect conclusion would have been drawn that these boron arsenide crystals would be excellent electronic devices, when in fact the devices had no response to alpha particle interaction.

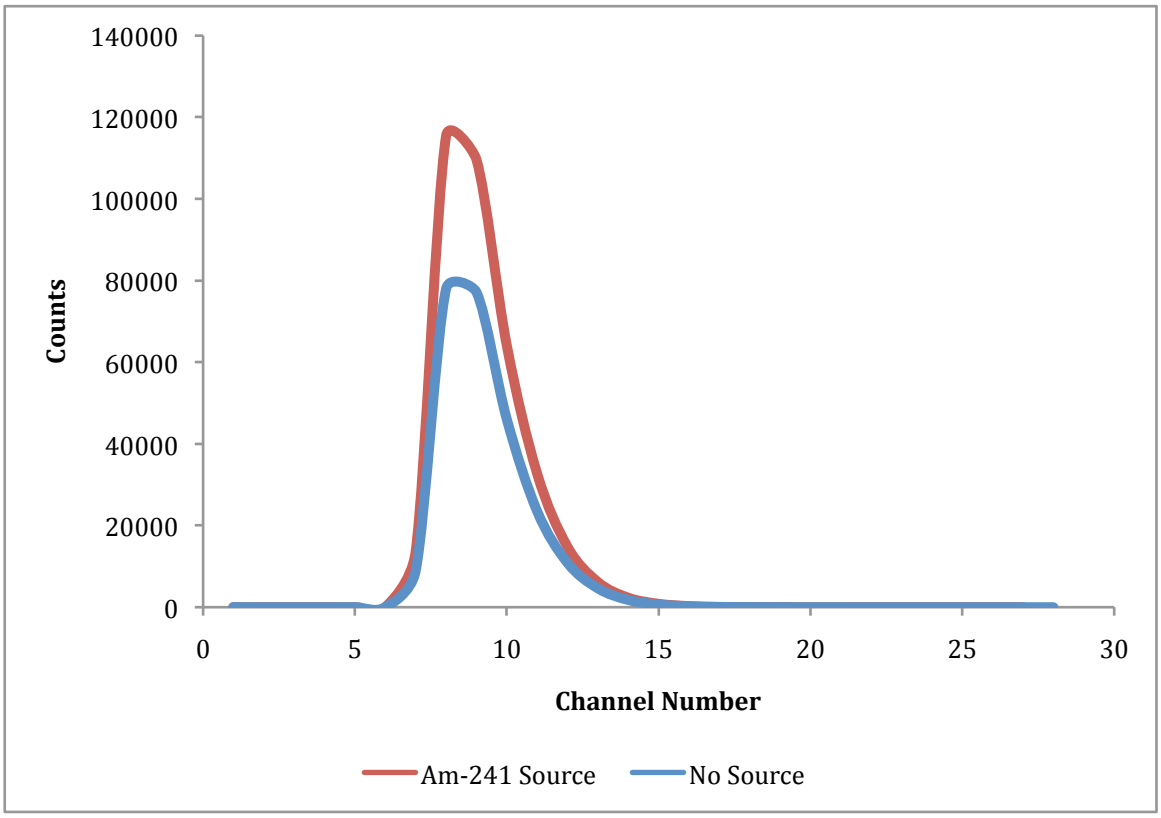

Figure 7-8 - Energy spectrum for the μτ product measurement. The measurement with the alpha particle source was taken for a longer time, and thus collected more counts, but the Channel Number (9) indicates background energy. The most significant observation being that there is no full energy peak for the 5.5MeV alpha particle, which should appear as an individual peak in the 300-500 Channel Number range.

The low charge carrier lifetime, and generally poor electrical properties, were attributed to the exceedingly high impurity concentrations present in the crystals revealed by SIMS and XPS analysis. These impurities are most certainly producing trapping, or recombination, centers in the otherwise wide bandgap (3.2eV) of boron arsenide. Thus lowering the lifetime and probably the mobility of the charge carriers. These results were disappointing, but not necessarily surprising given that the crystal color was constantly black and opaque; with the rare exception of some yellow colored transparent crystals. The color of a material with a bandgap above 3eV should be colorless and transparent [22], visually revealing high impurity concentrations, and the potential for poor electrical properties.

Conclusions

High structurally quality boron arsenide crystals were produced using the solution growth method, but SIMS analysis revealed degenerately high impurity concentrations. The rectifying behavior, low leakage current ($1x10^{-12}$ Amp), and hole mobility (24.5 cm^2/Vs) of boron arsenide are still factors leading to a potential for good electronic devices. However, the impurity concentrations remain a significant hindrance to the advancement of the technology. With improved crystal growth techniques, such as higher purity source materials, the quality of the boron arsenide crystals could most certainly be improved to the point were a better evaluation of its potential for electronic devices could be made.

References

[1] S. Bakalova, Y. Gong, C. Cobet, N. Esser, Y. Zhang, J. H. Edgar, Y. Zhang, M. Dudley, and M. Kuball, Phys. Rev. B, **81**, 075114 (2010).

[2] H. Chen, Defect Structures and Growth Mechanisms of $B_{12}As_2$ Epilayers Grown on 6H-SiC and 15R-Sic Substrates, Dissertation. Stony Brook University (2008)

[3] D. Emin, J. Solid State Chem. **179** 2791 (2006).

[4] M. Carrard, D. Emin, L. Zuppiroli, Phys. Rev. B **51** 11, 270 (1995).

[5] J.R. Michael, T.L. Aselage, D. Emin, P.G. Kotula, J. Mater. Res. **20** 3004 (2005).

[6] The van der Pauw technique and Hall effect measurement. Information found online at: http://www.nist.gov/pml/semiconductor/hall_intro.cfm (December 21, 2010).

[7] Standard Test Methods for Measuring Resistivity and Hall Coefficient and Determining Hall Mobility in Single-Crystal Semiconductors, ASTM Designation F76, Annual Book of ASTM Standards, Vol. 10.05 (2000).

[8] L. J. van der Pauw, Philips Res. Repts. **13**, 1-9 (1958).

[9] L. J. van der Pauw, Philips Tech. Rev. **20**, 220-224 (1958).

[10] C. Kasl, and M.J.R. Hoch, Rev. of Sci. Instru. **76** 0339071-0339074 (2005)

[11] M. Lampert, P. Mark, Current Injection in Solids, Academic Press, New York, New York (1970)

[12] D. Elwell, H.J. Scheel, Crystal Growth from High-Temperature Solutions. London, Academic Press, (1975).

[13] C. F. Robinson, Ion microprobe instrumentation, in Microprobe Analysis, C. A. Andersen, Ed. New York: Wiley, 507–529 (1973).

[14] A. Benninghoven, Surf. Sci., **299/300** 246–260, (1994).

[15] J. C. Vickerman, H. Brown, and N. M. Reed, Secondary Ion Mass Spectrometry Principles and Applications. Oxford, U.K.: Clarendon, (1989).

[16] A. C. Diebold, M. R. Kump, J. J. Kopanski, and D. G. Seiler, J. Vac. Sci. Technol. B, **14**, 196–201, 1996.

[17] J. Riviére, Handbook of Surface and Interface Analysis Methods for Problem-Solving, 2nd Ed. Taylor and Francis, Boca Raton FL (2009)

[18] D. Emin, Physics Today, January, **55** (1987)

[19] C.E. Whiteley, A. Mayo, J.H. Edgar, M. Kuball, and Y. Zhang J. Cryst. Growth **318** 553-557 (2011).

[20] S. H. Wang, E. M. Lysczek, Bangzhi Liu, and S. E. Mohney, Z. Xu, R. Nagarajan, and J. H. Edgar, App. Phy. Let. **87** 042103 (2005).

[21] A.B Sproul, M.A Green, J. Appl. Phys. **70** 846 (1991).

[22] K. Nassau, American Mineralogist, **63** 219-229 (1978)

CHAPTER 8 - CONCLUSIONS AND FUTURE WORK

Icosahedral boron arsenide, $B_{12}As_2$, has unique chemical, physical, and electrical properties, and when combined with its radiation hardness, and wide band gap (3.2 eV), it becomes a very interesting material for neutron detectors and radioisotope batteries. To evaluate the potential applications for boron arsenide crystals, the fundamental properties, such as growth conditions, structural characterization, chemical compositions, detector fabrication, and device testing were examined.

The coefficient of thermal expansion of icosahedral boron arsenide ($B_{12}As_2$) powder was calculated from HTXRD data up to 850 °C. A comparison with the reported literature on solids with similar structure (boron carbide) and substrates for epitaxial thin films of $B_{12}As_2$, was completed. HTXRD revealed a large volumetric coefficient of thermal expansion ($1.92x10^{-5}$ K^{-1}), and a 9% anisotropy between the *a* and *c* direction. The expansion data exposes the importance of a slow cooling rate during the flux growth method, and the large difference between $B_{12}As_2$ and Si or SiC (common substrates for thin films) explains the strain and cracking of the $B_{12}As_2$ thin films that is experimentally observed [1,17].

A detailed exploration of the growth parameters of boron arsenide revealed that large (8mm) $B_{12}As_2$ crystals could be grown via a flux growth mechanism with nickel as the solvent. Using elemental boron (instead of $B_{12}As_2$ powder) as the source material is a superior method for producing large crystals; 8mm compared to 1mm. The crystals formed in the flux and, due to a low solubility of the crystals in the solution, precipitated out of the solution when the temperature was slowly decreased (3.5°C/hr). Structural characterization of the $B_{12}As_2$ crystals with defect selective etching, Raman spectroscopy, and synchrotron white beam x-ray topography demonstrated that high quality (low defect density) semiconductors can be produced at a relatively low temperature (1050-1150 °C), much lower than the melting points of the source materials (>2000 °C for boron).

Defect selective etching of $B_{12}As_2$ crystals under reaction limited kinetics was conducted, producing a low density of pits ($5x10^7$ cm^{-2}) after etching at 550°C for 2 minutes in molten KOH. Additionally, etching multi-faceted crystals revealed that the facets have orientation specific defects, which require further investigation. By studying the etching behavior of unique crystal facets, a correlation was drawn that relates the etch pit shapes to particular defects (edge

dislocations) and crystal orientation (the (111) facet orientation produced only triangle etch-pits). Thus, defect-selective etching is an effective method for determining the extent dislocations extending to the surface of $B_{12}As_2$ crystals, and therefore an excellent way to judge the quality of the crystals.

The microstructure of $B_{12}As_2$ bulk crystals produced using the flux growth method was examined. The SWBXT study suggests that the major face of the plate-like crystals was (111) type, while (100), (010) and (001) type facets were also observed optically. SWBXT revealed untwinned (111) orientated $B_{12}As_2$, with significantly improved macroscopic properties. The most prominent defects were typically edge-dislocations. In whole, characterization with these three techniques shows that flux growth is a viable method for producing good structural quality $B_{12}As_2$ crystals.

The chemical composition of the boron arsenide crystals was examined, and the results from the SIMS analysis revealed the concentration of some major impurities (H, C, and Si) were high enough to be considered degenerate (10^{20}, 10^{19}, and 10^{17} respectively). These contaminates were likely introduced into the system from the source materials (B, As, Ni), and the quartz tube.

Next the electrical properties were measured using three techniques: I-V curves, Hall effect measurements, and by determining the $\mu\tau$ product. The I-V curves showed rectifying behavior and a leakage current of $1x10^{-12}$ Amp. The mobility ($24.5cm^2/Vs$) was calculated from the Hall effect data, and an attempt to measure the $\mu\tau$ product was done by injecting current into the crystals with an Am-241 alpha source. From the radiation testing, it appeared that the crystals did not respond to the injection of current, even though the mobility and leakage current were favorable. The conclusion was that the crystals must have a very low charge carrier lifetime (<<100ns). A low charge carrier lifetime, and generally mediocre electrical properties, were attributed to the exceedingly high impurity concentrations present in the crystals revealed by SIMS analysis. These impurities are most certainly producing trapping, or recombination, centers in the otherwise wide bandgap (3.2eV) of boron arsenide.

Dramatically lowering the impurity concentrations by starting with higher purity source materials or by using the flux grown crystals as substrates for the epitaxial growth of $B_{12}As_2$ is undoubtedly the next step. Producing higher quality boron arsenide crystals might improve the electrical properties to the point where a better evaluation of its potential for electronic devices could be made.

Additionally, although 8mm crystals are a significant improvement over previous reports [14-18], growing even larger crystals (>2 cm^2) will allow for easier device fabrication and straightforward implementation as substrates for epitaxial experiments. One approach to growing larger $B_{12}As_2$ crystals is to identify the temperature, or range of temperatures, where the growth rate is the highest, and slow cool and hold the flux at that temperature. This procedure offers two advantages over the procedure mentioned in this study, namely, the experiments can be much shorter (as much as a few days), and the crystals are allowed to grow in their preferred temperature regime (less strain, larger, and well developed facets) [40].

REFERENCES

[1] S. Ovsyannikov, A. Polian, P. Munsch, J. Chervin, G. Marchand, and T. L. Aselage, Physical Review B **81**, 140103 (2010)

[2] K. Shirai, A. Masago, and H. Katayama-Yoshida, Phys. Status Solidi B **244**, 303 (2007)

[3] M. Kaneshige, S. Hirayam, T. Yabuushi, T. Matsuoka, K. Shimizu, Y. Mita, H. Hyodo, K. Kimura, J. Phys. Soc. Jpn. **76**, Suppl. A, 19 (2007)

[4] B. Siberchicot, Phys. Rev. B **79**, 224101 (2009)

[5] M. I. Eremets, V.V. Struzhkin, H.K. Mao, R.J. Hemley, Science **293**, 272 (2001)

[6] S. K. Bose, T. Kato, and O. Jepsen, Phys. Rev. B **72**, 184509 (2005)

[7] E. Yu. Zarechnaya et al., Sci. Technol. Adv. Mater. **9**, 044209 (2008)

[8] E. Yu. Zarechnaya et al., Phys. Rev. Lett. 102, 185501 (2009)

[9] Y. Gong, Y. Zhang, M. Dudley, Y. Zhang, J. H. Edgar, P. J. Heard, and M. Kuball, J. App. Phys. **108** 084906 (2010)

[10] S. Sasakia, M. Takedaa, K. Yokoyamaa, T. Miuraa, T. Suzukib, H. Suematsub, W. Jiangb, K. Yatsuib, Sci. and Tech. of Adv. Mat. **6** 181–184 (2005)

[11] V. Lankau, H. Martin, R. Hempel-Weber, N. Oeschler, and A. Micaelis, J. of Elect. Mat. **39**, 1809-1813 (2010)

[12] M. Carrard, D. Emin, and L. Zuppiroli, Phys. Rev. B **51**, 11270 (1995)

[13] D. Emin, J. Solid State Chem. **179** 2791 (2006)

[14] W. Orellana and H. Chacham, Phys. Rev. B **63** 125205 (2001).

[15] Y. Kumashiro, J. Mater. Res. **5** 2933 (1990).

[16] T.L. Chu and A.E. Hyslop, J. Electrochem. Soc. **121** 412 (1974).

[17] F. Thévenot, J. Europ. Ceram. Soc. **6** 205 (1990)

[18] G.A. Slack, T.F. McNelly, and E.A. Taft, J. Phys. Chem. Solids **44**, 1009 (1983).

[19] F.H. Horn, J. Electrochem. Soc. **106** 905 (1959).

[20] R.A. Burmeister, Jr. and P.E. Greene, Trans. Metal. Soc. AIME **239** 408 (1967).

[21] Y. Kumashiro, T. Yao, and S. Gonda, J. Cryst. Growth **70** 515 (1984).

[22] T.L. Aselage, Mater. Res. Soc. Symp. Proc. **97** 101 (1987).

[23] T.L. Aselage, S.B. Van Deusen, and B. Morosin, J. Less-Common Met. **166** 29 (1990).

[24] P. Yang and T.L. Aselage, Proc. 11th Int. Symp. Boron, Borides and related compounds, JJAP series **10** 130 (1994).

[25] M. Yamamoto, Y. Hamazaki, M. Tsukihara, Y. Naoi, K. Nishino, and S. Sakai, Jpn. J. Appl. Phys. **46** 323 (2007).

[26] O.A. Golikova, Phys. Stat. Sol. A **51** 11 (1979).

[27] T.L. Aselage, D. Emin, G.A. Samara, D.R. Tallant, S.B. Van Deusen, M.O. Eatough, H.L. Tardy, E.L. Venturini, and S.M. Johnson, Phys. Rev. B **48** 11759 (1993).

[28] Z. Xu, J.H. Edgar, D.C. Look, S. Baumann, R.J. Bleiler, S.H. Wang, and S.E. Mohney, J. Appl. Phys. **101** 053710 (2007).

[29] H. Werheit and U. Kuhlmann, J. Solid State Chem. **133** 140 (1997).

[30] F. Wald and J. Bulitt, Semiconductor neutron detectors, U. S. Nat. Tech. Inform. Serv., AD Rep. (1973), (No. 771526/1GA), 36.

[31] Insaco Inc, Information on the properties of Boron Carbide can be found at, http://www.insaco.com/MatPages/mat_display.asp?M=BC (January 11, 2011)

[32] Z. Xu, Dissertation. Kansas State University (2005)

[33] Harris, Gary L. (1995). Properties of Silicon Carbide. Institution of Engineering and Technology. Online version available at: http://www.knovel.com/web/portal/browse/display?_EXT_KNOVEL_DISPLAY_bookid=1147&VerticalID=0 (January 11, 2011)

[34] Hull, Robert (1999). Properties of Crystalline Silicon. Institution of Engineering and Technology. Online version available at: http://www.knovel.com/web/portal/browse/display?_EXT_KNOVEL_DISPLAY_bookid=1148&VerticalID=0 (January 11, 2011)

[35] H. Chen, Defect Structures and Growth Mechanisms of $B_{12}As_2$ Epilayers Grown on 6H-SiC and 15R-Sic Substrates. Dissertation. Stony Brook University (2008)

[36] M. Dresselhaus, G. Chen, M. Y. Tang, R. Yang, H. Lee, D. Yang, Z. Ren, J. Fleurial, and P.

[37] J. R. Michael, T. L. Aselage, D. Emin and P.G. Kotula, J. Mater. Res., **20** (11), 3004 (2005)

[38] W.M. Vetter, R. Nagarajan, J. H. Edgar and M. Dudley, Mater. Lett., **58**, 1331 (2004)

[39] S. H. Wang, E. M. Lysczek, Bangzhi Liu, and S. E. Mohney, Z. Xu, R. Nagarajan, and J. H. Edgar, App. Phy. Let. **87** 042103 (2005).

[40] D Elwell, H.J. Scheel, Crystal Growth from High-Temperature Solutions, Academic Press, (1975)

[41] M. Wald, Shortage Slows a Program to Detect Nuclear Bombs, November 2009, http://www.nytimes.com/2009/11/23/us/23helium.html

[42] N. Tsolfanidis, Measurement and Detection of Radiation, 2nd Ed.; Taylor & Francis: Bristol, (1995)

[43] D.S. McGregor, S.M. Vernon, H.K. Gersch, IEEE Trans on Nuc. Scie. **47** 1364-1370 (2000).

[44] D.S. McGregor, T.C. Unruh, W.J. McNeil, Nuc. Inst. and Meth. Phys. Res. **591** 530-533 (2008)

[45] D.S. McGregor and J.K. Shultis, Nucl. Instr. Meth. Phys. Res. A **517** 180 (2004).

[46] L. Vel, G. Demazeau, and J. Etourneau, Mater. Sci. Eng. B **10** 149 (1991).

[47] Y. Kubota, K.Watanabe, and T. Taniguchi, Jpn. J. Appl. Phys. **46** 311 (2007).

[48] J.D. Buckley and J.A. Cooley, Mater. Sci. Research **5** 547 (1971).

[49] Z.W. Bell, D.A. Carpenter, S.S. Cristy, V.E. Lamberti, A. Burger, B.F. Woodfield, T. Niedermayr, I.D. Hau, S.E. Labov, S. Friedrich, W.G. West, K.R. Pohl, and L. van den Berg, Phys. Stat. Sol. C **2** 1592 (2005).

[50] D. Emin, J. Solid State Chem. **179** 2791 (2006).

[51] Bower, K.E. Barbanel, Y.A. Shreter, Y.G. Bohnert, G.W. Polymers, Posphors, and Voltaics for Radioisotope Microbatteries, CRC Press: New York, (2002)

[52] Cress, C. (2008) Effects of Ionizing Radiation on Nano-materials and III-V Semiconductors. PhD Dissertation. Rochester Institute of Technology, United States.

[53] P. Rappaport, J.J. Loferski, and E.G. Linder, RCA Rev **17** 100 (1956)

[54] E.M. Baum, H.D. Knox, T.R. Miller, Nuclides and Isotopes; Chart of the Nuclides, 16th Ed.; Lackheed Martin, (2002).

[55] T. Shaffner, Proc. IEEE, Vol. **8**, NO. 9, (2000)

[56] W. R. Runyan and T. J. Shaffner, Semiconductor Measurements and Instrumentation. New York: McGraw-Hill, (1998).

[57] D. A. Wollman, K. D. Irwin, G. C. Hilton, L. L. Dulcie, D. E. Newbury, and J. M. Martinis, J. Microscopy, **188**,196–223, (1997).

[58] M. LeGros, E. Silver, D. Schneider, J. McDonald, S. Bardin, R. Schuch, N. Madden, and J. Beeman, Nucl. Instrum. Meth. A, **357**, 110–114, (1996).

[59] J. Riviére, Handbook of Surface and Interface Analysis Methods for Problem-Solving, 2nd Ed. Taylor and Francis, Boca Raton FL (2009)

[60] C. F. Robinson, "Ion microprobe instrumentation," in Microprobe Analysis, C. A. Andersen, Ed. New York: Wiley, 507–529 (1973).

[61] A. Benninghoven, Surface analysis by secondary ion mass spec- trometry (SIMS), Surf. Sci., **299/300**, 246–260, (1994).

[62] J. C. Vickerman, H. Brown, and N. M. Reed, Secondary Ion Mass Spectrometry Principles and Applications. Oxford, U.K.: Clarendon, (1989).

[63] A. C. Diebold, M. R. Kump, J. J. Kopanski, and D. G. Seiler, J. Vac. Sci. Technol. B, **14**, 196–201, (1996).

[64] Paul A., Tipler; Gene Mosca (2008). Physics for Scientists and Engineers, 6th Edition, New York, NY: Worth Publishers

[65] Turcotte, Donald L.; Schubert, Gerald (2002). Geodynamics ,2nd Edition, Cambridge

[66] G. V. Tsagareishvili, T.G. Nakashidze, J. Sh. Jobava, G.P. Lomidize, D.I. Khulelidze, D. Tsagareishvili, and O.A. Tsagareishvili, Journal of the Less-Common Metals, **117** 159-161 (1986)

[67] B. Raghothamachar, G. Dhanaraj, J. Bai, and M. Dudley, Micro. Res. Tech. 343-358 (2006)

[68] T. Tuomi, J. Synchrotron Rad. 174-178 (2002)

[69] D.J. Gardiner, Practical Raman spectroscopy. Springer-Verlag. (1989).

[70] The van der Pauw technique and Hall effect measurement. Information found online at: http://www.nist.gov/pml/semiconductor/hall_intro.cfm (December 21, 2010).

[71] "Standard Test Methods for Measuring Resistivity and Hall Coefficient and Determining Hall Mobility in Single-Crystal Semiconductors," ASTM Designation F76, Annual Book of ASTM Standards, Vol. 10.05 (2000).

[72] L. J. van der Pauw, Philips Res. Repts. **13**, 1-9 (1958).

[73] L. J. van der Pauw, Philips Tech. Rev. **20**, 220-224 (1958).

[74] C. Kasl, and M.J.R. Hoch, Rev. of Sci. Instru. **76** 0339071-0339074 (2005)